

Stability and Cyclability Predictions of Redox Active Organic Molecules for Non-Aqueous Redox Flow Batteries

by

Benjamin David Silcox

A dissertation submitted in partial fulfillment
of the requirements for the degree of
Doctor of Philosophy
(Chemical Engineering)
in the University of Michigan
2021

Doctoral Committee:

Professor Nirala Singh, Co-Chair
Professor Levi T. Thompson, Co-Chair
Professor Bryan R. Goldsmith
Professor Melanie S. Sanford
Dr. Lu Zhang, Argonne National Laboratory

Benjamin David Silcox

bsilcox@umich.edu

ORCID iD: [0000-0002-8012-2504](https://orcid.org/0000-0002-8012-2504)

© Benjamin David Silcox 2021

Dedication

To my friends and family.

Acknowledgments

There are many people that contributed to my success in graduate school. I would like to start by thanking the members of the Thompson research group for their guidance and mentorship. Specifically, Dr. Sydney Laramie, Dr. Jonathan Kucharyson, Dr. Siuon Tung, and Zixuan Wang. I would also like to thank all the members of the Singh Lab for welcoming me into their group: Harsh Agarwal, James Akinola, Cailin Buchanan, Danielle Richards, and Zixuan Wang. This thesis could not be completed without the collaboration from Dr. Jingjing Zhang and Dr. Ilya Shkrob from the Zhang research group at Argonne National Laboratory. Additional thanks to Jacques Esterhuizen from the Goldsmith Lab and Dr. Lei Cheng for their assistance with computational methods. Finally, I would like to thank the Joint Center for Energy Storage Research for funding a portion of this research.

Table of Contents

Dedication	ii
Acknowledgments	iii
List of Figures	ix
List of Tables	xiii
List of Schemes	xv
Abstract	xvi
Chapter 1: Introduction	1
1.1 Energy Storage	1
1.2 Redox Flow Batteries	3
1.2.1 Aqueous Redox Flow Batteries	5
1.2.2 Non-Aqueous Redox Flow Batteries	6
1.2.2.1 Non-aqueous Electrolytes	6
1.2.2.2 Active Species	7
1.3 Research Motivation	9
1.3.1 Stability	9
1.3.2 Cyclability	9
1.3.3 Prediction	10
1.4 Research Summary and Goals	10
1.5 Chapter Summaries	11
1.5.2 Chapter 2: A Cycling Comparison of Dialkoxyarene Catholytes	11
1.5.3 Chapter 3: Factors Affecting Bulk Electrolysis Cycling Performance	11

1.5.4 Chapter 4: A Kinetic Model for Redox Organic Active Material Cycling	11
1.5.5 Chapter 5: Stability Predictions for ROMs	12
1.5.6 Chapter 6: Cyclability Predictions for Catholyte ROMs	12
Chapter 2: A Cycling Comparison of Dialkoxyarene Catholytes	13
2.1 Background and Approach	13
2.2 Experimental	14
2.2.1 Molecule Set	14
2.2.2 Cyclic Voltammetry	15
2.2.3 Bulk Electrolysis	17
2.2.4 Density Functional Theory	20
2.2.4.1 Standard Potential Calculation	21
2.3 Results and Discussion	22
2.3.1 Electrochemical Reversibility and Oxidation Potentials	22
2.3.2 Cyclability	27
2.3.3 Decay Mechanisms	29
2.3.4 Cyclability Comparisons with ANL	31
2.4 Conclusions	33
2.5 Acknowledgments	33
Chapter 3: Factors Affecting Bulk Electrolysis Cycling Performance	34
3.1 Background and Approach	34
3.2 Experimental	35
3.2.1 Materials	35
3.2.1.1 Active Materials	35
3.2.1.2 Supporting Salts	36
3.2.2 Electrochemical Methods	37
3.2.2.1 Cyclic Voltammetry	37
3.2.2.2 Bulk Electrolysis	37

3.2.2.3 Active Material Concentration	38
3.2.2.4 Cycle Rate	38
3.2.3 Computational Methods	38
3.2.3.1 Density Functional Theory	38
3.2.3.2 Molecular Dynamics	38
3.3. Results and Discussion	38
3.3.1 Oxidation Potentials and Electrochemical Reversibility	38
3.3.2 Cycling Summary	40
3.3.3 DDB Summary	43
3.3.4 DBBB Summary	44
3.3.5 Similarities in DDB and DBBB Performance	44
3.3.6 TEMPO Summary	44
3.3.7 Exceptional Dialkoxyarene Performance	46
3.3.8 The Impact of Supporting Salt Choice on N80	46
3.3.8.1 Incompatibility with BF_4^-	47
3.3.8.2 Dialkoxyarene Behavior with Li^+	48
3.3.8.3 TEMPO Behavior with Li^+	49
3.3.9 Poor Performance at 20 mM/3 C	51
3.3.10 The Impact of Active Material Concentration on N80	51
3.3.11 The Impact of Cycle Rate on N80	53
3.4 Conclusions	55
3.5 Acknowledgements	55
Chapter 4: A Kinetic Model for Redox Active Organic Molecule Cycling	56
4.1 Background and Approach	56
4.1.1 Model Development	57
4.1.1.1 Model Variation for TEMPO	61
4.2 Experimental	62
4.2.1 TEMPO Stability Measurements	62

4.3 Results and Discussion	63
4.3.1 ϕ	63
4.3.2 Maximum CE	64
4.3.3 Recovery Summary	65
4.3.4 Cells above Maximum CE	71
4.3.5 New Insights from ϕ	72
4.4 Conclusions	73
4.5 Acknowledgements	73
Chapter 5: Stability Predictions for Redox Active Organic Molecules	74
5.1 Background and Approach	74
5.2 Experimental	76
5.2.1 ROMs	76
5.2.2 Density Functional Theory	76
5.2.3 Sure Independence Screening and Sparsifying Operator	81
5.3 Results and Discussion	82
5.3.1 A Binary Classifier for Generalized ROM Stability	82
5.3.1.2 Cross Validation	83
5.3.2 Dialkoxyarene Stability Predictions	88
5.3.2.1 Stability Prediction of Hydrocarbon-Substituted Dialkoxyarenes	89
5.3.2.2 Multi-Task Stability Prediction of Dialkoxyarenes	91
5.4 Conclusions	93
5.5 Acknowledgments	94
Chapter 6: Cyclability Predictions for Catholyte Redox Active Organic Molecules	95
6.1 Background and Approach	95
6.2 Experimental	97
6.2.1 ROMs	97

6.2.2 Density Functional Theory	99
6.2.3 Sure Independence Screening and Sparsifying Operator	99
6.3 Results and Discussion	99
6.3.1 A Simple Model for Dialkoxyarene N80 with a TBAPF ₆ /MeCN Electrolyte	99
6.3.1.1 Cross Validation	101
6.3.1.2 Liquid Dialkoxyarene Validation	101
6.3.1.3 The Simple Model for a LiTFSi/MeCN Electrolyte	101
6.3.2 Cyclability Models for Varied Experimental Conditions and Supporting Salts	103
6.3.2.1 General Models for Catholyte ROM Cyclability	103
6.3.2.2 Models at Individual Experimental Conditions	104
6.3.3 Models for Individual Active Materials and Experimental Conditions	107
6.3.3.1 DBBB	108
6.3.3.2 TEMPO	109
6.4 Conclusions	113
6.5 Acknowledgments	114
Chapter 7: Conclusions and Future Directions	115
7.1 Conclusions	115
7.1.1. Cyclability Characterization	115
7.1.2 Computational Screening and Prediction	116
7.2 Future Directions	117
References	119

List of Figures

Figure 1.1 U.S. overall and renewable power generation projections.	2
Figure 1.2 U.S. 2020 energy storage capacity, rated power includes announced projects.	2
Figure 1.3 Diagram of a redox flow battery.	4
Figure 2.1 Example CV with cathodic and anodic peak potentials ($E_{p,c}$ and $E_{p,a}$) and peak heights ($i_{p,c}$ and $i_{p,a}$) labeled with blue and red dashed lines, respectively. Scans were taken starting at a potential of 0 V to a termination point of 1 V, where they reversed direction.	16
Figure 2.2 Example BE current response with cathodic and anodic peak potentials ($E_{p,c}$ and $E_{p,a}$) labeled with blue dashed lines. $E_{p,c}$ is located at the halfway point of oxidation and $E_{p,a}$ is located at the halfway point of reduction.	18
Figure 2.3 An example capacity vs cycle graph from BE with cycle life (N_{80}) labeled with black lines.	19
Figure 2.4 Schematic of the fritted H-cell used in this work. ¹	20
Figure 2.5 Correlations between (a) reduction potentials vs Li/Li ⁺ and LUMO energies and (b) oxidation potentials vs Li/Li ⁺ and HOMO energies of quinoxaline derivatives. ¹	22
Figure 2.6 Correlation between oxidation potentials and HOMO energies of the dialkoxyarene catholytes	23
Figure 2.7 Capacity vs cycle life plots for (a) Q1 and (b) Q11. Structures shown inset. The decay behavior of Q1 is an abrupt decrease, while Q11 decays with a first order rate.	29
Figure 2.8 Comparison between N_{80} of the dialkoxyarene catholytes at UM and ANL. Q1 shows the largest increase in N_{80} , while Q5 shows no change in N_{80} despite cycling at three times the rate.	32
Figure 3.1 Capacity vs cycle life plots for (a) DDB 5/1/TBAPF ₆ , (b) TEMPO 5/1/LiPF ₆ , and (c) DDB 5/3/LiTFSi. Structures shown inset. The decay behavior of (a) is an abrupt decrease, (b) is a first order decay, and (c) terminates without capacity fade.	43

Figure 3.2 Cycling of a $\text{Li}_{4/3}\text{Ti}_{5/3}\text{O}_4/\text{LiFePO}_4$ coin cell with 0.3 M TEMPO in 0.5 M LiBOB electrolyte. TEMPO was used as an overcharge protector, cycling after the primary redox event. With 25-hour cycles, TEMPO remained cyclable until 124 cycles at around 3100 hours.	45
Figure 3.3 Capacity vs cycle life for the DDB 20/1/ LiPF_6 cell. N_{80} was reached at 1073 cycles, the longest lifetime of any experiment. Experiments of this duration typically terminate due to cell component failure, making this result particularly valuable.	46
Figure 3.4 Pre-cycling CV for the DDB 5/1/ TBABF_4 BE cell. The highlighted peak around 0.4 V shows the active impurity present in all BF_4 salts.	47
Figure 3.5 DFT optimized structures of DBBB coordinated to (a) one Li^+ on a single O atom or (b) on two O atoms. Li is purple, O is red, C is grey, and H is white.	49
Figure 3.6 Capacity vs cycle plots for (a) TEMPO 5/1/ TBAPF_6 and (b) TEMPO 5/1/ LiPF_6 . The 5/1/ LiPF_6 cell has an early onset decay at an N_{80} roughly half of the 5/1/ TBAPF_6 cell.	50
Figure 3.7 Radial distribution function of the TEMPO oxygen to Li^+ distance. LiPF_6 coordinates strongest, while LiBF_4 shows no coordination.	50
Figure 3.8 Capacity vs cycle plots for TEMPO (a) 20/1/ TEABF_4 , $N_{80} = 102$, (b) TEMPO 100/1/ TEABF_4 $N_{80} = 50$, (c) TEMPO 20/1/ LiTFSi , $N_{80} = 328$, and (d) TEMPO 100/1/ LiTFSi , $N_{80} = 241$. N_{80} decreases with greater active material concentrations for TEMPO due to its decay reaction order.	54
Figure 4.1 A graphical representation of the cycling regimes N_q , $N_<$, and $N_>$. $N_<$ extends to the end of the constant capacity plateau, followed by $N_>$ until the capacity cutoff q is reached.	58
Figure 4.2 ϕ vs N_{80} in Equation 15 for different CE at $\eta = 0.5, q = 0.8$. As CE increases, ϕ shows greater variation at low N_{80} . Materials with sufficiently high CE have a theoretical minimum N_{80} .	64
Figure 4.3 ϕ vs N_{80} for the dialkoxyarene catholytes in Table 4.2.	65
Figure 4.4 ϕ vs N_{80} for the DDB experiments in Table 4.3.	70
Figure 4.5 ϕ vs N_{80} for the DBBB experiments in Table 4.4.	70
Figure 4.6 ϕ vs N_{80} for the TEMPO experiments in Table 4.5.	71
Figure 5.1 SISSO construction of its feature space. Mathematical operators are recursively applied to the initial feature space, rapidly increasing the total number	81

of descriptor combinations while maintaining dimensionality. For this example, x and y are variables with different dimensionality, limiting possible combinations.

Figure 5.2 ξ classification of the 52 dialkoxyarene catholytes (blue) and pyridinium anolytes (red) as unstable or stable above or below the dashed line respectively. Experimentally unstable molecules are given faded colors. 85

Figure 5.3 A histogram of 100 absolute PCCs of ξ and ξ' for the 42/10 MC-CV partitions. Clustering of the values near one indicates that the models identified by SISSO do have chemical meaning for ROM stability. 86

Figure 5.4 ξ classification of a selected group of dialkoxyarene catholytes (blue), pyridinium anolytes (red), and TEMPO family catholytes (orange) as unstable or stable above or below the dashed line respectively. Experimentally unstable molecules are given faded colors. Both TEMPO and ATEMPO are stable but are not classified properly by ξ . 88

Figure 5.5 Parity plot of experimental and predicted $t_{\frac{1}{2}}$ of hydrocarbon substituted dialkoxyarene catholytes. 91

Figure 5.6 Parity plot of experimental and predicted $t_{\frac{1}{2}}$ of hydrocarbon substituted dialkoxyarene catholytes. 93

Figure 6.1 Parity plot of experimental and predicted cycle life of metal acetylacetonates with more than 50% of their HOMO orbital density on the metal. 96

Figure 6.2 Parity plot of experimental and predicted cycle life of dialkoxyarene catholytes cycled in a TBAPF₆/MeCN electrolyte at 5 mM active material concentration and 1 C rate. 100

Figure 6.3 Parity plot of experimental and predicted cycle life of dialkoxyarene catholytes cycled in a LiTFSi/MeCN electrolyte at 20 mM active material concentration and 3 C rate. 102

Figure 6.4 Parity plot of experimental and predicted cycle life of DDB, DBBB, and TEMPO cycled at 20 mM active material concentration and 1 C rate. 106

Figure 6.5 Parity plot of experimental and predicted cycle life of DDB, DBBB, and TEMPO cycled at 20 mM active material concentration and 3 C rate. 107

Figure 6.6 Parity plot of experimental and predicted cycle life of DBBB cycled at 20 mM active material concentration and 1 C rate. 109

Figure 6.7 Parity plot of experimental and predicted cycle life of TEMPO cycled at 5 mM active material concentration and 1 C rate. The LiPF ₆ and LiBF ₄ data points are labeled.	110
Figure 6.8 Parity plot of experimental and predicted cycle life of TEMPO cycled at 5 mM active material concentration and 3 C rate. The LiPF ₆ data point is labeled.	111
Figure 6.9 Parity plot of experimental and predicted cycle life of TEMPO cycled at 20 mM active material concentration and 1 C rate. The LiPF ₆ data point is labeled.	112
Figure 6.10 Parity plot of experimental and predicted cycle life of TEMPO cycled at 20 mM active material concentration and 3 C rate. The LiPF ₆ data point is labeled.	113

List of Tables

Table 2.1 Names, structures, oxidation potentials (vs Ag/Ag ⁺), peak height ratios, and CV scans of the nine dialkoxyarene catholytes.	24
Table 2.2 Names, structures, cycle lives, and coulombic efficiencies from BE experiments of the dialkoxyarene catholytes.	28
Table 3.1 Names, structures, oxidation potentials (vs Ag/Ag ⁺), peak height ratios, and CV scans of the three selected catholytes.	39
Table 3.2 Name, structure, active material concentration, cycle rate, supporting salt, cycle life, and coulombic efficiency for DDB. The alkylammonium supporting salts were not cycled at 20 mM active material concentration due to solubility limitations of DDB. Cells that terminated prematurely are marked with an asterisk.	40
Table 3.3 Name, structure, active material concentration, cycle rate, supporting salt, cycle life, and coulombic efficiency for DBBB. Cells that terminated prematurely are marked with an asterisk.	41
Table 3.4 Name, structure, active material concentration, cycle rate, supporting salt, cycle life, and coulombic efficiency for TEMPO. No TEMPO cells terminated prematurely.	42
Table 4.1 Theoretical maximum <i>CE</i> for DDB, DBBB, and TEMPO. <i>CE</i> greater than the theoretical maximum in a BE experiment requires a change in the active material structure.	65
Table 4.2 Names, structures, cycle lives, coulombic efficiencies, and recoveries from BE experiments of the dialkoxyarene catholytes. All values are averages when multiple experiments were performed.	66
Table 4.3 Name, structure, active material concentration, cycle rate, supporting salt, cycle life, coulombic efficiency, and recovery for DDB. The alkylammonium supporting salts were not cycled at 20 mM active material concentration due to solubility limitations of DDB. Cells that terminated prematurely are marked with an asterisk.	67

Table 4.4 Name, structure, active material concentration, cycle rate, supporting salt, cycle life, coulombic efficiency, and recovery for DBBB. Cells that terminated prematurely are marked with an asterisk.	68
Table 4.5 Name, structure, active material concentration, cycle rate, supporting salt, cycle life, coulombic efficiency, and recovery for TEMPO. No TEMPO cells terminated prematurely. $k_{TEMPO} = 0.0129 \text{ h}^{-1}$ was used for all calculations of ϕ .	69
Table 5.1 Name, substituting groups, and experimentally measured half-lives of the Scheme 5.2 dialkoxyarenes.	78
Table 5.2 Name, substituting groups, and experimentally measured half-lives of the Scheme 5.3 dialkoxyarenes.	79
Table 5.3 Name, substituting groups, and experimentally measured half-lives of the Scheme 5.4 pyridiniums.	80
Table 5.4 Molecules and coefficients for the three dialkoxyarene sub-families.	92
Table 6.1 Names, structures, and cycle lives from BE experiments of the dialkoxyarene catholytes originally presented in Chapter 2. Cells were cycled at 5 mM active material, 1 C cycle rate, in TBAPF6/MeCN.	98
Table 6.2 Names, structures, and cycle lives from BE experiments of the liquid dialkoxyarene catholytes.	98

List of Schemes

Scheme 1.1 General chemical structures for (a) dialkoxyarene catholytes, (b) pyridinium anolytes, and (c) (2,2,6,6-Tetramethylpiperidin-1-yl)oxyl (TEMPO) derivatives.	8
Scheme 2.1 Structures of DDB and DBBB. The extended poly-ethylene oxide chains of DBBB increase solubility in polar solvents.	14
Scheme 2.2 The nine dialkoxyarene catholyte names and structures investigated in this chapter.	15
Scheme 2.3 (1) Dialkoxyarene dealkylation and subsequent (2) disproportionation, (3) abstraction, and (4) solvent reactions to form products.	30
Scheme 3.1 Structures of DDB, DBBB, and TEMPO.	35
Scheme 3.2 TEMPO H-abstraction and disproportionation into the N-oxoammonium salt and 2,2,6,6-Tetramethylpiperidin-1-ol.	52
Scheme 5.1 Structures for (a) dialkoxyarene catholytes and (b) pyridinium anolytes.	75
Scheme 5.2 Structure for the dialkoxyarene catholytes in Table 5.1.	78
Scheme 5.3 Structures for the dialkoxyarenes catholytes in Table 5.2.	79
Scheme 5.4 Structures for the pyridinium anolytes in Table 5.3.	80
Scheme 5.5 Structures of TEMPO and ATEMPO. Both molecules are stable, electrochemically active radicals.	87
Scheme 6.1 Structures of DDB, DBBB, and TEMPO.	97

Abstract

Non-aqueous redox flow batteries (NaRFBs) are a promising technology for widespread grid-scale energy storage deployment. Despite their potential for high energy density, current active materials lack the necessary stability and cyclability for scale-up. One class of active materials for NaRFBs are redox active organic molecules (ROMs), which are a focus of recent development due to their low cost and high solubilities compared to other candidate active materials. The research in this thesis seeks to advance of ROM development through characterization of new active materials and development of computational design tools for stability and cyclability. ROM characterization focused on cyclability of the dialkoxyarene ROM catholyte family and (2,2,6,6-Tetramethylpiperidin-1-yl)oxyl (TEMPO). An extensive set of bulk electrolysis (BE) experiments with varying active material concentration, cycle rate, and supporting salt were performed. Two different design strategies for improving dialkoxyarene cyclability were identified: increasing steric hinderance in alkylammonium electrolytes and increasing lithium-coordination in lithium electrolytes. These two strategies and the BE data provide new insight into ROM design and proper selection of electrolytes for cyclability. Computational work used the model building tool Sure Independence Screening and Sparsifying Operator (SISSO) to develop models for screening and prediction of ROMs. A variety of prediction tools for dialkoxyarene and TEMPO cyclability were developed, highlighting the lowest unoccupied molecular orbital (LUMO) energy and the solvation energy as the most important active material descriptors for improving cyclability. Similar tools were developed for dialkoxyarene stability, with the LUMO energy and geometry as the most important factors identified by SISSO. Most significantly, a generalized screening model for stability was developed from data for dialkoxyarene catholytes and pyridinium anolytes. This model is the first generalizable model for any ROM property of interest and provides insight into the unknown factors affecting electrochemical stability. These models provide foundations and methods for the computational design of new ROMs.

Chapter 1

Introduction

1.1 Energy Storage

Demand for reliable electricity supply has increased greatly over the past decades, which is expected to continue with the improving global standard of living. This increasing electricity demand is primarily met by burning of fossil fuels which releases harmful levels of CO₂ in the environment. The greatest challenge with this increase in electrification is reducing the carbon emissions from power generation. Consequently, there is now a shift towards clean renewable energy resources like solar and wind, which are expected to supply ~35% of the total electricity demand by 2050 according to the US Energy Information Administration.¹ However, integrating renewables as a significant portion of our generation profile will lead to grid instability due to the intermittent nature of wind and solar power, the two most widespread and cost-effective renewable technologies. To offset this intermittency, energy storage capacity will need to be installed at a similar rate to fully utilize these renewable resources. In the United States, only ~2% of electricity is supplied from energy storage devices, a number that has remained constant for the past 30 years. However, renewable technologies now account for 19% of the electricity supply,² shown in Figure 1.1. Integration of energy storage enables peak shaving, load shifting, and frequency regulation, improving grid reliability in addition to reducing carbon emissions and costs. Energy storage devices also play an important role in the development of smart grids and decentralized electricity generation.³

Grid-scale energy storage technologies can be classified into four major categories, listed from largest to smallest capacity, mechanical, thermal, chemical, and electrical energy storage.⁴ Mechanical energy storage systems, which are the most mature energy storage technologies, use

kinetic or potential energy as their storage medium. Kinetic energy storage is dominated by flywheels, but is not a significant source of total storage capacity. Pumped hydroelectric storage (PHS) is the dominant form potential energy storage and of installed grid-scale energy storage devices in the U.S., accounting for 94% of the installed energy storage capacity, shown in Figure 1.2.⁵

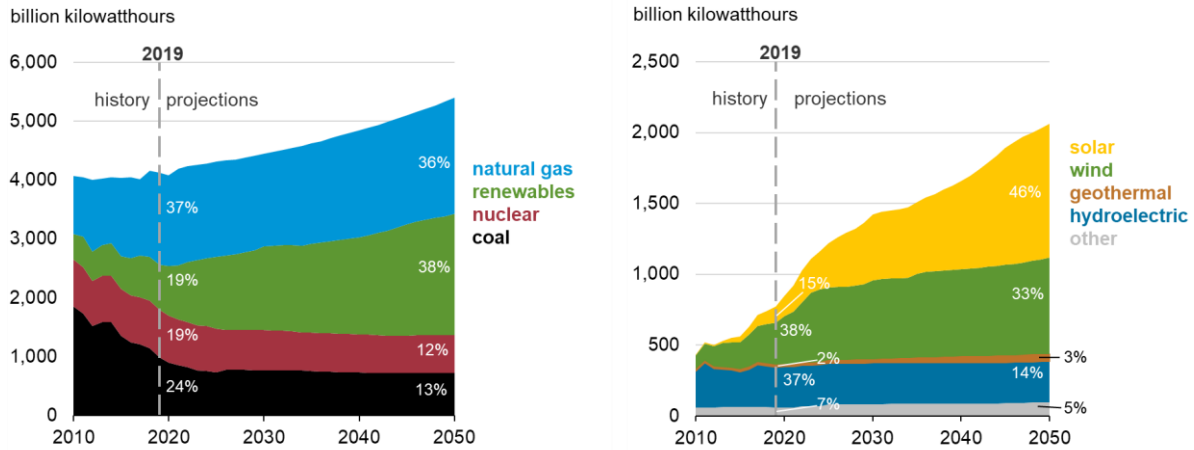


Figure 1.1 U.S. overall and renewable power generation projections until 2050.²

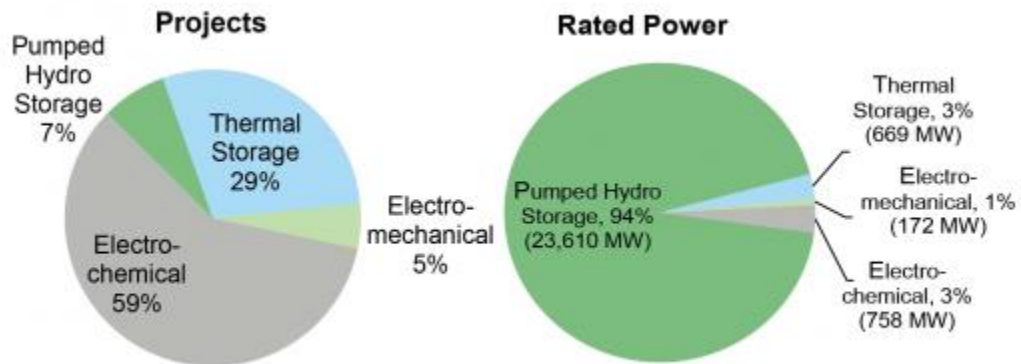


Figure 1.2 U.S. 2020 energy storage capacity, rated power includes announced projects.⁵

PHS systems operate as a reversible dam, pumping water from a lower reservoir to an upper reservoir during “charging” and then releasing the stored water to power turbines during “discharge”. PHS systems have long lifetimes and large capacities, but their cost and geographic limitations restrict use to large scale, which cause significant environmental harm.⁴

Thermal energy storage technologies are a candidate technology aiming to avoid the high costs and geographic limitations associated with PHS. These systems operate by storing heat/cold in various media, which is later extracted for thermal energy or electricity. These systems are already in use for commercial and industrial cooling but have not yet matured as an energy storage technology due to their cost at larger scales.⁶ Mature electrical energy storage technologies are capacitors and super capacitors, both of which have widespread use for frequency regulation, but lack the capacity to replace PHS as a widespread grid-scale energy storage technology.⁷

Chemical energy storage encompasses battery chemistries, which have varying levels of technological maturity. They can range in size and capacity, from coin cell batteries (~0.01 Wh) to redox flow batteries (RFBs) for grid scale storage (~1 GWh). For grid scale applications, mature technologies such as lead-acid and lithium ion batteries are commonly used. However, these technologies have relatively short lifetimes and are significant risks for thermal runaway, a major safety hazard.⁸ One alternative to these technologies are RFBs, which offer improved lifetimes and safety over other batteries while still avoiding the significant cost and geographic limitations of PHS. Research efforts are focused on increasing energy densities and reducing cost of RFBs to make them market viable for grid scale integration.⁹ This dissertation will discuss performance trends and predictions for new non-aqueous RFB (NaRFB) chemistries to expedite materials discovery and characterization.

1.2 Redox Flow Batteries

RFBs are batteries with their electrochemically active species stored in liquid electrolytes, whereas traditional batteries contain their active species at or near the electrode surface. This feature allows RFBs to be constructed with a separate cell stack and storage reservoirs as shown in Figure 1.3. Since the power output is proportional the electrode area and capacity are proportional to the size of the storage reservoirs, RFBs can independently scale power output and capacity. During operation of the battery, the electrolytes are pumped from the reservoirs to the cell stack, where they undergo charge/discharge and are returned to the reservoirs. For convention, the electrolyte which undergoes oxidation during charge is known as the catholyte

and the other is the anolyte. These electrolytes are kept electrochemically isolated by a membrane in the cell stack, which allows transport of non-reactive ions to satisfy charge neutrality in the system while preventing transport of the active species. These membranes are typically inert materials, which can undergo further surface treatments to improve kinetics and reduce resistance.^{10,11}

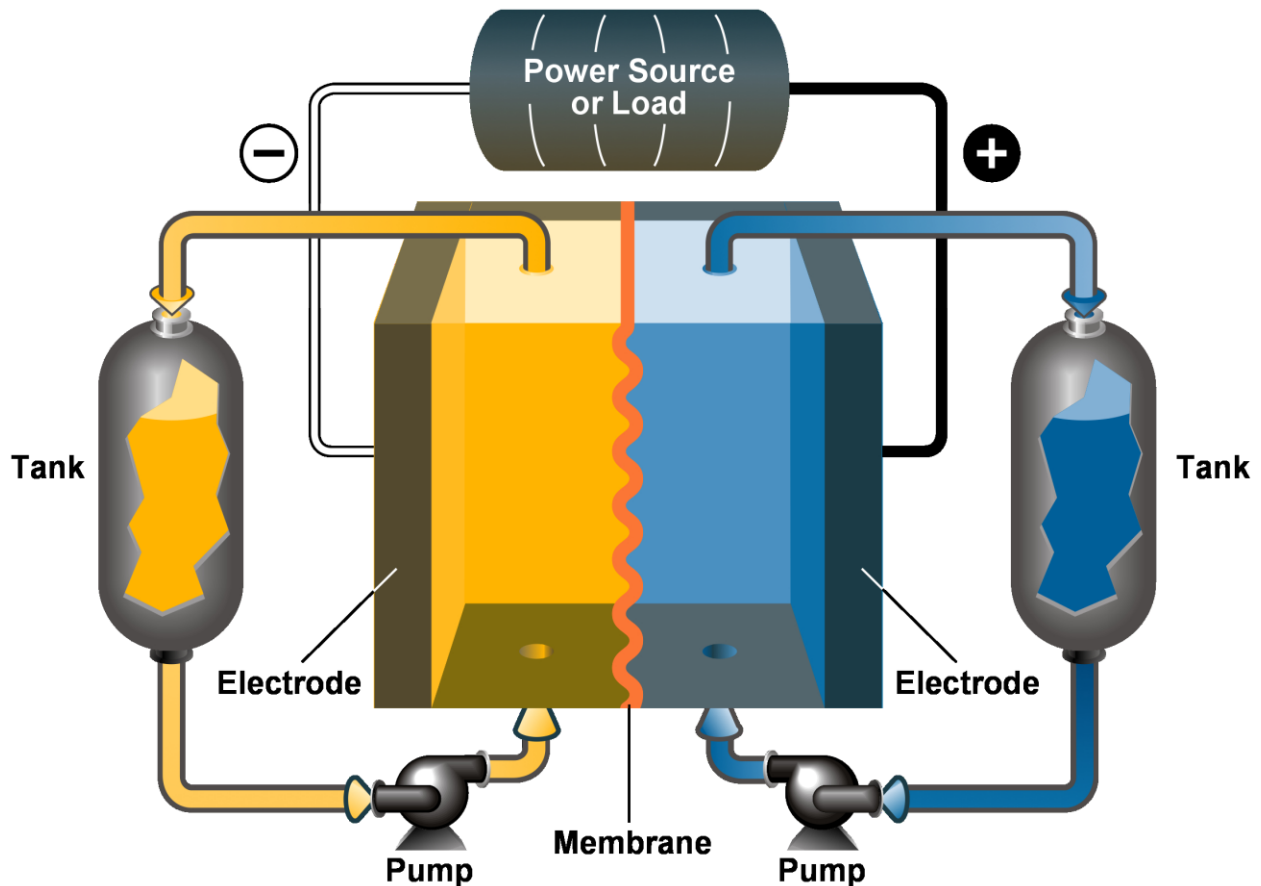


Figure 1.3 Diagram of a redox flow battery.

Overall RFB performance is measured through a variety of metrics. Two commonly used metrics are cycle life (N_q) and energy density. N_q is defined as the number of cycles or amount of time before the battery reaches a lower bound on acceptable capacity, which in this work was chosen as 80% of the initial capacity (N_{80}). Increasing the cycle life of an RFB increases its operational lifetime.

Energy density measures the energy per unit volume of electrolyte and is given in Equation 1.1

$$E = nFV_{cell}C_{active} \quad (1.1)$$

Where n is the number of electrons transferred, F is Faraday's constant, V_{cell} is the cell voltage during discharge, and C_{active} is the concentration of active species. Increasing energy density of an RFB decreases the necessary electrolyte volume and reservoir size. Commercially available RFBs have long cycle lives (>10,000) but low energy densities (up to 25 Wh/L).^{12,13} Further installation and integration of RFBs requires significant improvements to energy density.

1.2.1 Aqueous Redox Flow Batteries

The first RFB chemistry was developed in the 1930's, an aqueous RFB (AqRFB) with a variety of metal redox couples as possible active materials.¹⁴ The first modern RFB was developed at NASA after improvements to cell components in the 1970's with Fe^{2+}/Fe^{3+} and Cr^{2+}/Cr^{3+} halide solutions as the catholyte and anolyte respectively, but was plagued with high crossover and subsequent capacity fade of the anolyte.¹⁵ Further development around various metal redox couples led to the invention of the vanadium RFB (VRFB) in the 1980's at the University of South Wales. This design used sulfuric acid electrolytes with V^{2+}/V^{3+} and V^{4+}/V^{5+} as the catholyte and anolyte respectively, eliminating contamination from crossover.¹⁶ The VRFB is the most commercially viable RFB to date, with a cycle life up to 20,000 and efficiencies up to 85%, but energy densities of only 25 Wh/L.¹³ Energy densities for the system are limited by the limited voltage window of water (1.23 V) and the low solubility of vanadium (1.7 M), which also limits the system to a narrow range of operating temperatures (10 – 40 °C).¹⁷ Development of VRFBs is ongoing, with a primary focus on increasing efficiency and increasing solubility. Efficiency has been improved by optimization of cell components and some electrode treatments to reduce overvoltage.¹⁸⁻²¹ New electrolytes have also been investigated to increase the solubility of vanadium in the system.^{22,23}

Several other AqRFB chemistries are in various stages of development. More mature technologies include the zinc bromine RFB^{24,25} and zinc cerium RFB.^{26,27} New active material development is also an active area of research, with efforts focused on redox active organic molecules (ROMs) for their low cost.^{28,29} However, these efforts are still gated by the limited voltage window of water.

1.2.2 Non-Aqueous Redox Flow Batteries

Current construction and integration of redox flow batteries is limited by their high cost per kilowatt hour. A capital cost target for widespread integration set by the Department of Energy is 150 USD/kWh, which PHS and lithium ion batteries are approaching.^{30,31} Redox flow batteries are still significantly behind this target, current VRFB systems cost 500 USD/kWh assuming a 4 hour discharge.³¹ One possible avenue of reducing costs is to move away from water and its low voltage window to non-aqueous solvents, which have voltage windows up to 6 V.³² This wider voltage window can utilize many new chemistries with improved solubilities, increasing theoretical energy density drastically. An additional benefit of these systems is more tunability with the larger range of supporting salts and solvents to choose from. Current non-aqueous RFBs (NaRFBs) are limited to the bench-scale, however they have seen an increase in research focus due to their potential to reach higher energy densities at lower costs than aqueous RFBs.

1.2.2.1 Non-aqueous Electrolytes

A wide variety of solvents exist for non-aqueous electrochemistry, which allows for a wide degree of control over properties such as viscosity, operational temperature, and voltage window, among others. Non-aqueous solvents require a supporting salt to reach necessary ionic conductivities for electrochemical activity, although there are a wide variety of support salts to choose from.³³ Non-aqueous electrolyte development has primarily focused on the lithium-ion (Li-ion) battery space, with significant developments in liquid electrolyte chemistries.^{34–36} These electrolytes consist of a carbonate solvent or mixture of carbonate solvents, dimethyl carbonate (DC), ethylene carbonate (EC), propylene carbonate (PC), among others; and a lithium-based supporting salt like lithium tetrafluoroborate (LiBF_4), lithium hexafluorophosphate (LiPF_6), or lithium perchlorate (LiClO_4). Early NaRFB research utilized these Li-ion electrolytes, however acetonitrile (MeCN) has steadily grown as the solvent of choice due to the variety of benefits it offers over carbonate solvents including lower viscosity and greater supporting salt solubility.^{33,34} For these reasons, all experiments in this thesis used MeCN. However, MeCN does not see

industrial use as a battery solvent due to the presence of water in the purified solvent, which currently cannot be removed at an industrial scale. Industrially dried acetonitrile can be further dried at laboratory scale, making it suitable for use with water-incompatible materials.³⁷

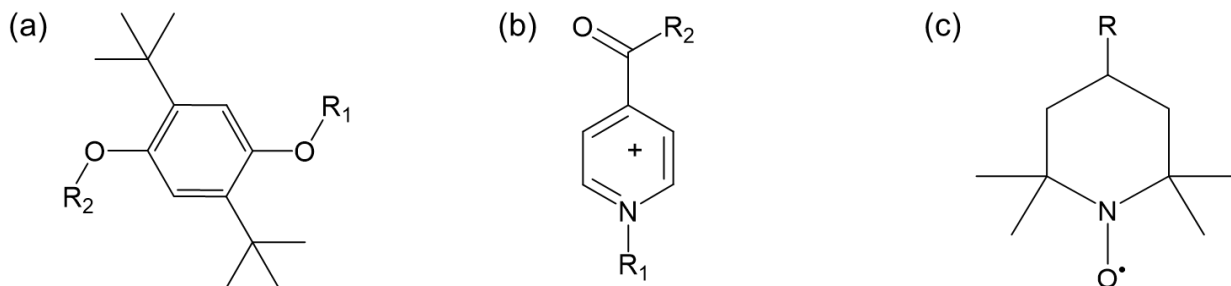
Supporting salts consist of an anion and cation that dissociate in the solvent to provide the necessary conductivity for bulk electrochemical reactions. The most commonly used anions are BF_4^- , PF_6^- , ClO_4^- , and bis(trifluoromethanesulfonyl)amide (TFSi^-), each with their advantages and disadvantages. BF_4^- has the smallest ionic radii and therefore the largest limiting molar ionic conductivity of available anions.³³ When BF_4^- is combined with lithium as a cation in LiBF_4 , it dissociates poorly in MeCN and is one of the most expensive supporting salts.³⁵ PF_6^- is more dissociative than BF_4^- but is known to react with water to produce HF, although the presence of HF may stabilize electrodes in Li-ion batteries.³⁵ ClO_4^- is one of the most soluble anions, but oxidizes non-aqueous solvents at high current loads or high temperatures, a significant safety hazard.³³ TFSi^- provides a balance of properties with BF_4^- and PF_6^- , but has shown instability in ether- and sulfone-based electrolytes.^{33,35,38} This thesis used BF_4^- , PF_6^- , and TFSi^- as supporting salt anions.

There are only two types of cations used in NaRFB research, alkylammonium and lithium, both of which are used in this thesis. The two alkylammonium cations used here are tetrabutylammonium (TBA^+) and tetraethylammonium (TEA^+), which provide high conductivities.³⁹ Lithium salts are known to dissociate poorly in some solvents, and strongly interact with some active species.^{35,40,41} Despite this, the interaction can often be beneficial, which will be discussed in Chapters 2 and 3.

1.2.2.2 Active Species

NaRFBs research is primarily focused on active material development and characterization, as scale-up and performance are currently gated by the low stability and cyclability of proposed active species. There are four main classes of active materials for NaRFBs, ordered by molecular size from smallest to largest are ROMs, metal coordination complexes (MCCs), redox active polymers (RAPs), and redox active colloids (RACs).

ROMs are promising for NaRFB research because of their low costs, high solubility, and easy tunability of chemical and electrochemical properties.⁴² Structures for a few common ROMs are shown in Scheme 1.1.



Scheme 1.1 General chemical structures for (a) dialkoxyarene catholytes, (b) pyridinium anolytes, and (c) (2,2,6,6-Tetramethylpiperidin-1-yl)oxyl (TEMPO) derivatives.

ROM development was driven by active materials for overcharge protection in Li-ion batteries.^{43,44} The high redox potential and stability of these molecules led to their use as NaRFB catholytes. The primary family of focus in this thesis, the dialkoxyarene family, was one of the first to be investigated for NaRFB applications. This family exhibits high redox potentials (~ 0.8 V vs Ag/Ag⁺ in MeCN) and has been modified for high solubilities (>2 M in carbonate solvents).^{45,46} Another ROM family of interest is (2,2,6,6-Tetramethylpiperidin-1-yl)oxyl (TEMPO) and its 4-substituted derivatives. These families exhibit high redox potentials (~ 0.4 V vs Ag/Ag⁺ in MeCN) and exceptional solubilities (>5.2 M in carbonate solvents);⁴⁷ TEMPO features primarily in Chapter 3 of this thesis. More recently, anolyte ROMs have been introduced. The two main families of anolytes are pyridinium anolytes and benzothiadiazoles (BzNSN).^{48,49} These families have high stabilities and low redox potentials (~ -2.2 V vs Ag/Ag⁺), but have yet to approach reduction potentials near lithium (-3.2 V vs Ag/Ag⁺ in MeCN).

Redox active metals are the dominant active material in AqRFBs, but they are insoluble in non-aqueous solvents. These metals can be functionalized with organic ligands to create soluble metal coordination complexes (MCCs). MCCs can exhibit multiple redox events which are tunable by changing the coordinated ligands. Bipyridine MCCs were the first family of MCCs proposed for NaRFBs with four redox events within their voltage window, however solubility was limited to 0.2 M in MeCN.⁵⁰ Acetylacetonate MCCs were the next major family investigated, with increased

solubility (2.0 M) and improved cyclability (~200 cycles).⁵¹⁻⁵³ Of particular note, these molecules were the first with demonstrated correlations of structure to both solubility and cyclability.⁵³ Most recently, a systematic investigation of metal centers and ligands identified ligand denticity as a key factor in MCC cyclability, with tridentate ligands out-cycling bidentate ligands due to stronger attachment to the metal center.⁵⁴

Redox active polymers and redox active colloids are newer types of molecules that evolved from ROM development and a desire to reduce crossover of active species.^{55,56} They consist of functionalized ROMs attached to a polymer or colloid backbone, greatly increasing the size and number of redox events of a single molecule.

1.3 Research Motivation

Initial NaRFB active material development was focused on improving solubility, which has resulted in established functionalization strategies. A larger focus is now placed on stability and cyclability, which govern the performance of active materials and are not well understood.

1.3.1 Stability

Stability of an active species measures its ability to remain in the charged state. This governs the theoretical coulombic efficiency of the active material and the charge retention of an RFB. Stability is a chemical property of the active species, but can be influenced by the supporting salt and solvent environment. Shelf-life studies are the simplest way of evaluating stability, although recent studies have used resonance spectroscopy for more detailed results.

1.3.2 Cyclability

Cyclability of an active species measures its ability to remain stable while cyclically donating and accepting electrons, the determining factor of RFB lifetime. Cyclability is greatly influenced by external factors, including electrolyte interactions and experimental conditions of cycling experiments. The two main ways to characterize cyclability are bulk electrolysis (BE) and flow cell cycling, this work focuses on BE. The primary experimental component of this research

systematically adds to the limited quantity of cyclability data available to develop a greater understanding between cyclability and the various experimental factors that influence it.

1.3.3 Prediction

Synthesis and characterization of new active materials are time-consuming processes and are responsible for the lackluster rate of new active materials development. In addition, there is no guarantee of finding a promising active material from a synthesized family, as the performance of materials is seemingly random. Computational screening of materials has so far only been possible for redox potential.⁵⁷ Stability and cyclability screening have been shown for a couple non-generalizable cases,^{48,53} but more generalized prediction has been non-existent. The primary computational part of my research focuses on developing predictive models for active material stability and cyclability based on structural and electrochemical descriptors obtained computationally. These models can greatly reduce the number of molecules that are synthesized and characterized through pre-screening of candidate materials, increasing active material discovery throughput.

1.4 Research Summary and Goals

This thesis is split into two parts, an experimental section in Chapters 2-4 and a computational section in Chapters 5 and 6. The experimental section will discuss the characterization of ROM catholyte active materials. The experimental section reports and discusses the cyclability results for two main thrusts: characterizing additions to the dialkoxyarene family and a systematic investigation of experimental factors affecting cyclability. These results greatly expand the set of available cyclability data and provide insight into the complexity of cyclability characterization, guiding characterization procedures for future active materials. Lastly, a model for a new cyclability metric, recovery, is developed and used to provide additional insight into the reported results. The computational section of this thesis discusses the use of Sure Independence Screening and Sparsifying Operator (SISSO) for model development of general ROM stability and the BE experiments. These models will help increase active material

discovery throughput by providing previously non-existent computational screening methods for performance.

1.5 Chapter Summaries

1.5.2 Chapter 2: A Cycling Comparison of Dialkoxyarene Catholytes

Chapter 2 discusses the dialkoxyarene family of ROMs and their development into active materials for RFBs. A series of nine dialkoxyarenes with new functional group variations are presented and characterized by cyclic voltammetry and BE. Oxidation potentials, peak height ratios, cycle life, and coulombic efficiencies are reported for each active material. Trends and relationships for oxidation potentials, cycle life, and coulombic efficiency are discussed. Additionally, the degradation mechanism of these dialkoxyarenes is identified. Steric hinderance was identified as a significant descriptor of cyclability and its effects on decay are demonstrated. Lastly, the significance of experimental conditions and electrolyte choice are identified.

1.5.3 Chapter 3: Factors Affecting Bulk Electrolysis Cycling Performance

Chapter 3 discusses the experimental effect of active material concentration, cycle rate, and supporting salt choice on cyclability. To investigate these effects, a total of 66 BE experiments were performed on three ROM active materials. From the BE experiments, supporting salt choice was found to be as impactful as active material selection for cyclability and should be considered for all ROM characterization. Li^+ coordination to the ROMs significantly improved cyclability, while an active impurity in BF_4^- salts made them incompatible with dialkoxyarene ROMs. Further investigation of Li^+ coordination allowed us to hypothesize possible mechanisms for improved cyclability. Lastly, the impact and mechanism of active material concentration on TEMPO cyclability was identified.

1.5.4 Chapter 4: A Kinetic Model for Redox Organic Active Material Cycling

Chapter 4 follows the derivation of a kinetic model for BE cycling. This model was developed as an alternative metric for performance and quantifies the recovery, ϕ , of an active material. ϕ is a metric for how much decay of a charged active material returns to the neutral

state and is a kinetic indicator of the quantity of active material decay. ϕ is calculated for all BE experiments in Chapters 2 and 3. The derivation of ϕ also led to an expression for the maximum theoretical coulombic efficiency, which can be used to identify active material/supporting salt combinations which coordinate. Lastly, ϕ was used to gain additional insights in to the BE experiments from Chapter 3.

1.5.5 Chapter 5: Stability Predictions for ROMs

Chapter 5 introduces three models for computational stability prediction of ROMs developed with Sure Independence Screening and Sparsifying Operator. The first model is a generalized ROM stability screening model, which categorizes stable and unstable dialkoxyarene catholytes and pyridinium anolytes, allowing synthesis and characterization efforts to be focused on stable molecules. This model is the first multi-family stability model for any active materials and identifies a non-obvious, common feature for ROM stability. The second and third models are predictive models for hydrocarbon substituted-dialkoxyarenes and a multi-task learning, general dialkoxyarene model.

1.5.6 Chapter 6: Cyclability Predictions for Catholyte ROMs

Chapter 6 continues the modeling efforts in Chapter 5 by focusing on cyclability. Nine SISO developed models for computational cyclability prediction of dialkoxyarenes and TEMPO are introduced, although none of these models is generalizable to all ROMs. Two models are developed for cyclability of hydrocarbon substituted-dialkoxyarenes in different electrolytes. The additional seven models focused on predicting the effects of active material concentration, cycle rate, and supporting salt on cyclability. Model development was severely hampered by the limitations of the descriptor sets, which did not account for active material-supporting salt interactions. These models provide a basis to predict cyclability with varying experimental conditions, however additional experimental work is needed to confirm their robustness.

Chapter 2

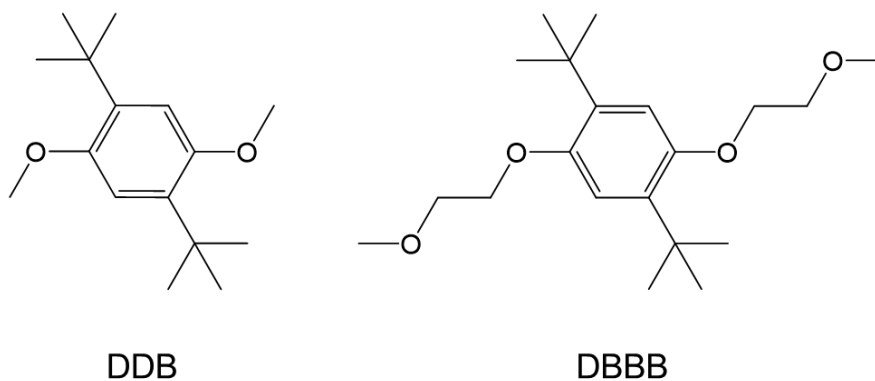
A Cycling Comparison of Dialkoxyarene Catholytes

2.1 Background and Approach

Non-aqueous redox flow batteries (NaRFBs) are an emerging technology for grid scale energy storage applications. However, significant progress in active material, electrolyte, and membrane development are necessary before they become competitive with current technologies.^{3,58} Active materials for NaRFBs need to exhibit electrochemical reversibility, high solubility, high stability, and high cyclability to move beyond laboratory scale investigation. Currently, there are no active materials that meet all these criteria. New materials discovery is currently limited by time intensive materials synthesis and characterization. Compounding this effect, there is still limited information on the molecular characteristics that impact stability and cyclability. Increasing throughput of molecular discovery requires a greater understanding of structural features impacting active material performance and screening candidate molecules computationally to increase the productivity of laboratory work.

Work in this thesis is focused on using promising redox active organic material (ROM) families to identify key descriptors for performance through laboratory characterization and computational tools.

Dialkoxyarene molecules were among the earliest ROMs investigated for use in non-aqueous redox flow batteries,⁴³ the two primary dialkoxyarene molecules, 1,4-Di-*tert*-butyl-2,5-dimethoxybenzene (DDB) and 1,4-Di-*tert*-butyl-2,5-bis (2-methoxyethoxy)benzene (DBBB), are shown in Scheme 2.1.



Scheme 2.1 Structures of DDB and DBBB. The extended poly-ethylene oxide chains of DBBB increase solubility in polar solvents.

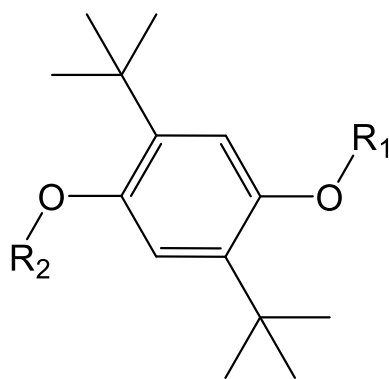
Their use for charge storage was initially investigated for Li-ion battery overcharge protection, where DDB cycled for thousands of hours. However, DDB and other dialkoxyarene molecules of the time had low solubility (8 mM in carbonate solvents), limiting their practicality.⁴³ To increase solubility, DDB was functionalized with poly-ethylene oxide chains, creating DBBB with greater solubility (0.4 M in PC).⁴⁶ DBBB was the first dialkoxyarene to be investigated in NaRFB applications, with further development of the family focused on NaRFB applications thereafter.^{45,59,60} While a number of these materials have been cycled, many are not electrochemically reversible, which greatly reduces the data available.^{59,60}

In this chapter, I present a newly synthesized series of dialkoxyarene molecules, which were characterized by cyclic voltammetry (CV) and bulk electrolysis (BE) to assess their electrochemical reversibility and cyclability. Further, I discuss cyclability trends and the decay mechanism. Most importantly, I discovered the impact of experimental conditions on cyclability performance, in particular supporting salt choice. This work also establishes the importance of steric hinderance for improved cyclability in the dialkoxyarene family and identifies the impact of supporting salt choice on cyclability.

2.2 Experimental

2.2.1 Molecule Set

The nine dialkoxyarene molecules investigated in this chapter are presented in Scheme 2.2.



Molecule	Alternate Names	R ₁	R ₂
Q1	DiMe, DDB	Me	Me
Q2	MeEt	Me	Et
Q3	MeiPr	Me	<i>iso</i> -Pr
Q5	MeBn	Me	Bn
Q6	DiEt	Et	Et
Q7	DiiPr	<i>iso</i> -Pr	<i>iso</i> -Pr
Q9	DiBn	Bn	Bn
Q10	MesBu	Me	<i>sec</i> -Bu
Q11	DisBu	<i>sec</i> -Bu	<i>sec</i> -Bu

Scheme 2.2 The nine dialkoxyarene catholyte names and structures investigated in this chapter.

These molecules were synthesized at Argonne National Laboratory (ANL) and shipped in inert atmospheres to the University of Michigan (UM).

2.2.2 Cyclic Voltammetry

Cyclic Voltammetry experiments provide a rapid characterization of basic electrochemical behavior. As implied by the name, a CV scan increases the applied voltage to an electrode of known surface area at a fixed scan rate, and then reverses the direction of the applied voltage to the start point, in a cyclical experiment. Redox events are marked by an increase in the magnitude of current, oxidation in the positive direction and reduction in the negative direction, as per the IUPAC convention. A sample CV scan can be found in Figure 2.1.

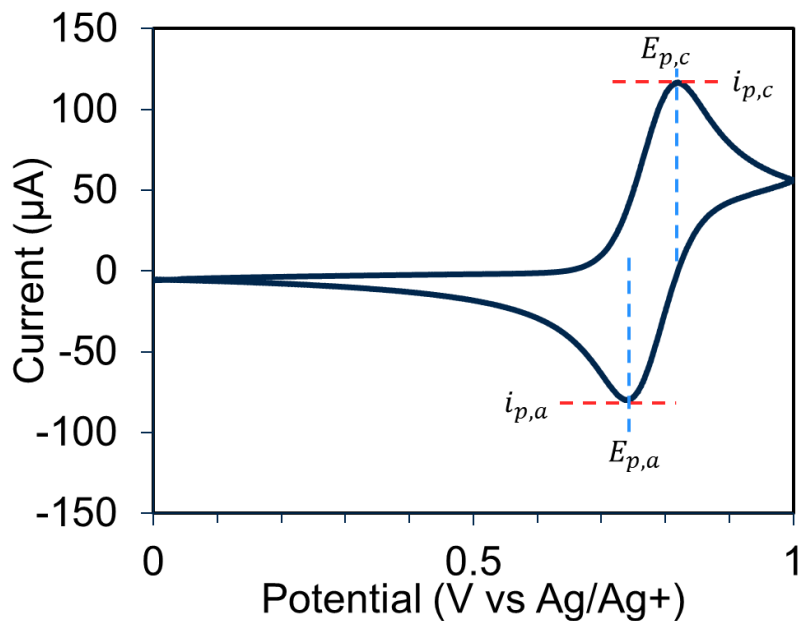


Figure 2.1 Example CV with cathodic and anodic peak potentials ($E_{p,c}$ and $E_{p,a}$) and peak heights ($i_{p,c}$ and $i_{p,a}$) labeled with blue and red dashed lines, respectively. Scans were taken starting at a potential of 0 V to a termination point of 1 V, where they reversed direction.

A CV scan provides information on the number of redox events, their standard potentials, reversibility, diffusivity, and kinetics. The standard potential of a redox couple is defined as the average of the anodic and cathodic potentials ($E_{p,a}$ and $E_{p,c}$). For an ideal, reversible system, the peak separation between $E_{p,a}$ and $E_{p,c}$ is $\frac{59}{n}$ mV, where n is the number of electron transfers. Larger peak separation values are indicative of slow kinetics and/or high solution resistance; non-aqueous electrochemistry typically falls into the second category due to low solvent conductivity, with typical peak separation values in this work around 70 mV for one electron transfer. The peak height ratio $\frac{i_{p,a}}{i_{p,c}}$ provides a quantification of reversibility, with a perfectly reversible redox event returning unity. Diffusion coefficients and reaction rate constants can be measured by conducting CVs at a variety of scan rates and applying the Randles-Sevcik equation. In a full flow cell, diffusivity can become a limiting factor for materials utilization and achievable power densities,⁶¹ however, for the experiments in this thesis it is neglected due to low active material concentrations. Slow reaction kinetics lead to an increase in overpotential seen in bulk electrolysis (BE) experiments, but non-aqueous electrolytes generally exhibit near-instant

kinetics.¹³ CV requires only a small amount of active material and is rapid, an ideal experiment for basic characterization. However, only material near the surface of the electrode undergoes redox reactions and measured reversibility is not necessarily indicative of bulk reversibility.

For this work, all materials storage, solution preparation, and electrochemical characterization were performed in an argon-filled glove box ($O_2 < 0.3$ ppm, $H_2O < 0.5$ ppm). CVs were measured in-situ in fritted, three electrode bulk electrolysis cells with a 3.0 mm diameter glassy carbon (GC) working electrode (BASi), a reticulated-vitreous carbon (RVC) counter electrode (Duocell, 100 PPI), and Ag/Ag⁺ quasi-reference electrode (BASi). The GC electrode was polished in air with micron alumina oxide polishing paper (Fiber Instrument, 9 micron and 0.3 micron) and water. The reference electrode was a fritted chamber containing 10 mM of silver nitrate (AgNO₃) or silver bis(trifluoromethanesulfonyl)amide (AgTFSi) in MeCN and a silver wire. A BioLogic VSP potentiostat recorded scans at a rate of 100 mV/s. Solutions contained either 5 or 20 mM of the active species with 500 mM of tetrabutylammonium hexafluorophosphate (TBAPF₆) or lithium bis(trifluoromethanesulfonyl)amide (LiTFSi) (> 99%, Sigma Aldrich) in 10 mL of MeCN (Acros Organics).

2.2.3 Bulk Electrolysis

Bulk electrolysis experiments provide a single-molecule evaluation of active material cyclability. As also implied by the name, bulk electrolysis experiments alter the oxidation state of the bulk electrolyte solution. This technique is used to quantify the cyclability of the active material and provides cursory information about possible decay mechanisms. BE requires limited solution volumes and can be performed at a wide variety of concentrations (2 mM – 100 mM), potentially minimizing the use of active material. The cyclability obtained from BE is typically a lower bound, as crossover from the uncontrolled counter chamber or other physical effects can occur.

Cycling experiments can be performed at constant current measuring the voltage response, or constant voltage measuring the current response. This work uses galvanostatic (constant current) cycling experiments, which provide greater information about the redox events being accessed. In a galvanostatic bulk electrolysis, the working electrode is held at

constant current, appropriate cutoffs (capacity, potential, time) are used to repeatedly alternate between charge and discharge. A sample potential response can be found in Figure 2.2.

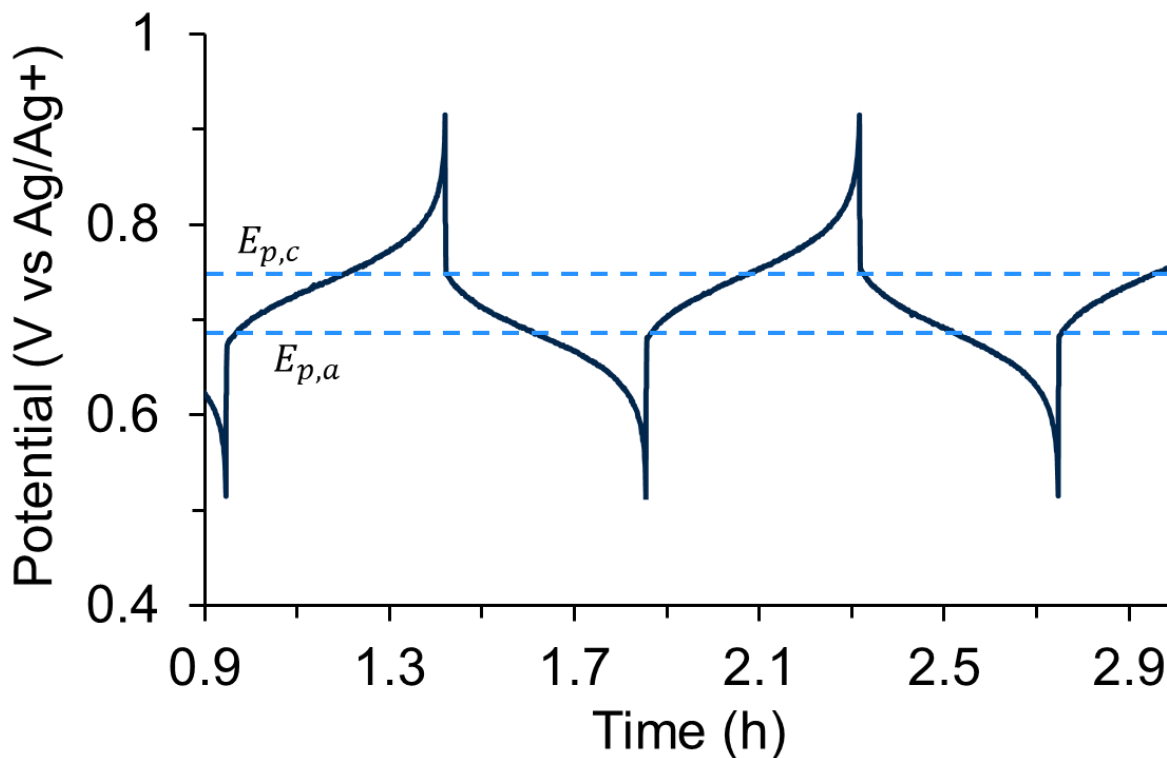


Figure 2.2 Example BE current response with cathodic and anodic peak potentials ($E_{p,c}$ and $E_{p,a}$) labeled with blue dashed lines. $E_{p,c}$ is located at the halfway point of oxidation and $E_{p,a}$ is located at the halfway point of reduction.

The primary metric of interest from BE is cyclability, which is typically defined as the cycle life or the time of cycling. Cycle life (N_q) in this work is defined as the number of cycles before the discharge capacity reaches 80% of its theoretical value (N_{80}), shown in Figure 2.3.

Cycling efficiencies (coulombic, voltaic, and energy) can also be calculated, but only coulombic efficiency (CE) has meaning due to the use of a reference electrode. CE is the ratio of discharge capacity to charge capacity and provides information on losses in the cell due to irreversibility/instability of the redox event and crossover.

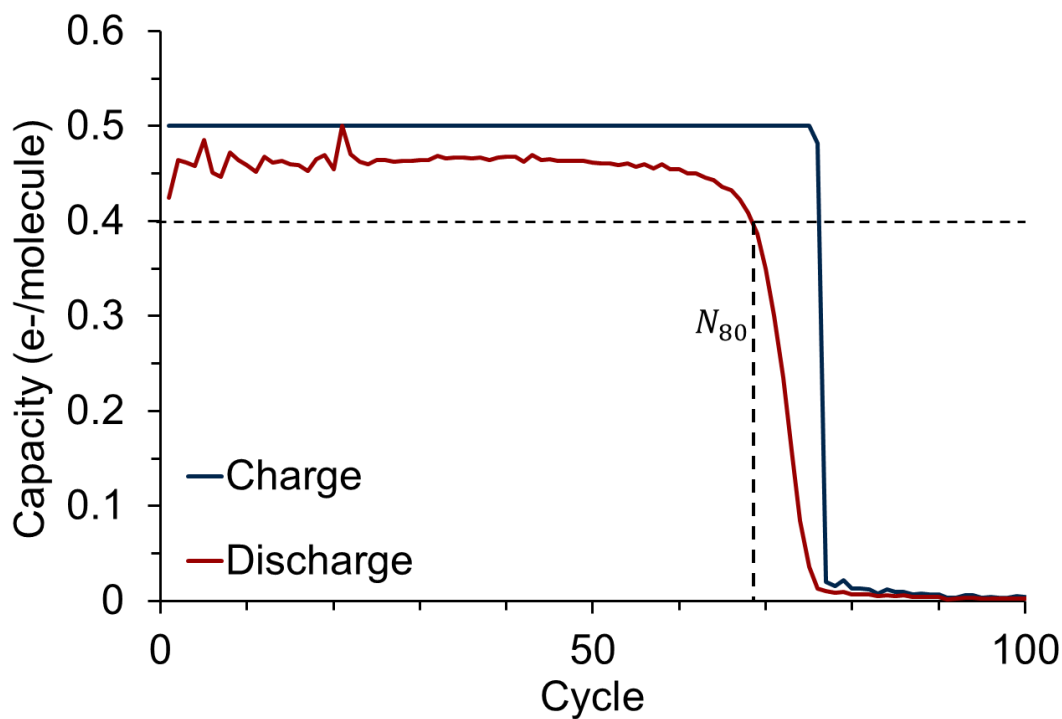


Figure 2.3 An example capacity vs cycle graph from BE with cycle life (N_{80}) labeled with black lines.

All BE experiments were performed in a fritted glass H-cell, shown in Figure 2.4. Two 5 mL chambers are separated by a 1.6 μm glass frit (frit porosity: P5, Adams and Chittenden) that eliminates the need for a membrane. This is particularly important in non-aqueous electrochemistry, as many membranes are incompatible with non-aqueous solvents.⁹ RVC is used for both the working and counter electrode with a Ag/Ag⁺ quasi-reference electrode. Both cell chambers are stirred continuously during cycling; a separate port for an in-situ CV electrode is provided in the cell design. All solutions were composed of either 5 or 20 mM of the active species with 500 mM of TBAPF₆ or LiTFSi (> 99%, Sigma Aldrich) in 10 mL of MeCN (Acros Organics). A Biologic VSP potentiostat was used to provide a constant current. Three sets of cutoffs were used, a potential cutoff set around the redox event (± 200 mV for TBAPF₆ experiments, 0 to 1.6 V for LiTFSi experiments), a state of charge (SOC) cutoff to 50% theoretical SOC, and a time cutoff if any of the previous two cutoffs failed. A 3.0 mm diameter GC electrode was used to record CVs before and after cycling.

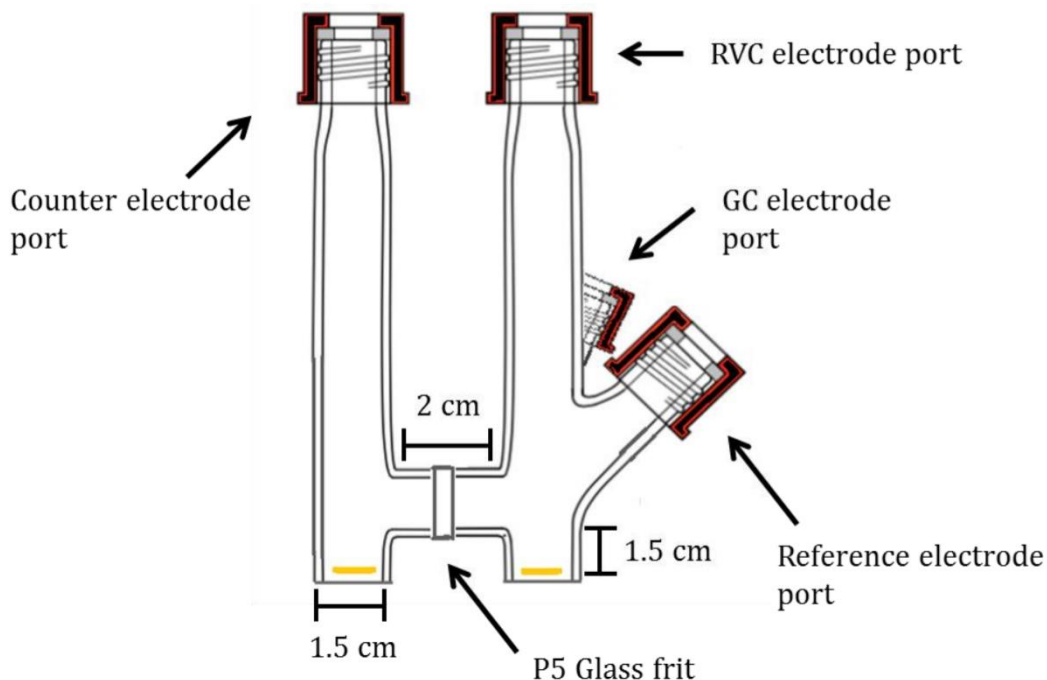


Figure 2.4 Schematic of the fritted H-cell used in this work.⁶²

2.2.4 Density Functional Theory

Density Functional Theory (DFT) is the most common method for electronic structure calculations, providing a balance between accuracy and resource requirements.⁶³ DFT solves the Schrödinger equation:

$$H\Psi = E\Psi \quad (2.1)$$

Where H is the Hamiltonian operator, Ψ is the wavefunction, and E is the energy. The wavefunction is generated by the positions of the system nuclei and electrons, where the electrons are described as waves and their positions are interpreted as molecular orbitals. Very simple systems have an analytical solution to the Schrodinger equation, but for systems of any practical use, simplifications must be made. The most elegant of these simplifications was discovered by Hohenberg and Kohn in 1964, which solely uses electron density to determine the Hamiltonian, and is the birth of DFT.^{64,65}

There are a variety of different first-principles methods used to generate the molecular orbital shapes (basis sets) and density functionals (Functionals). Basis sets commonly consist of a series of gaussian type orbitals (Gaussians) describing the molecular orbitals. For the calculations in this thesis, the 6-31G(d) basis set is used.⁶⁶ This set provides a good balance between accuracy

and computational expense for systems where long-range interactions are not critical.⁶³ Similar to the variety of basis sets, there are numerous functionals to choose from. Functionals can be based solely on DFT approximations or combine DFT approximation and Hartree-Fock wavefunction theory to form a hybrid functional. The hybrid functional Becke, three-parameter, Lee-Yang Parr (B3LYP)⁶⁷ is utilized throughout this thesis. The combination B3LYP/6-31G(d) is commonly used for calculating structures and energies for organic and other small molecules.^{57,68} All DFT modeling in this Chapter was performed with Gaussian09 on computing resources provided by UM Advanced Research Computing.⁶⁹

2.2.4.1 Standard Potential Calculation

Theoretical standard potentials can be calculated from a thermodynamic cycle combined with DFT predictions. However, this procedure is computationally expensive, requiring optimized structures for the molecule and its oxidized/reduced state in vacuum and in solution. Each of these optimizations requires additional thermal corrections, requiring frequency calculations. An alternative to this method is to calculate highest occupied/lowest unoccupied molecular orbital (HOMO/LUMO) energies, which only require optimization of the neutral structure. As shown in Figure 2.5, (a) LUMO and (b) HOMO energies have been correlated to standard potentials for quinoxaline derivatives, as well as metal coordination complex families.^{53,57}

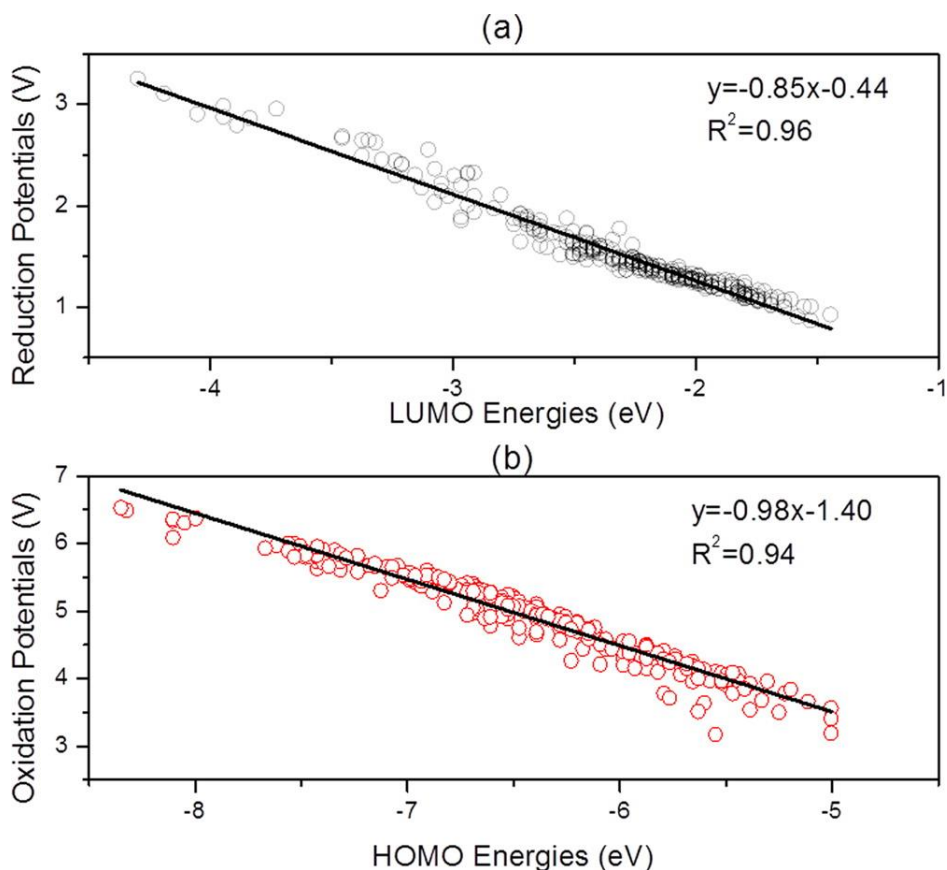


Figure 2.5 Correlations between (a) reduction potentials vs Li/Li⁺ and LUMO energies and (b) oxidation potentials vs Li/Li⁺ and HOMO energies of quinoxaline derivatives.⁵⁷

2.3 Results and Discussion

2.3.1 Electrochemical Reversibility and Oxidation Potentials

The first aim of this study was to evaluate the electrochemical reversibility of the new set of dialkoxyarene active materials. To perform this evaluation, the nine dialkoxyarene molecules underwent CV at a concentration of 5 mM with 500 mM of TBAPF₆ in 10 mL of MeCN. A scan rate of 100 mV/s was used, and the fourth scan out of five was selected. No significant differences in electrochemical reversibility were identified, all nine molecules exhibited consistent and reasonable peak height ratios. CV scans, peak height ratios, and experimentally determined oxidation potentials are presented in Table 2.1. The small variation in potential between each molecule is expected given their structural similarity. This data reveals an inverse correlation between peak height ratio and potential, or more reversible molecules have lower potentials. A similar relationship exists between chemical stability of pyridinium anolyte molecules and their

reduction potential,⁴⁸ which disappointingly confirms that molecules that enable greater cell potential are more unstable.

Similar to the correlation developed for quinoxaline derivatives,⁵⁷ experimental oxidation potentials were correlated with the HOMO energies of the DFT optimized neutral structures, resulting in Figure 2.6. Albeit with much less data, these nine dialkoxyarene molecules have a similar relationship between oxidation potential and HOMO energies as the quinoxaline derivatives. This relationship has also been demonstrated for acetylacetonate metal coordination complexes (MCCs),⁵³ and looks to be further generalizable with this result.

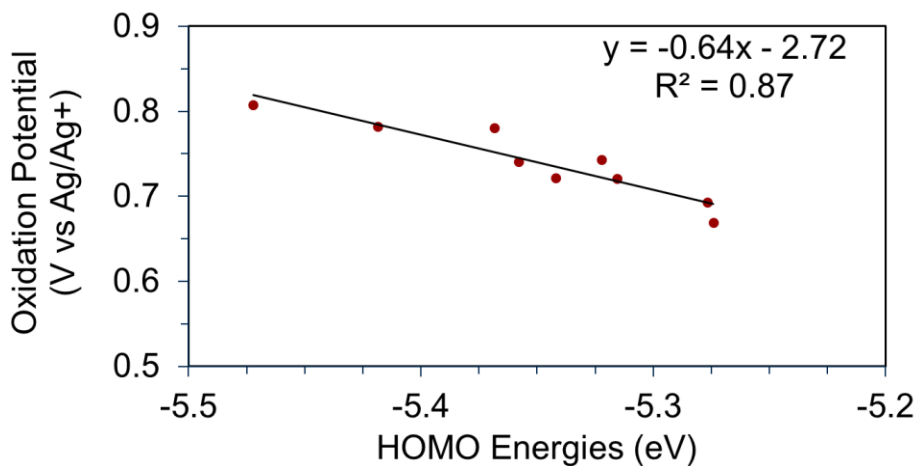
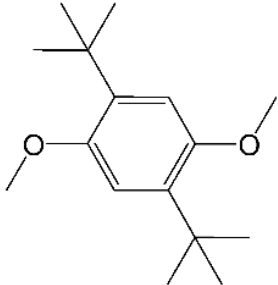
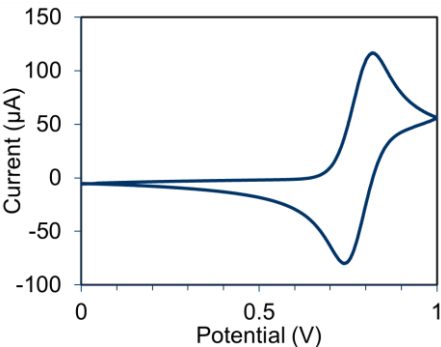
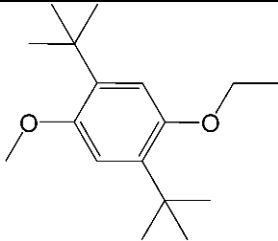
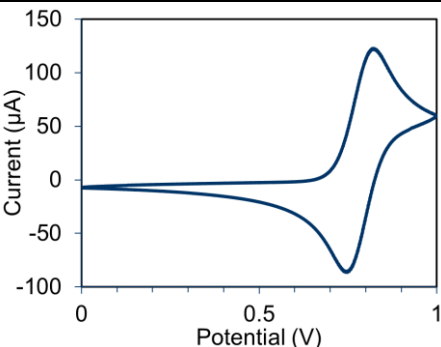
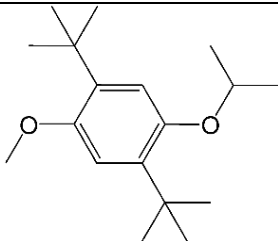
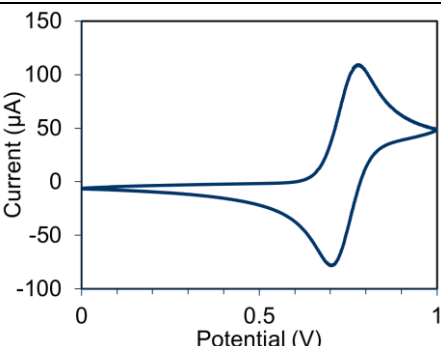
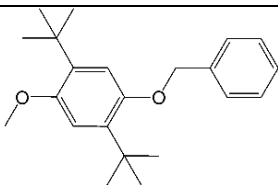
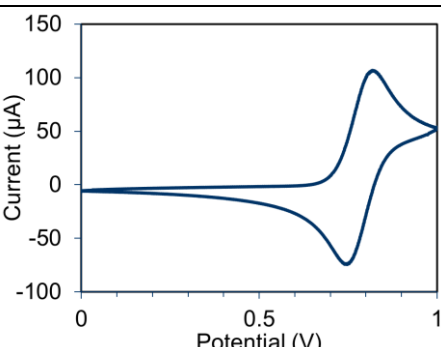
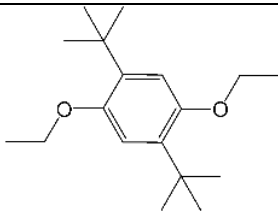
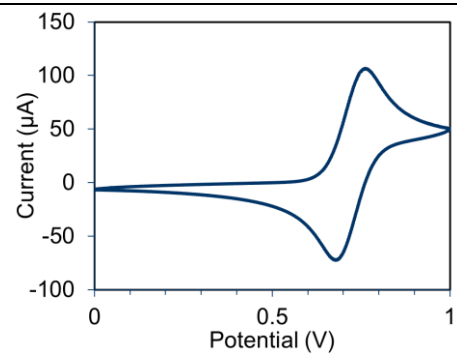
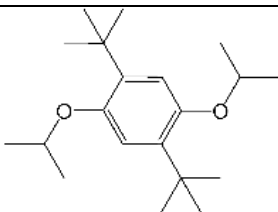
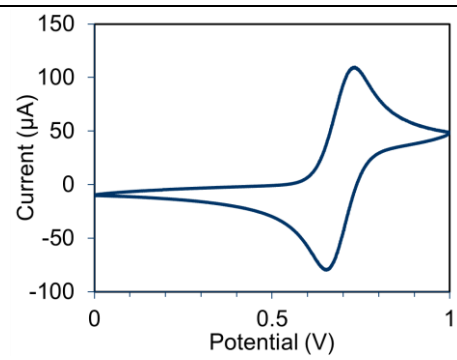
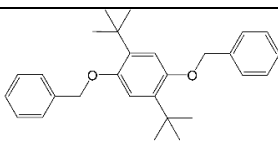
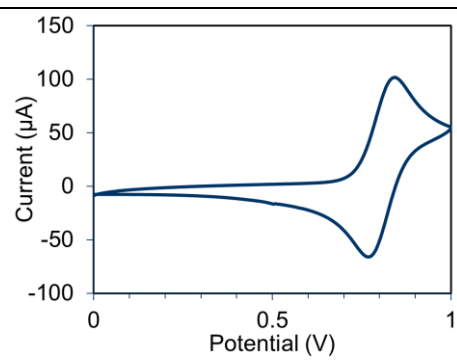
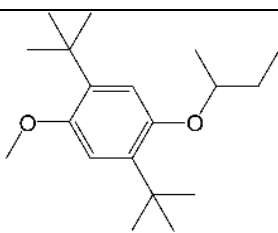
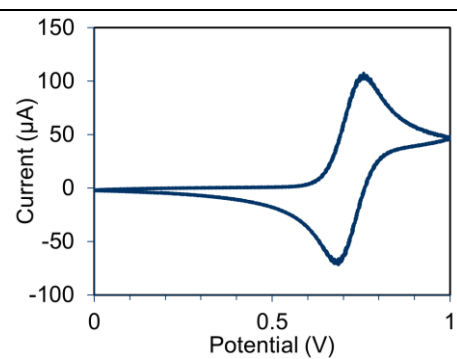
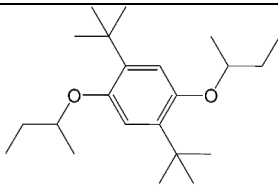
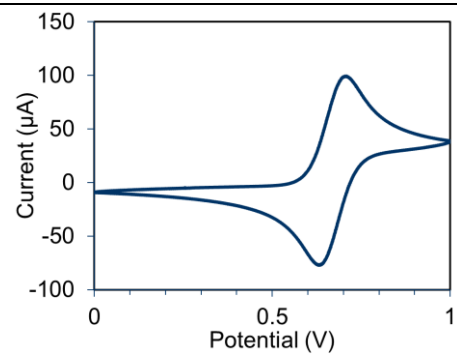


Figure 2.6 Correlation between oxidation potentials and HOMO energies of the dialkoxyarene catholytes.

Table 2.1 Names, structures, oxidation potentials (vs Ag/Ag⁺), peak height ratios, and CV scans of the nine dialkoxyarene catholytes.

Molecule	Structure	E_{ox}	$\frac{i_{p,a}}{i_{p,c}}$	CV
Q1		0.781	0.89	
Q2		0.741	0.95	
Q3		0.743	0.94	
Q5		0.782	0.91	

Molecule	Structure	E_{ox}°	$\frac{i_{p,a}}{i_{p,c}}$	CV
Q6		0.722	0.92	
Q7		0.693	0.94	
Q9		0.808	0.87	
Q10		0.721	0.93	

Molecule	Structure	E_{ox}°	$\frac{i_{p,a}}{i_{p,c}}$	CV
Q11		0.669	0.94	

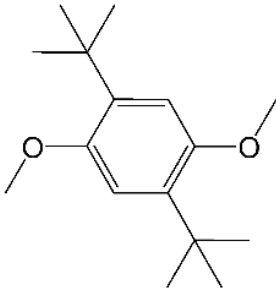
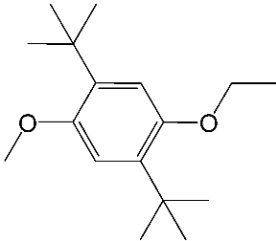
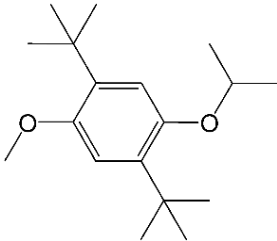
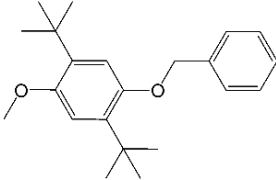
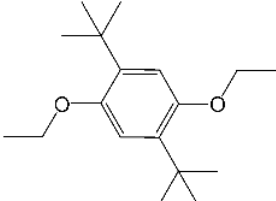
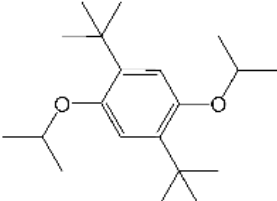
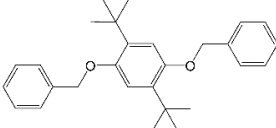
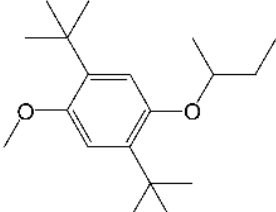
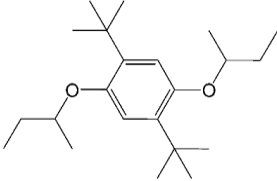
2.3.2 Cyclability

Continuing with electrochemical characterization of the dialkoxyarene ROMS, BE experiments were performed to quantify their cyclability. All cycling experiments were performed at 5 mM with 500 mM of TBAPF₆ in 10 mL of MeCN to 50% SOC at a rate of 1 C (corresponding to a current which charges 100% SOC in one hour) with voltage cutoffs of ± 200 mV. The dialkoxyarene molecules, their average (in the case of experiments with replicate data) N_{80} and CE are reported in Table 2.2. Except for Q5 and Q9, all molecules had reasonable performance compared to previously reported non-aqueous active materials, with an N_{80} of at least 50.

Additional trends are explained with the BE and CV data. The expected positive correlation between N_{80} and CE is present, as better cycling molecules are expected to discharge more efficiently. However, the N_{80} greatly exceeds the amount of material unrecovered by CE , implying that a significant portion of un-discharged active material decays back to the parent molecule. The expectation that lower redox potentials can signal greater stability⁴⁸ also extends to N_{80} for this dialkoxyarene set. Q11 was clearly the best cycling of the molecules, followed by Q7, which have the lowest oxidation potentials of the group. Additionally, they are the most sterically hindered molecules of the set. This steric hinderance likely has an additional dependence on symmetry; Q10 and Q3, despite having the same functionalization on one ligand, perform significantly worse than Q11 and Q7 respectively. Replicate data was recorded for Q2, Q7, and Q11, and all results were confirmed.

Investigating the poor performance of Q5 and Q9, both were functionalized with bulky benzyl groups, which appeared to have a significant effect on their N_{80} . Further investigation with DFT revealed that these benzyl groups rotated ninety degrees when Q5 and Q9 were oxidized, this significant structural change is the likely cause of their rapid decay, as less-significant changes to structure during redox has led to poor cycling performance of MCCs.⁷⁰

Table 2.2 Names, structures, cycle lives, and coulombic efficiencies from BE experiments of the dialkoxyarene catholytes.

Molecule Structure	Q1 	Q2 	Q3 
\bar{N}_{80} \overline{CE}	68 92.4%	60 89.7%	50 92.5%
Molecule Structure	Q5 	Q6 	Q7 
\bar{N}_{80} \overline{CE}	29 86.7%	53 91.2%	73 91.9%
Molecule Structure	Q9 	Q10 	Q11 
\bar{N}_{80} \overline{CE}	18 84.9%	55 92.0%	127 96.3%

2.3.3 Decay Mechanisms

This section is adapted with permission from B. Silcox, J. Zhang, I. Shkrob, L. Thompson, L. Zhang; *Journal of Physical Chemistry C* (2019). Copyright 2019 American Chemical Society

Plots of capacity vs cycle number are the most common way to report the behavior of a cycling experiment and can be used in conjunction with post-cycling CV to infer possible decay mechanisms for the active material of interest. This is particularly insightful for the dialkoxyarene series in the TBAPF₆/MeCN electrolyte. Each molecule's capacity decayed in an identical manner except for Q11, shown in Figure 2.7.

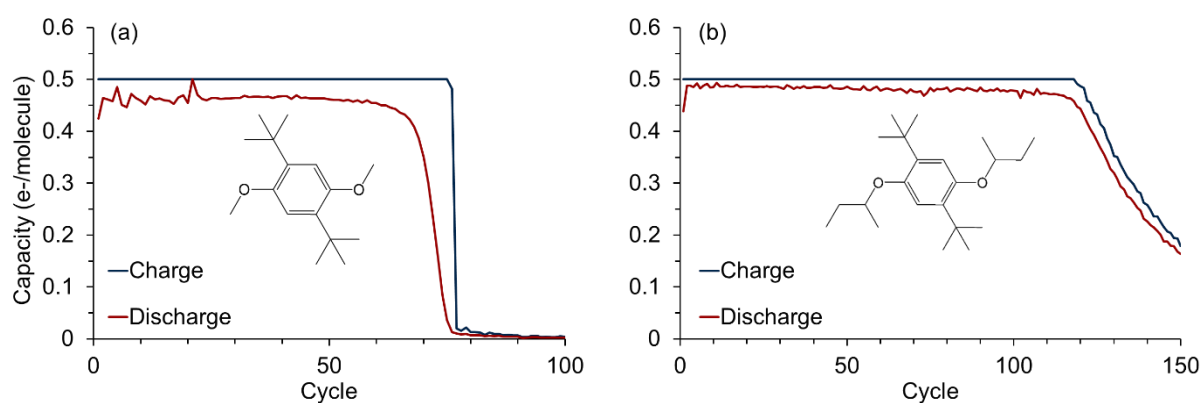
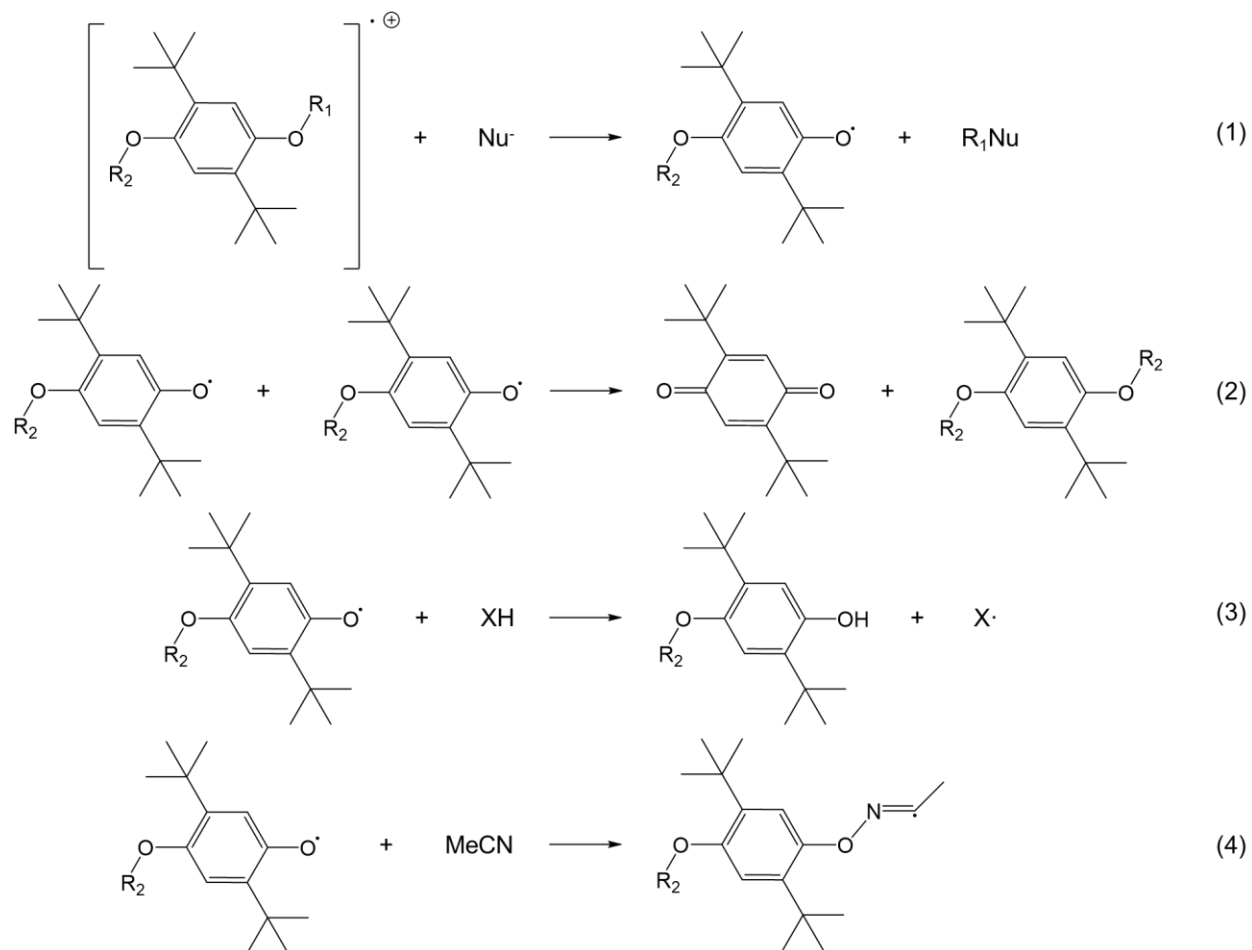


Figure 2.7 Capacity vs cycle life plots for (a) Q1 and (b) Q11. Structures shown inset. The decay behavior of Q1 is an abrupt decrease, while Q11 decays with a first order rate.

In Q11, this decay reaction has first-order kinetics with a familiar first-order shape. For all other molecules, this reaction is self-catalyzed, eventually reaching a critical rate where the charged species decays before it can be discharged, causing an abrupt loss of capacity. All post-cycling CVs for these materials indicated that the active material was completely depleted, confirming their decay into an electrochemically inactive species.

To investigate this decay mechanism further, product quantification with GC-MS and H-NMR was performed at ANL. The likely reaction pathway back to the parent molecules is via deprotonation of the radical cation from the alkoxy group of the molecule that is followed by H atom abstraction from the solvent by the C-centered radical. This particular pathway is suggested by H/D substitution observed in the ROMs electrolyzed in deuterated MeCN; however, it is not possible to fully exclude the protic impurity as a possible reagent for a fraction of charged ROMs.

The primary competing reaction is O-dealkylation that is initiated when an anion, the solvent, or a nucleophile solvent impurity attacks the ROM (ArOR), releasing an aroxyl radical (ArO•) and a free or bound carbocation, R⁺. Two such aroxyl radicals can disproportionate to yield the corresponding quinone (that can also form by secondary oxidation of the phenols); alternatively, the aroxyl radicals abstract hydrogen yielding phenols (ArOH) or react with acetonitrile to yield ArON=• CMe radicals that undergo internal cyclization through the elimination of tert-butyl from the ortho-position in the aromatic ring. These reactions are shown in Scheme 2.3.



Scheme 2.3 (1) Dialkoxyarene dealkylation and subsequent (2) disproportionation, (3) abstraction, and (4) solvent reactions to form products.

The presence of these three products was established using GC-MS, and their chemical structure was confirmed by chromatographic fractioning and ¹H NMR spectroscopy. These

aroxyl-related products can be observed alone or in combination, depending on the ROM structure and experimental conditions. The carbocation elimination is particularly efficient when a stable carbocation (such as the benzyl) is generated; hence, the radical cations of such ROMs are very vulnerable to O-dealkylation. The stable carbocations (R⁺) reversibly add to the acetonitrile, yielding RN=C⁺ Me cations that subsequently undergo the Ritter reaction, yielding acetamides (RNH₂(O)Me), which are detected using GC-MS. According to our product analyses, O-dealkylation is the main reaction for such ROMs.

This O-dealkylation reaction rate is dependent on molecular structure, although no relation has been identified. The decay behavior of Q11 suggests that its steric hinderance removes the chain-reaction behavior of the dealkylation and can be a design factor for future, more cyclable dialkoxyarenes.

2.3.4 Cyclability Comparisons with ANL

Cyclability characterization of the dialkoxyarene molecules occurred in tandem at ANL under different experimental conditions: 20 mM of active material in 500 mM LiTFSi/MeCN, cycled to 50% SOC at 3 C rate and voltage cutoffs from 0 to 1.6 V vs Ag/Ag⁺. Q9 was an exception due to solubility and was cycled at UM at a 5 mM concentration with all other conditions identical to ANL. The results of this investigation are plotted in Figure 2.8.

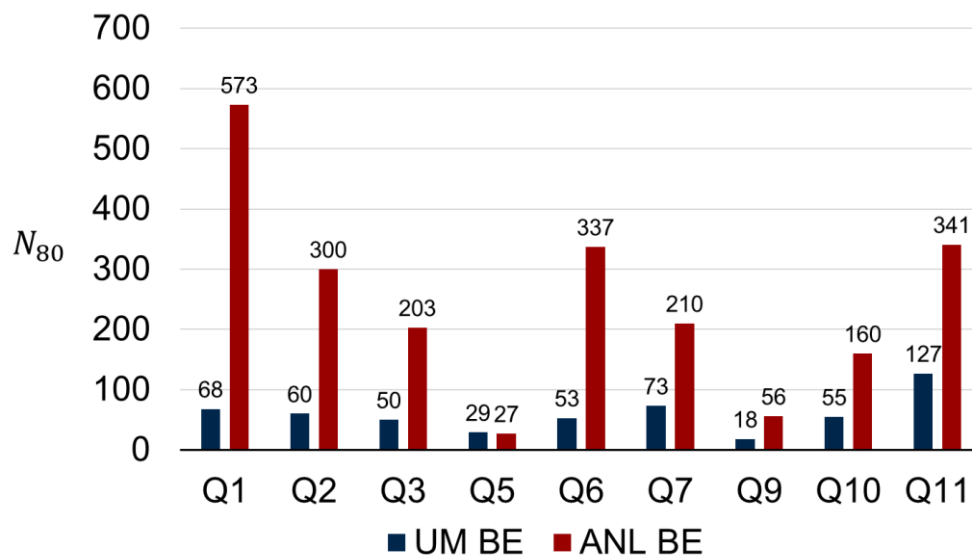


Figure 2.8 Comparison between N_{80} of the dialkoxyarene catholytes at UM and ANL. Q1 shows the largest increase in N_{80} , while Q5 shows no change in N_{80} despite cycling at three times the rate.

There is no consistent trend between the two experimental conditions, with most molecules outperforming expectations at the ANL conditions. As a general rule, if a molecule underwent the same behavior during cycling at ANL and UM, we expect its N_{80} to be a function of the cycle rate: the N_{80} of the active materials should have been increased by a factor of 3 at ANL compared to UM. However, this is only the case for Q7, Q9, Q10, and Q11. It is likely that the electrolyte environment is responsible for the drastically increased N_{80} seen from Q1, Q2, Q3, and Q6. Lithium ions are known to coordinate with acetonitrile, changing the overall solvation environment and the cycling behavior of specific molecules.^{38,71} Molecules with sufficient steric hinderance (Q7, Q9, Q10, and Q11) avoid interaction with the new Li-MeCN coordination structures. Steric hinderance may also provide insight into the N_{80} increases seen from Q1, Q2, Q3, and Q6. Their unexpected increase in N_{80} also correlates with their steric hinderance, Q1 is the least bulky molecule and has the greatest overperformance of the four, while Q3 is the bulkiest and has its magnitude of increase is the least of the four. While the exact interaction of Li^+ in the electrolyte is unknown, its impact on the performance of the dialkoxyarenes can be explained by structural characteristics.

Q5 is the outlier molecule, recording the same N_{80} at both sets of conditions. This specific result suggests that Q5's N_{80} is limited by the number of charge/discharge cycles it undergoes, further supporting the hypothesis that the rotation of the benzyl group during oxidation places excess steric strain on the structure.

2.4 Conclusions

In this Chapter, nine new dialkoxyarene catholyte molecules were systematically characterized to identify trends in their electrochemical properties. Analysis of the nine structures and their performance revealed many significant relationships. CV results demonstrated a negative relationship between electrochemical reversibility and redox potential. Further addition of BE data revealed a relationship between steric hinderance, cyclability, and redox potential. Q11 was by far the best cycling molecule of the data set, likely due to its bulky sec-Butyl substitution compared to the rest of the molecules. With ANL, the decay mechanism of the dialkoxyarene catholytes was hypothesized as O-dealkylation, which proceeds in a runaway manner. Lastly, comparisons between cyclability were made at ANL and UM, and discovered the significant effect experimental conditions and electrolyte choice have on performance, which are explored in Chapter 3. Overall, this work confirms the benefit of steric hinderance on ROM cyclability, which can be used as a starting point for molecular design of future active materials.

2.5 Acknowledgments

I would like thank Dr. Jingjing Zhang from Dr. Lu Zhang's group for his collaborative efforts on this project. He was responsible for all the active material synthesis in this chapter and electrochemical characterization at ANL.

Chapter 3

Factors Affecting Bulk Electrolysis Cycling Performance

3.1 Background and Approach

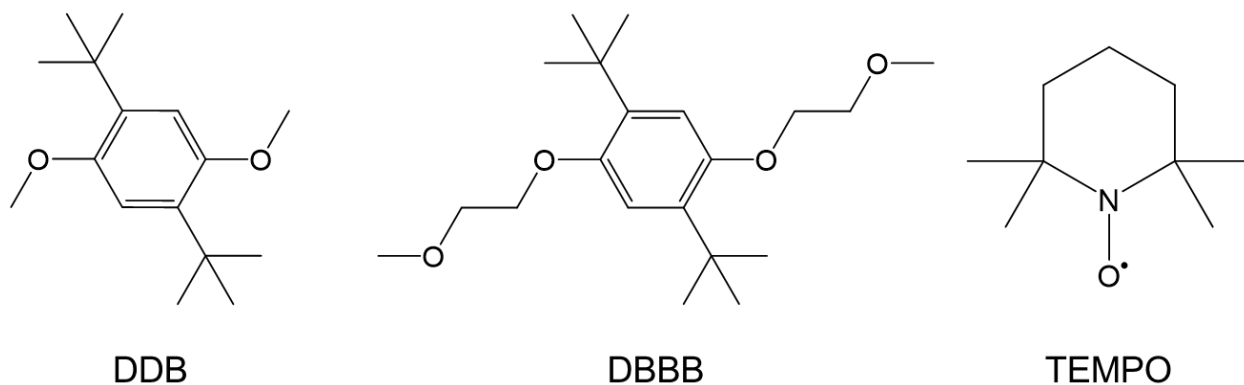
Active materials for non-aqueous redox flow batteries (NaRFBs) need to exhibit electrochemical reversibility, solubility, stability, and cyclability. Of these criteria, design for reversibility, solubility, and stability are relatively well understood.^{45,59,72} Cyclability and their associated experiments introduce additional complexity into quantifying and understanding active material behavior in the form of electrode-active material interactions, crossover, and extended time under load, among others. To better understand and design for cyclability, it is necessary to understand the additional complexities introduced by cycling experiments.

In Chapter 2, I discussed the dialkoxyarene redox active organic molecule (ROM) family and their development into catholytes. The molecules characterized by cyclic voltammetry (CV) and bulk electrolysis (BE) helped identify the effect of steric hinderance on oxidation potential, reversibility, and cycle life (N_{80}). However, N_{80} was as greatly influenced by the active materials themselves as the experimental conditions. For Li^+ supporting salts, steric hinderance actually limited the possible N_{80} of the dialkoxyarenes, providing even more complexity in the interpretation and analysis of cyclability experiments. Of the experimental conditions used, three were identified as key factors: active material concentration, cycle rate, and supporting salt choice.

The effect of supporting salt choice has been briefly reported for ROMs.^{41,73,74} In particular, Li^+ coordination to active materials has been intentionally used to increase cyclability of a tetramethylnaphthalene ROM.⁴¹ Lithium coordination to the Lewis basic methoxy groups of the molecule allowed the complex to cycle reversibly compared to an alkylammonium cation.

Additionally, individual active materials may be incompatible with specific supporting salts and solvents, an effect that is unknown until cycling.⁷³ Active material concentration and cycle rate are even less studied and are often chosen for convenience. While these effects are significant and deserve investigation, research efforts have mostly focused on designing and improving active materials.^{48,59,75}

In this chapter, I propose an experimental design to investigate the effect of active material concentration, cycle rate, and supporting salt choice on the three catholytes in Scheme 3.1, 1,4-Di-*tert*-butyl-2,5-dimethoxybenzene (DDB, Q1), 1,4-Di-*tert*-butyl-2,5-bis (2-methoxyethoxy)benzene (DBBB, C1), and (2,2,6,6-Tetramethylpiperidin-1-yl)oxyl (TEMPO).



Scheme 3.1 Structures of DDB, DBBB, and TEMPO.

A set of 66 BE experiments are used to fully explore the design space, and the effect of each experimental condition on N_{80} is reported. Most importantly, guidelines for thorough electrochemical characterization and electrolyte choice are discussed. This work establishes the importance of proper BE characterization and the impact on reported performance.

3.2 Experimental

3.2.1 Materials

3.2.1.1 Active Materials

The three active materials used in this Chapter were chosen for their availability and demonstrated cyclability in lithium-ion (Li-ion) and NaRFB applications.^{43,44,46,76} Adding a molecule outside the dialkoxyarene family provides a control for effects specific to the

dialkoxyarene family. TEMPO was chosen for its extreme solubility (5.2 M) in carbonate electrolytes and similar performance.⁴⁷

TEMPO (Sigma Aldrich, 98%) was used as received. Two batches of DDB were used, one from Argonne National Laboratory (ANL) and one from AAblocks (98%). The two samples were confirmed electrochemically identical by CV and BE. DBBB was synthesized at ANL, its synthesis procedure is included here from ref. 46.

2,5-di-*tert*-butylhydroquinone (9 mM) was dissolved in anhydrous tetrahydrofuran (THF) (20 mL). Sodium hydroxide (27 mM) and 2-methoxyethoxymethyl chloride or 2-chloroethylmethyl ether (18 mM) was added to the solution. The reaction was stirred at room temperature overnight. After removal of the THF, the residue was partitioned between dichloromethane (DCM) and NaHCO₃ (0.1 M). The organic portion was separated and dried over Na₂SO₄ before the solvent was removed under vacuum. The crude product was chromatographed (silica, hexanes/DCM from 5:1 to 1:1) isolate oligo(ethylene glycol) functionalized compounds, which were further purified by crystallization from saturated DCM solution under low temperature.

3.2.1.2 Supporting Salts

Six supporting salts were chosen for this work based to provide a range of cations and anions: tetrabutylammonium tetrafluoroborate (TBABF₄), tetrabutylammonium hexafluorophosphate (TBAPF₆), tetraethylammonium tetrafluoroborate (TEABF₄), lithium tetrafluoroborate (LiBF₄), lithium hexafluorophosphate (LiPF₆), and lithium bis(trifluoromethanesulfonyl)amide (LiTFSi). These six were selected to provide a spectrum of anions and cations, maintaining at least one common ion for each molecule in the series. Of commonly available and used NaRFB support salts, only tetraethylammonium bis(trifluoromethanesulfonyl)amide (TEATFSi) was not used due to time constraints. All supporting salts were purchased from Sigma Aldrich at purities > 99 % for the alkylammonium salts and > 99.9% for the lithium salts. Alkylammonium salts were dried under vacuum for 24 hours at 140 °C before use.

3.2.2 Electrochemical Methods

For this work, all materials storage, solution preparation, and electrochemical characterization were performed in an argon-filled glove box ($O_2 < 0.3$ ppm, $H_2O < 0.5$ ppm). All BE and CV experiments were performed in a fritted glass H-cell with 10 mL of electrolyte split between the working and counter chambers. A reticulated vitreous carbon (RVC) (Duocell) counter electrode and a Ag/Ag⁺ quasi-reference electrode (BASi) were used for all experiments. Acetonitrile (MeCN) (Acros Organics) was used as the solvent for all solutions and contained a supporting salt concentration of 500 mM. The reference electrode was a fritted chamber containing 10 mM of a corresponding silver salt: silver tetrafluoroborate (AgBF₄) for BF₄⁻ salts, silver nitrate (AgNO₃) for PF₆⁻ salts, and silver bis(trifluoromethanesulfonyl)amide AgTFSi for LiTFSi and a silver wire. A BioLogic VSP potentiostat recorded all data. A total of 66 BE experiments were run for this chapter, 3 catholytes, 2 active material concentrations, 2 cycle rates, and 6 supporting salts. 6 cells, 20 mM DDB in alkylammonium salts, were not cycled due to solubility limits.

3.2.2.1 Cyclic Voltammetry

CVs were measured in-situ before and after BE experiments with a 3.0 mm diameter glassy carbon (GC) working electrode (BASi). CV scans were taken before cycling experiments with 500 mM supporting salt in 10 mL MeCN. Scans were recorded from 0 to 1 V vs Ag/Ag⁺ at a scan rate of 100 mV/s and all scans displayed are of the fourth cycle out of five.

3.2.2.2 Bulk Electrolysis

BE were performed with an RVC working electrode. Three sets of cutoffs were used: a potential cutoff set around the redox event, a state of charge (SOC) cutoff to 50% theoretical SOC, and a time cutoff if any of the previous two cutoffs failed. With the high N_{80} seen in some experiments, it is valuable to note that BE measures the lower bound of cyclability, as modes of failure (electrode failure, crossover, and others) at $N_{80} > 400$ can often be related to failure of the cell components themselves. Additionally, cells with long enough N_{80} will inevitably fail due to MeCN evaporating out of the working and counter chambers to the point where electrodes

are unable to contact the electrolyte. To allow for a non-time dependent measurement of N_{80} , these cells were periodically refilled with MeCN. Due to the excess of MeCN compared to the active material, this should not have an effect on performance or other cell failure modes.

3.2.2.3 Active Material Concentration

Two active material concentrations were chosen for comparison, 5 mM and 20 mM. These concentrations were selected from the concentrations used in Chapter 2. Solubility is the limiting factor for reaching higher active material concentrations, especially with the limited solubility of DDB (8 mM in carbonate).⁴³ Despite valiant efforts, DDB was still insoluble at 20 mM with the alkylammonium salts, reducing the total number of experiments.

3.2.2.4 Cycle Rate

Two cycle rates were chosen for comparison, 1 C and 3 C, also selected from the cycle rates tested in Chapter 2. For BE experiments, cycle rate is often not a limiting factor due to high electrode surface area, rapid stirring of each chamber, and lack of concern about overpotential.

3.2.3 Computational Methods

3.2.3.1 Density Functional Theory

All density functional theory (DFT) used in this Chapter was performed on Gaussian09⁶⁹ with the Becke, three-parameter, Lee-Yang Parr hybrid functional and 6-31G(d) basis set.^{66,67} Computing resources were provided by UM Advanced Research Computing.

3.2.3.2 Molecular Dynamics

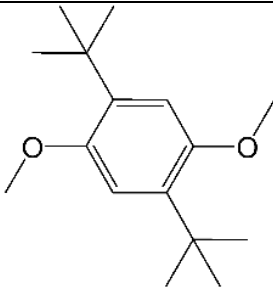
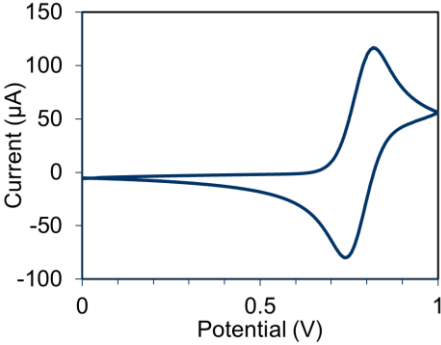
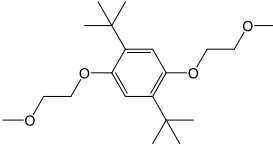
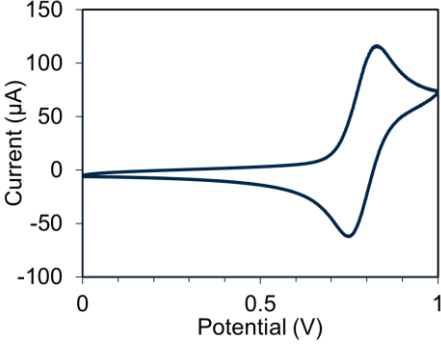
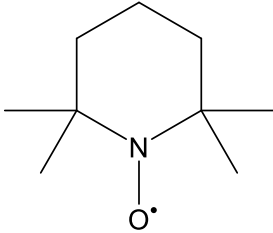
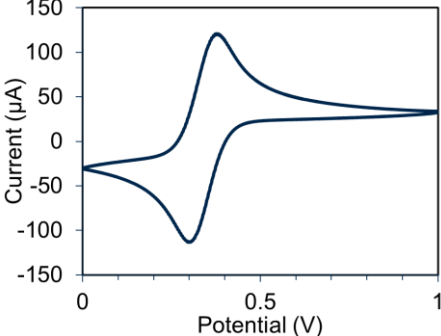
Molecular dynamics (MD) simulations were performed at Argonne National Laboratory (ANL) for TEMPO solvation with a ratio of TEMPO:Supporting Salt:MeCN of 1:50:800 in the Opls-aa force field.

3.3. Results and Discussion

3.3.1 Oxidation Potentials and Electrochemical Reversibility

While all three active materials investigated are known to be stable and cyclable, CV scans, peak height ratios, and experimentally determined oxidation potentials (V vs Ag/Ag⁺) from the 5 mM active material concentration, 1 C rate, TBAPF₆ experiments (5/1/TBAPF₆) are presented in Table 3.1.

Table 3.1 Names, structures, oxidation potentials (vs Ag/Ag⁺), peak height ratios, and CV scans of the three selected catholytes.

Molecule	Structure	E_{ox}	$\frac{i_{p,a}}{i_{p,c}}$	CV
DDB		0.781	0.89	
DBBB		0.791	0.83	
TEMPO		0.339	0.99	

Of particular note is the greater oxidation potential of DBBB compared to DDB despite being more sterically hindered. DBBB also displays a poor peak height ratio that is confirmed by CVs in the other supporting salts. Despite this, the cycling behavior of DBBB does not seem to be affected, one of the limitations of using electrochemical reversibility as a proxy for cycling characterization.

3.3.2 Cycling Summary

The N_{80} and coulombic efficiency (CE) for all BE experiments is presented in Tables 3.2 - 3.4, arranged by active material, concentration, cycle rate, and supporting salt in sequence.

Table 3.2 Name, structure, active material concentration, cycle rate, supporting salt, cycle life, and coulombic efficiency for DDB. The alkylammonium supporting salts were not cycled at 20 mM active material concentration due to solubility limitations of DDB. Cells that terminated prematurely are marked with an asterisk.

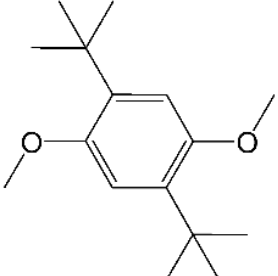
Molecule	Structure	Active Material Concentration	Cycle Rate	Supporting Salt	N_{80}	CE		
DDB		5 mM	1 C	TBABF ₄	16	76.0%		
				TBAPF ₆	68	92.4%		
				TEABF ₄	21	78.1%		
				LiBF ₄	48	91.8%		
				LiPF ₆	498*	98.6%		
				LiTFSi	623*	95.3%		
			3 C	TBABF ₄	19	86.3%		
				TBAPF ₆	168	98.1%		
				TEABF ₄	35	91.9%		
				LiBF ₄	345	96.8%		
				LiPF ₆	2868*	95.9%		
				LiTFSi	901*	99.7%		
				20 mM	1 C	LiBF ₄	620*	93.5%
						LiPF ₆	1073	98.9%
						LiTFSi	447	98.9%
3 C	1 C	LiBF ₄	86	94.8%				
		LiPF ₆	210	98.4%				
		LiTFSi	172	96.9%				

Table 3.3 Name, structure, active material concentration, cycle rate, supporting salt, cycle life, and coulombic efficiency for DBBB. Cells that terminated prematurely are marked with an asterisk.

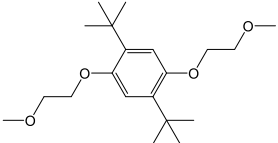
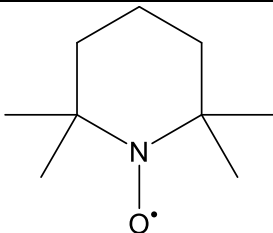
Molecule	Structure	Active Material Concentration	Cycle Rate	Supporting Salt	N_{80}	CE
DBBB		5 mM	1 C	TBABF ₄	21	82.5%
				TBAPF ₆	63	89.6%
				TEABF ₄	26	84.5%
				LiBF ₄	70	93.1%
				LiPF ₆	941*	98.1%
				LiTFSi	883*	93.1%
		3 C	TBABF ₄	48	91.9%	
			TBAPF ₆	165	96.8%	
			TEABF ₄	32	88.5%	
			LiBF ₄	756*	98.2%	
			LiPF ₆	2696*	99.6%	
			LiTFSi	582	96.4%	
		20 mM	1 C	TBABF ₄	26	71.7%
				TBAPF ₆	33	87.2%
				TEABF ₄	176	96.7%
				LiBF ₄	648*	95.9%
				LiPF ₆	548	99.3%
				LiTFSi	439	96.0%
3 C	TBABF ₄		137	97.8%		
	TBAPF ₆		131	98.2%		
	TEABF ₄		163	97.4%		
	LiBF ₄		72	95.7%		
	LiPF ₆		461	95.7%		
	LiTFSi		242	98.4%		

Table 3.4 Name, structure, active material concentration, cycle rate, supporting salt, cycle life, and coulombic efficiency for TEMPO. No TEMPO cells terminated prematurely.

Molecule	Structure	Active Material Concentration	Cycle Rate	Supporting Salt	N_{80}	CE
TEMPO		5 mM	1 C	TBABF ₄	129	98.0%
				TBAPF ₆	132	98.0%
				TEABF ₄	131	98.8%
				LiBF ₄	182	99.9%
				LiPF ₆	68	99.5%
				LiTFSi	323	98.5%
		20 mM	3 C	TBABF ₄	89	97.8%
				TBAPF ₆	132	99.0%
				TEABF ₄	254	99.1%
				LiBF ₄	155	100.0%
				LiPF ₆	141	99.7%
				LiTFSi	366	99.2%
		20 mM	1 C	TBABF ₄	118	98.1%
				TBAPF ₆	149	98.9%
				TEABF ₄	102	97.3%
				LiBF ₄	142	99.9%
				LiPF ₆	67	98.8%
				LiTFSi	328	98.9%
20 mM	3 C	TBABF ₄	93	98.4%		
		TBAPF ₆	118	98.7%		
		TEABF ₄	156	99.0%		
		LiBF ₄	105	99.5%		
		LiPF ₆	178	100.0%		
		LiTFSi	193	99.5%		

Three primary decay behaviors were seen among the cycling experiments, shown in Figure 3.1.

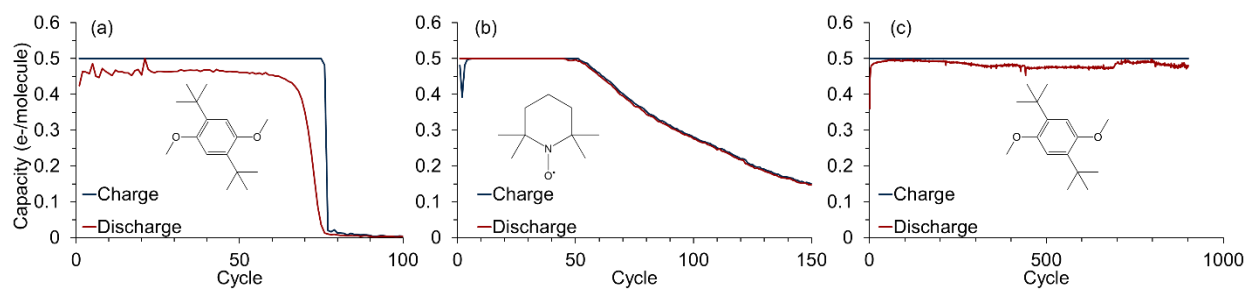


Figure 3.1 Capacity vs cycle life plots for (a) DDB 5/1/TBAPF₆, (b) TEMPO 5/1/LiPF₆, and (c) DDB 5/3/LiTFSi. Structures shown inset. The decay behavior of (a) is an abrupt decrease, (b) is a first order decay, and (c) terminates without capacity fade.

The capacity fade behaviors shown in Figure (a) and (b) were discussed in Chapter 2. The abrupt fade is due to self-catalyzed behavior of the active material decay, while the first order decay is expected without this self-catalyzation. Figure (c) shows a third decay, where cycling is abruptly terminated. This behavior was only seen in cells with significantly high N_{80} (> 400 cycles). This occurs when the cell fails due to an external factor. Experimental observation of these cells hypothesized that electrode failure accounted for all these cases, either through disconnection of the RVC from the electrode assembly or coating of the counter electrode and the subsequent cycling failure. Neither of these results is particularly damning for the active material itself. The laboratory assembled RVC electrodes are not expected to be perfect, especially in the harsh BE environment. Similarly, the coating and subsequent failure of the counter electrode is unique to the H-cell and would not be present in a full flow cell, where the complimentary chamber would be cycling around a separate active material. Results where this termination of cycling occurs are therefore a lower bound on the N_{80} at these experimental conditions.

Similar to the dialkoxyarene active materials discussed in Chapter 2, N_{80} greatly exceeds the amount of material unrecovered by CE, implying that a significant portion of un-discharged active material decays back to the parent molecule for all experiments.

3.3.3 DDB Summary

As predicted from the results in Chapter 2, DDB sees drastic N_{80} and CE improvements when cycled in Li⁺ salts. Of the alkylammonium salts, N_{80} is largest in TBAPF₆. Conclusions about

increasing active material concentration are hard to draw, as none of the 20 mM alkylammonium salt experiments could be performed due to solubility limitations and many of the Li^+ salt experiments failed due to cell termination. Cycle rate had mixed effects, only one cell pair, 5/1/TBAPF₆ and 5/3/TBAPF₆, showed linear scaling of N_{80} with cycle rate, the expected behavior. The cycle rate variations between 20/1/ Li^+ and 20/3/ Li^+ show extreme N_{80} decreases that are not expected from previous results and are unaccounted for in the experimental design. These results are likely due to increased cell resistances. DDB shows an incompatibility with BF_4^- anions, which are even able to reduce the N_{80} of the 5/1/ LiBF_4 experiment to alkylammonium-similar. This behavior will be discussed in Section 3.3.8.1.

3.3.4 DBBB Summary

Similar to DDB, DBBB sees drastic N_{80} and CE improvements when cycled in Li^+ salts and are incompatibility with BF_4^- anions. With the exceptions of BF_4^- anionic salts, increasing active material concentration causes a slight decrease in N_{80} and mixed effects on CE that appear to depend on the supporting salt. The relatively poor performance of DBBB 20/3/ Li^+ compared to other experiments conditions is also present.

3.3.5 Similarities in DDB and DBBB Performance

DDB and DBBB show similar performance and trends between at identical experimental conditions (incompatibility with BF_4^- , improved performance in Li^+ , similar performance at 5/3/ LiPF_6 , etc.). As they have similar structure, this is unsurprising. This result is encouraging because it helps support the existence of a structure-function relationship in the dialkoxyarene family. For the remainder of this chapter, DDB and DBBB will be discussed together.

3.3.6 TEMPO Summary

The TEMPO cycling experiments provide a particularly useful comparison to the dialkoxyarene active materials, as TEMPO exhibits a smaller degree of Li^+ stabilization on N_{80} and none of the TEMPO cells terminated due to cell failure. Additionally, TEMPO does not exhibit the same BF_4^- incompatibility behavior as DDB and DBBB although there is likely some effect present.

TEMPO however, does exhibit an incompatibility with LiPF_6 , which will also be discussed in Section 3.3.8.3. At 5 mM active material and 1 C rate, TEMPO exhibits remarkable consistency in N_{80} and CE between all three alkylammonium support salts. In addition, these results confirm the cycle life reported for TEMPO as Li-ion overcharge, shown in Figure 3.2.

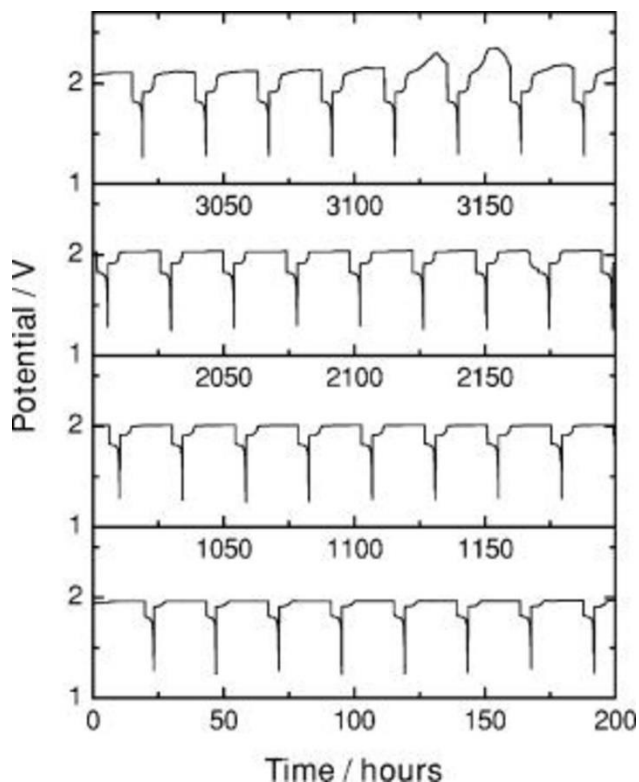


Figure 3.2 Cycling of a $\text{Li}_{4/3}\text{Ti}_{5/3}\text{O}_4/\text{LiFePO}_4$ coin cell with 0.3 M TEMPO in 0.5 M LiBOB electrolyte. TEMPO was used as an overcharge protector, cycling after the primary redox event. With 25-hour cycles, TEMPO remained cyclable until 124 cycles at around 3100 hours.⁴⁴

As a quasi-baseline for N_{80} , TEMPO exhibits some performance benefits in Li^+ salts, as expected for a molecule without significant steric hinderance. Similar to DDB and DBBB, performance was noticeably harmed in the 20 mM active material 3 C cycle rate experiments.

Of the three active materials cycled, TEMPO is unique as a stable organic radical. In addition to a decay of the positively charged ion, TEMPO itself has a half-life and observed first order decay into electrochemically non-active materials by disproportionation. In the non-interactive alkylammonium salts, this is the most likely cause of the consistent capacity fade.

3.3.7 Exceptional Dialkoxyarene Performance

Previously reported ROM N_{80} has been limited, reaching 100 cycles in BE is an accomplishment and seen as cyclable. These results show that it is possible to approach the long cell lifetimes (>4000 hours, 120 cycles) reported for DDB and DBBB in Li-ion overcharge^{43,46} in an H-cell. The DDB and DBBB 5/3/LiPF₆ cells and the DDB 20/1/LiPF₆ cell reached cell lifetimes around 1000 hours, with many more cycles at these experimental conditions than in Li-ion overcharge. These results show promise for these active materials, which are much closer to hitting the 5000 cycle N_{80} targets⁷⁷ needed for scale-up than previously reported.⁷⁶ Of these cells, the DDB 20/1/LiPF₆ cell shown in Figure 3.3 provides the most promising estimate of maximum N_{80} , as it failed due to capacity fade and not cell termination.

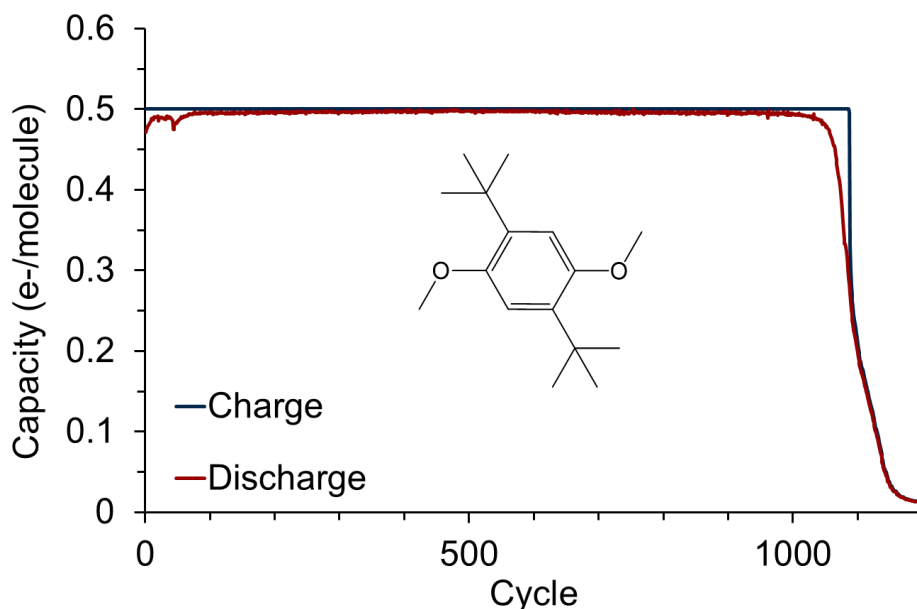


Figure 3.3 Capacity vs cycle life for the DDB 20/1/LiPF₆ cell. N_{80} was reached at 1073 cycles, the longest lifetime of any experiment. Experiments of this duration typically terminate due to cell component failure, making this result particularly valuable.

3.3.8 The Impact of Supporting Salt Choice on N_{80}

From Tables 3.2 – 3.4, the choice of supporting salt is observed to have just as great an impact on N_{80} as active material selection. The most dramatic change occurs with DDB and DBBB, which have two order of magnitude increases in N_{80} when moving from alkylammonium salts to LiPF₆. While the underlying mechanism behind these active material-supporting salt interactions

was not thoroughly investigated in this work, the wealth of experimental data reported allows us to draw conclusions. TBAPF₆ is the only salt not implicated in any electrolyte effect, and is recommended as a baseline for characterization of ROM active materials.

3.3.8.1 Incompatibility with BF₄⁻

The most noticeable trend from DDB and DBBB cycling is the extremely poor performance in the alkylammonium BF₄⁻ salts, with lesser performance in LiBF₄ than the other Li⁺ salts. This incompatibility is most likely due to an electrochemically active impurity present in the BF₄⁻ salts, which can be seen in the DDB 5/1/TBABF₄ CV in Figure 3.4.

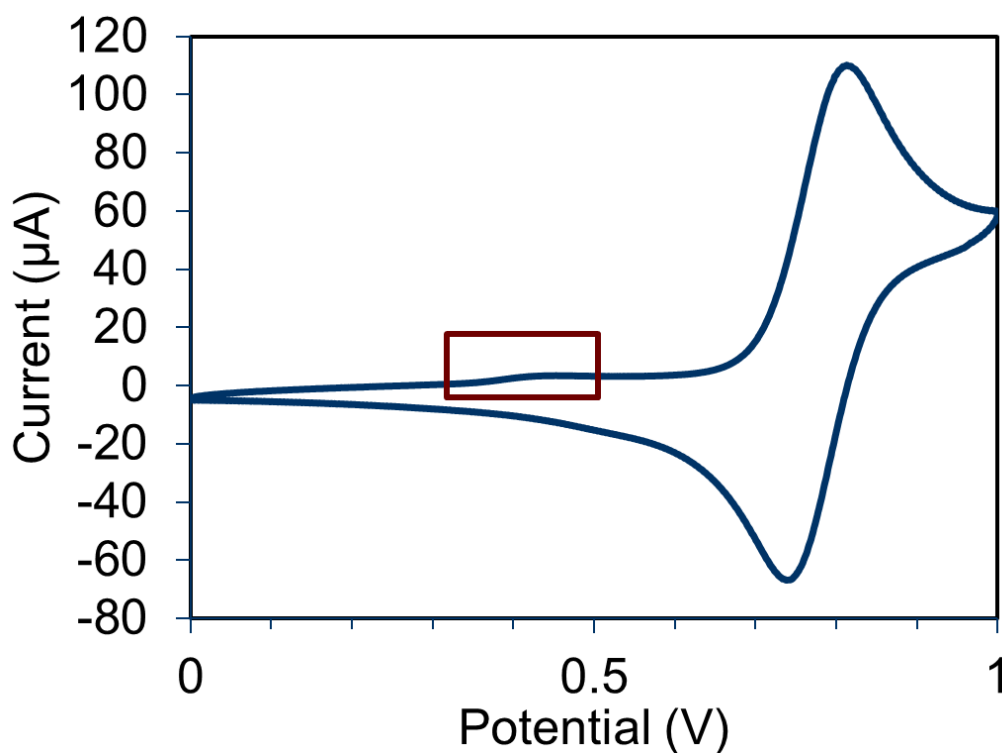


Figure 3.4 Pre-cycling CV for the DDB 5/1/TBABF₄ BE cell. The highlighted peak around 0.4 V shows the active impurity present in all BF₄ salts.

The highlighted section in the DDB 5/1/TBABF₄ CV shows a small peak around 0.4 V vs Ag/Ag⁺, this peak is also present in TEABF₄ and LiBF₄ CVs. TBABF₄ has the most prominent peak as the lowest purity of three salts. The presence of this peak in all three BF₄⁻ salts, its absence in the remaining three salts, and subsequent poor performance of the dialkoxyarenes in BF₄⁻, leads

to the hypothesis that this impurity interferes with dialkoxyarene cycling. At the greater active material concentration, N_{80} for DBBB in TBABF₄ and TEABF₄ reaches or improves on the TBAPF₆ N_{80} . The greater performance increase in TEABF₄ compared to TBABF₄ can be explained by the difference in purity.

This impurity has a reduced effect on TEMPO N_{80} due to TEMPO's redox potential, which is below that of the impurity, but its impact cannot be ruled out. TEMPO N_{80} trends with the different alkylammonium salts show no pattern across experimental conditions, suggesting this impurity may have an unknown but more complex effect than for the dialkoxyarenes. The presence of this impurity invokes the recommendation to avoid BF₄⁻ salts for electrochemical characterization without additional compatibility studies. For the remainder of this work, comparison of individual experiments becomes more difficult when three of the six supporting salts chosen contain the impurity.

One effect that cannot be explained with the previous hypothesis is the poor performance of DDB and DBBB in the 20/3/LiBF₄ cells. While all active materials performed poorly at the 20 mM active material and a 3 C cycle rate, DDB and DBBB in LiBF₄ were by far the worst.

3.3.8.2 Dialkoxyarene Behavior with Li⁺

DDB and DBBB both saw significant cyclability improvements in Li⁺ salts, with N_{80} increases up to two orders of magnitude. This stabilization suggests that either the changing electrolyte environment or Li⁺ coordination to the dialkoxyarenes are responsible. Of these two effects, Li⁺ coordination to the dialkoxyarenes is most likely. There are two possible explanations for improved N_{80} with Li⁺-coordination present. Coordination may lead to more stable charge/discharge reactions, like the mechanism in ref. 41. The second is based on the dialkoxyarene decay reactions in Scheme 2.3; the presence of Li⁺ coordination may serve a similar purpose as steric hinderance and inhibit the O-dealkylation reaction. Based on the N_{80} of DDB and DBBB with Li⁺ salts compared to the other dialkoxyarenes in Figure 2.8, this Li⁺ coordination is more impactful than steric hinderance for improving N_{80} . Possible Li⁺ coordination structures of DBBB were investigated by DFT, two possibilities are shown in Figure 3.5.

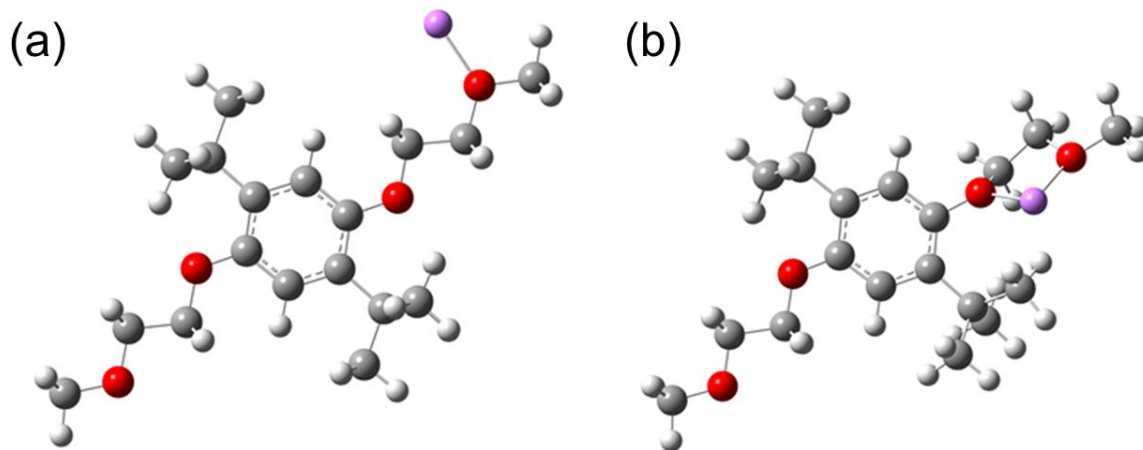


Figure 3.5 DFT optimized structures of DBBB coordinated to (a) one Li⁺ on a single O atom or (b) on two O atoms. Li is purple, O is red, C is grey, and H is white.

Of these two structures, the single O-Li⁺ coordination is more favorable due to the similarities in N_{80} of DDB and DBBB, as DDB cannot have 2O-Li coordination. Of note is no significant change in redox potential of the Li⁺ coordination structure compared to the dialkoxyarene, which was also not seen in ref. 41. Li⁺ coordination to MeCN may also influence cycling performance, although it is less likely. Li-MeCN coordination does occur to varying degrees depending on the supporting anion,^{38,40,71,78,79} but its contribution cannot be determined through this work.

3.3.8.3 TEMPO Behavior with Li⁺

While both dialkoxyarenes have beneficial interactions with Li⁺, TEMPO shows variable performance with Li⁺. TEMPO N_{80} improves in LiTFSi but is incompatible with LiPF₆ as shown by comparing the 5/1/TBAPF₆ cell and 5/1/LiPF₆ cell in Figure 3.6.

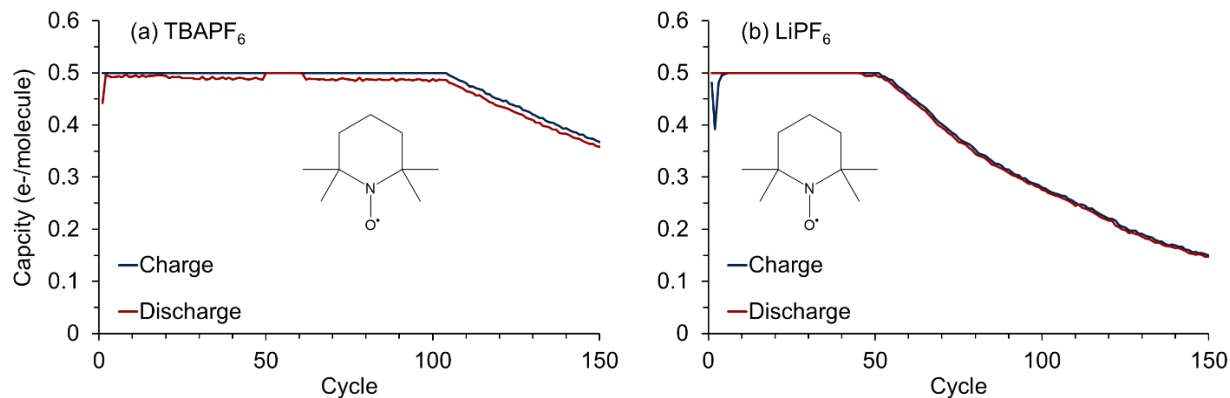


Figure 3.6 Capacity vs cycle plots for (a) TEMPO 5/1/TBAPF₆ and (b) TEMPO 5/1/LiPF₆. The 5/1/LiPF₆ cell has an early onset decay at an N_{80} roughly half of the 5/1/TBAPF₆ cell.

The 5/1/TBAPF₆ cell is one of the “baseline” TEMPO cells, but when the supporting salt cation is changed to Li⁺, N_{80} drops by half despite improved CE . An MD investigation of TEMPO coordination to Li⁺ returned three different coordination behaviors the Li⁺ salts, shown in Figure 3.7.

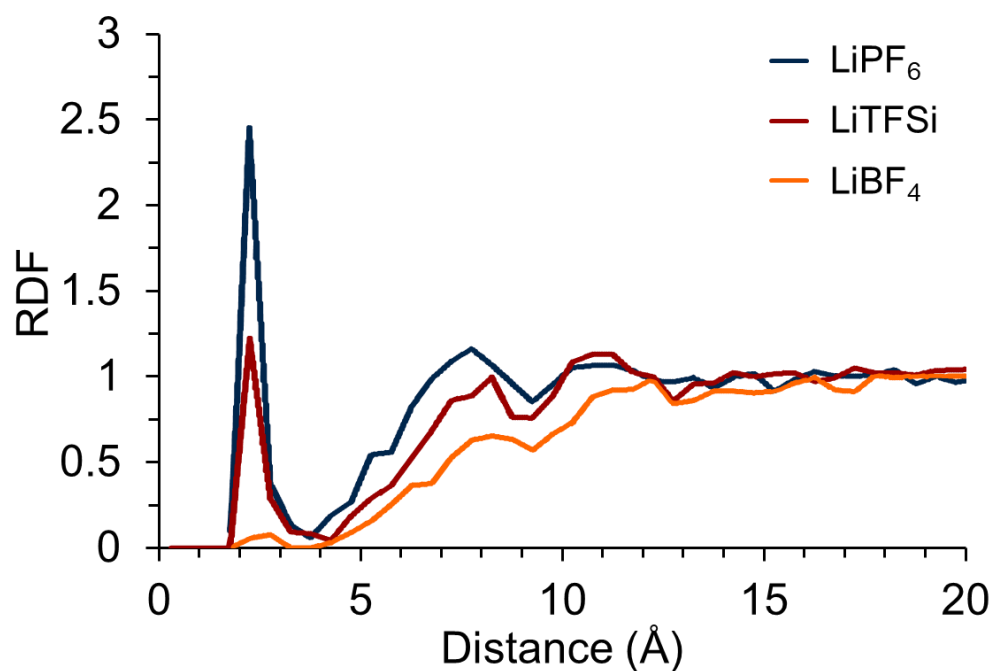


Figure 3.7 Radial distribution function of the TEMPO oxygen to Li⁺ distance. LiPF₆ coordinates strongest, while LiBF₄ shows no coordination.

TEMPO coordination is strongest to LiPF_6 , with moderate coordination to LiTFSi and no coordination to LiBF_4 in this calculation, shown by the peak height at 2.5 Å. This behavior matches salt dissociation trends seen in literature,⁷⁹ which identify LiBF_4 as one of the least dissociative Li^+ salts. Furthermore, there may be an optimal coordination behavior of Li^+ . N_{80} is improved by coordination for TEMPO with LiTFSi but not with LiPF_6 , the most likely-to-coordinate TEMPO-salt combination. DFT investigations of TEMPO- Li^+ -anion structures returned similar coordination structures for each different anion, yielding no additional insight.

3.3.9 Poor Performance at 20 mM/3 C

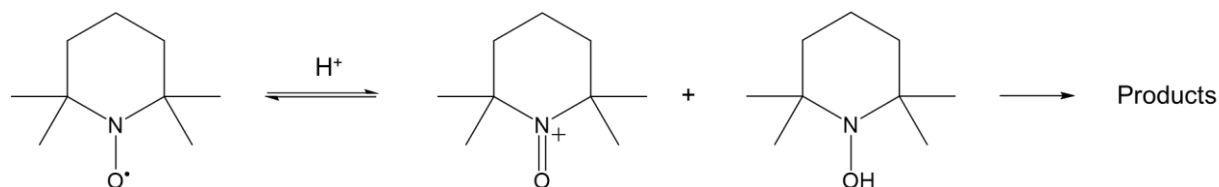
All three active materials performed worse at the 20 mM active material 3 C cycle rate condition, often times not even reaching the N_{80} seen at 1 C despite cycling three times as quickly. This was particularly pronounced with the dialkoxyarene LiBF_4 cells, which had N_{80} 's above 300 in the 5/3/ LiBF_4 and the 20/1/ LiBF_4 conditions but below 100 for the 20/3/ LiBF_4 cell. Experimental conditions which reported excellent results at 5 mM active material at 3 C and 20 mM active material at 1 C (for example, DBBB with LiBF_4), could not replicate that performance at the 20 mM active material at 3 C rate condition. CE at 20 mM and 3 C was among the highest reported at all active material concentration/cycle rate combinations, contrary to the low N_{80} . Two exceptions to this trend were present, DBBB in TBABF_4 and TBAPF_6 . This effect is unexplainable with the work presented in this dissertation and requires more investigation. One hypothesis is the increase in overpotential due to the increased current and cell resistance, which increases the active material oxidation potential to the limits of the supporting salts.

3.3.10 The Impact of Active Material Concentration on N_{80}

The laboratory experiments in this work do not approach the necessary active material concentrations needed for commercial NaRFBs and this work does not provide any insight on the effect molar-order active material concentrations have on N_{80} . With novel research chemicals in particular, there is a desire to minimize the amount of active material used in characterization

experiments. Variation of active material concentration for DDB, DBBB, and TEMPO provides some insight into the effect of active material concentration on N_{80} of TEMPO.

The three active materials of interest all have first order decay of their corresponding cations. For the dialkoxyarenes, this decay is either H-atom abstraction from the solvent back into the parent molecule or through irreversible side reactions, resulting in the observed capacity fade. As DDB and DBBB are stable in the neutral state, N_{80} should not vary based on active material concentration, and any trends are obscured by high N_{80} cell termination and supporting salt effects. TEMPO, alternatively, has both decay of the cation back to the neutral state and decay of the neutral molecule through H-atom abstraction and subsequent disproportionation,⁸⁰ shown in Scheme 3.2.



Scheme 3.2 TEMPO H-abstraction and disproportionation into the N-oxoammonium salt and 2,2,6,6-Tetramethylpiperidin-1-ol.

One of the disproportionation products is the N-oxoammonium cation itself. The rate-limiting step and overall reaction order are unknown, and observed decrease in TEMPO N_{80} with increasing concentration is indicative of an overall reaction order greater than 1.

A general effect of active material concentration is difficult to determine due to the presence of the BF_4^- and TEMPO/LiPF₆ electrolyte interactions. However, some qualitative trends can still be highlighted. First, the increased active material to impurity ratio at 20 mM active material compared to 5 mM led to increases in N_{80} , which are more accurate to the true performance of dialkoxyarenes in these salts. Second, the decrease of TEMPO N_{80} at increased concentration implies the existence of a concentration dependent decay. To further confirm the concentration effect on TEMPO, two BE experiments at 100 mM active material were performed (100/1/TEABF₄ and 100/1/LiTFSi). LiTFSi shows no N_{80} differences between 5 mM and 20 mM active material, likely due to Li⁺ coordination. TEABF₄ was chosen as an alkylammonium control.

Comparative capacity vs cycle plots for these experiments and the 20 mM active material experiments are presented in Figure 3.8. Both the 100 mM TEABF₄ and LiTFSi cells had reduced N_{80} , confirming the presence of a concentration effect and the greater than one reaction order for TEMPO decay.

3.3.11 The Impact of Cycle Rate on N_{80}

In the ideal case, N_{80} would scale linearly with cycle rate and this section would be conclusive. There were three pairs of experiments where this occurred (DDB and DBBB with TBAPF₆, TEMPO with LiPF₆), but the majority of the experiments did not obey this linear scaling. A second, less ideal case would be similar N_{80} no matter the cycle rate, indicative of a fixed N_{80} decay similar to Q5 and Q9 in Chapter 2, but this was only observed for TEMPO 5/1/TBAPF₆ and TEMPO 5/3/TBAPF₆. The remainder of the experiments showed variable cycle rate scaling through the BF₄⁻ impurity, cell termination at high N_{80} , and other unidentified effects. *CE* was at a maximum cycling at 3 C, as expected with a shorter time for cation decay. Additional investigation is necessary to determine the effect of cycle rate on these active materials, however TBAPF₆ can be recommended as a supporting salt which shows linear N_{80} scaling with cycle rate.

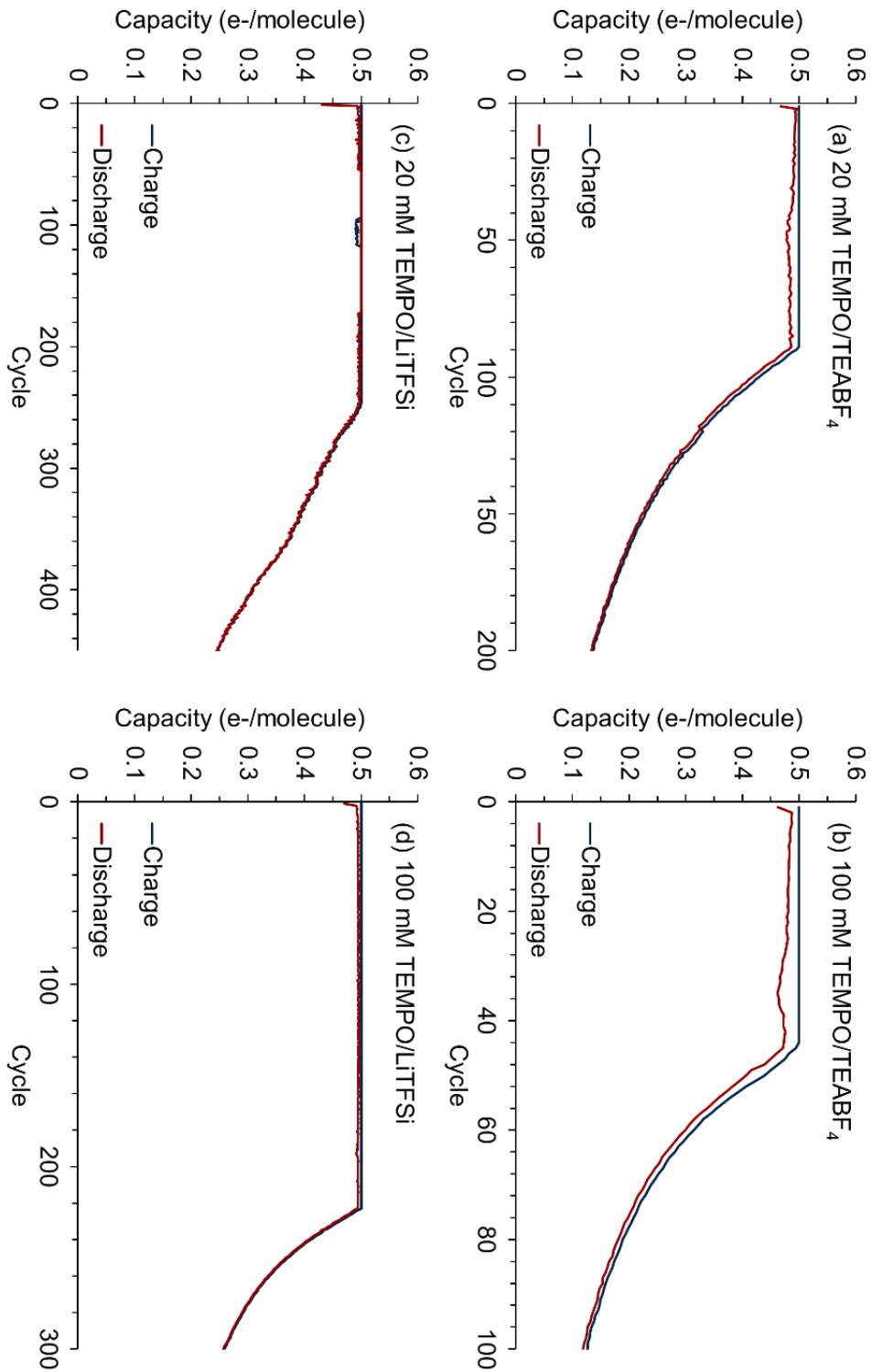


Figure 3.8 Capacity vs cycle plots for TEMPO (a) 20/1/TEABF₄, $N_{80} = 102$, (b) TEMPO 100/1/TEABF₄ $N_{80} = 50$, (c) TEMPO 20/1/LiTFSi, $N_{80} = 328$, and (d) TEMPO 100/1/LiTFSi, $N_{80} = 241$. N_{80} decreases with greater active material concentrations for TEMPO due to its decay reaction order.

3.4 Conclusions

This chapter discussed an extensive set of experiments conducted to isolate and identify the effect of active material concentration, cycle rate, and supporting salt choice on N_{80} . Analysis of active material concentration and cycle rate were difficult due to the significance of supporting salt choice, which overshadowed all other experimental variations. Due to the reaction order of TEMPO decay, active material concentration did have a negative correlation with N_{80} . Investigation of supporting salt interactions with active materials revealed many different interactions between individual active materials and supporting salts. Li^+ coordination was key to extending the N_{80} of all the tested active materials, although there does appear to be an optimal amount of coordination. The stabilization mechanism of the Li^+ coordination was hypothesized to be the same as steric hinderance for the dialkoxyarenes in Chapter 2, decreasing the rate of O-dealkylation by reducing access to the ether oxygens. Lastly, LiPF_6 and TBAPF_6 are recommended to achieve the greatest N_{80} for dialkoxyarenes and as a baseline comparison for other results, respectively. Significant negative interactions occurred between active materials and BF_4^- salts, which should be avoided until the active impurity present in those salts can be removed. This work also reported the best cycling ROM to date, with DDB 20/1/ LiPF_6 cycling for 1073 cycles. Overall, this work introduces Li^+ coordination as an alternative to steric hinderance as a stabilization strategy for ROM design and the importance of electrolyte composition on proper characterization.

3.5 Acknowledgements

I would like to thank Dr. Jingjing Zhang from Dr. Lu Zhang's group for his collaborative efforts on this project. He was responsible for dialkoxyarene synthesis in this Chapter. I would also like to thank Dr. Zhou Yu from ANL for his efforts. He was responsible for the MD simulations.

Chapter 4

A Kinetic Model for Redox Active Organic Molecule Cycling

Portions of this chapter are adapted with permission from B. Silcox, J. Zhang, I. Shkrob, L. Thompson, L. Zhang; Journal of Physical Chemistry C (2019). Copyright 2019 American Chemical Society

4.1 Background and Approach

Development of high cyclability active materials is a critical issue for non-aqueous redox flow battery (NaRFB) advancement.^{58,81} As demonstrated in Chapter 3, the factors affecting cyclability are numerous and their interactions with active materials are complex.^{41,73} For this reason, performance comparisons for active materials across literature or laboratories are often difficult if identical experiments are not performed. Compounding this difficulty is the lack of metrics for cyclability. Cycle life (N_q) is the primary metric but is simple and empirical, unable to standardize variable experimental conditions. N_q in particular does a poor job at high cycle rates, exaggerating performance for active materials that have a calendar life component to their fade. Cell lifetime, another metric, has the opposite problem, overestimating performance at low cycle rates and active materials that are only stable in the absence of redox activity. To make improved cyclability comparisons, new metrics, ideally with a theoretical basis, are needed.

In this chapter, I introduce a kinetic model of H-cell bulk electrolysis (BE) cycling experiments and use it to derive a new metric for evaluating cyclability. This model is applied to the experimental data presented in Chapters 2 and 3 to gain additional insight into their cycling behavior. This work establishes a new, kinetic metric for cycling experiments, which suppresses the effect of active material concentration and cycle rate.

4.1.1 Model Development

Ideally, this new model would have a basis in chemical kinetics, so a simple kinetic model for BE cycling was developed. From the experimental setup discussed in Chapter 2, we begin with the initial redox active organic molecules (ROM) concentration C_0 and the cell volume V . For the experiments in Chapters 2 and 3, we picked T , the theoretical cycling period, and defined the current in the cell, I by $I = C_0VF/T$, where F is Faraday's constant. If a specific current was instead desired, T could be calculated from the same relationship. Active material decay behavior was modeled from experimental observation. The dialkoxyarene family has demonstrated first-order decay of the charged species with a rate constant k ,^{82,83} with this decay either recovering the original active material or proceeding into irreversible side reactions. We define the yield of this recovery reaction as ϕ and $\bar{\phi} = 1 - \phi$ as the irreversible decay. Lastly, to complete our basic kinetic model, the concentration of the uncharged active species is defined as C and the concentration of the charged active species as C^* . Combining these variables into two first order rate equations, we have

$$dC/dt = \mp \frac{I}{VF} + \phi kC^* \quad (4.1)$$

$$dC^*/dt = \pm \frac{I}{VF} - kC^* \quad (4.2)$$

where the upper/lower signs denote charge and discharge cycles respectively (concentration of the uncharged active material decreases during charge, and increases during discharge). Before any cycling is performed at $t = 0$, $C^* = 0$ and $C = C_0$.

When cycling, the cell first undergoes constant current charge until either a time cutoff (equivalent to a desired capacity cutoff) is reached or the cell reaches its voltage cutoffs. The time/capacity cutoff is defined by $T' = \eta T$, where η is the desired state of charge (SOC). For simplicity, the voltage cutoff is ignored in the mathematical model. When one of these two cutoffs are reached, the current is reversed and the cell discharges back to the uncharged state. Charge and discharge times are defined as T_c and T_d ; note that T_c and T_d have a theoretical maximum of T' . N_q , the number of cycles before discharge capacity reaches a percentage capacity, can now be defined at qT_d , where q is the capacity cutoff.

When $\eta < 1$, the immediate capacity fade is not apparent, and only appears when the concentration of ROM during charge decreases below the theoretical capacity. This creates two regimes of cycling, one where we see no observable capacity fade and one where we do. We can define $N_{<}$ as the number of cycles in this first regime, and $N_{>} = N_q - N_{<}$ as the number of cycles in the second regime before reaching N_q . An illustration of these regimes is shown in Figure 4.1.

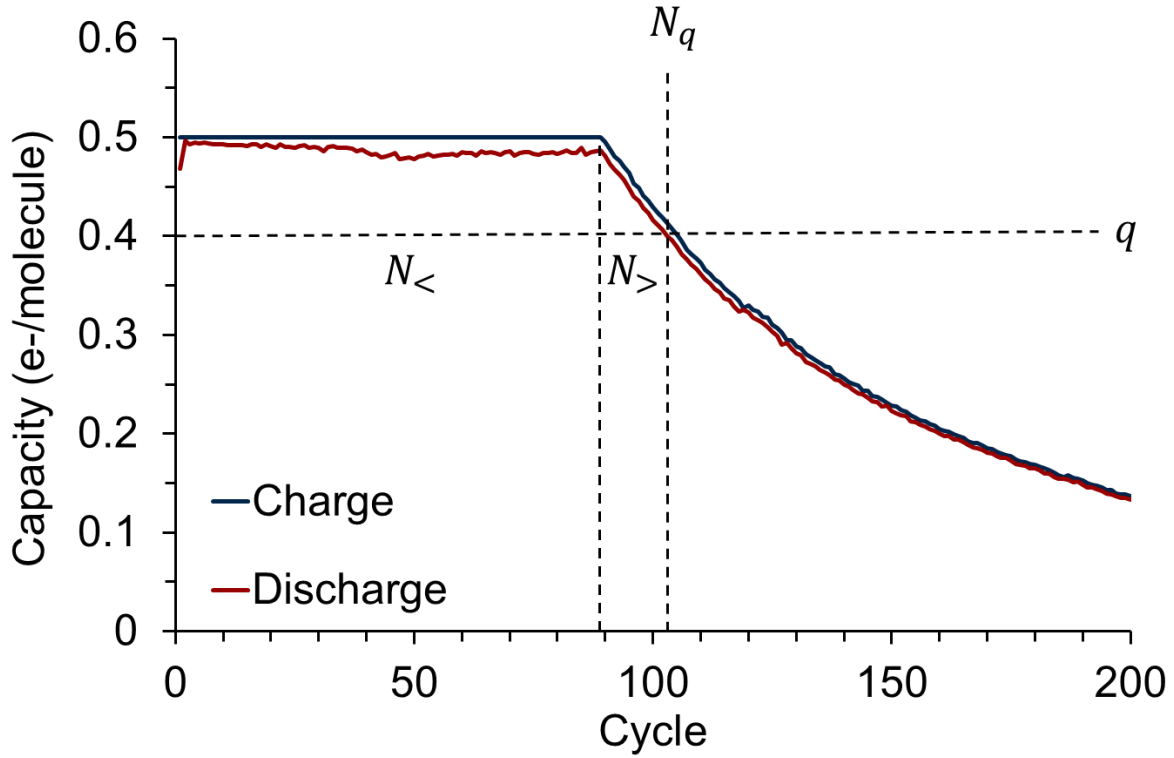


Figure 4.1 A graphical representation of the cycling regimes N_q , $N_{<}$, and $N_{>}$. $N_{<}$ extends to the end of the constant capacity plateau, followed by $N_{>}$ until the capacity cutoff q is reached.

Defining these cycling parameters in the model provides a target for the derivation, as they can be measured experimentally.

To simplify calculations, dimensionless parameters $c = C/C_0$, $c^* = C^*/C_0$, $\kappa = kT$, and reduced time τ , are introduced. Equations 4.1 and 4.2 are rewritten as

$$dc/d\tau - \phi\kappa c^* = \mp 1 \quad (4.1a)$$

$$dc^*/d\tau + \kappa c^* = \pm 1 \quad (4.2a)$$

In mathematical terms, charge of the cell ends when $\tau_c = \eta$ (for $c \geq \eta$) or $c = 0$ for ($c < \eta$), while discharge always ends at $c^* = 0$. Due to the charged active material decay, the discharge capacity is always less than the charge capacity so the capacity limit can never be reached during discharge in a well-behaved cell. Solving Equation 4.2a analytically allows us to obtain the dimensionless concentrations at the end of a charge-half cycle,

$$c^* = \frac{1 - e^{-\kappa\tau_c}}{\kappa} \quad (4.3)$$

$$c = c_n - \bar{\phi}\tau_c - \phi c^* \quad (4.4)$$

where c_n is the dimensionless concentration at the completion of cycle n . Taking the series expansions of Equations 4.3 and 4.4 for the practically important limit of $\kappa\tau_c \ll 1$ gives

$$c^* = \frac{1 - e^{-\kappa\tau_c}}{\kappa} \approx \tau_c \left(1 - \frac{\kappa\tau_c}{2}\right) \quad (4.3a)$$

$$c = c_n - \bar{\phi}\tau_c - \phi c^* \approx c_n - \tau_c + \phi k\tau_c^2/2 \quad (4.4a)$$

while $c_n \geq \eta$, $\tau_c = \eta$. For $c_n < \eta$, a second series expansion of Equation 4.4a is needed and can be approximated as

$$\tau_c \approx c_n \left(1 + \frac{\phi\kappa c_n}{2}\right) \quad (4.5)$$

A similar manner of solving for τ_d from Equation 4.2a gives

$$\tau_d = \frac{\ln(1 + \kappa c^*)}{\kappa} \quad (4.6)$$

And finally, Equation 4.3 can be substituted into Equation 4.6 and a series expansion used to get τ_d in terms of τ_c

$$\tau_d \approx \tau_c(1 - \kappa\tau_c) \quad (4.7)$$

With expressions for the time of charge and discharge, the concentration at the end of each cycle can be determined

$$c_{n+1} = c - \bar{\phi}\tau_d + \phi c^* \quad (4.8)$$

With c and c^* at the end of each cycle from Equations 4.3a and 4.4a respectively

$$c_{n+1} \approx c_n - \bar{\phi}\kappa\tau_c^2 \quad (4.9a)$$

For $c_n \geq \eta$, $\tau_c = \eta$ and the concentration c_n decreases with each cycle by a constant value

$$c_n \approx 1 - \bar{\phi} n \kappa \eta^2 \quad (4.9b)$$

This leads to a fairly simple expression for $N_{<}$, which is defined at $c_n = \eta$

$$N_{<} \approx \frac{1-\eta}{\bar{\phi} \kappa \eta^2} \quad (4.10)$$

$N_{>}$ is defined by the number of cycles to reach a specific capacity cutoff. This is defined by the discharge cycle, giving $\tau_d = \eta q$. With the previous assumption $\kappa \tau_c \ll 1$, Equation 4.5 gives $\tau_d \approx \tau_c \approx c_n \approx \eta q$. A new expression can then be derived from Equations 4.5 and 4.9a

$$c_{n+1} - c_n \approx \frac{dc_n}{dn} \approx -\bar{\phi} \kappa c_n^2 (1 + \phi \kappa c_n) \quad (4.11)$$

Integrating to find $N_{>}$

$$\bar{\phi} \kappa N_{>} \approx \int_{\eta q}^{\eta} \frac{dc}{c^2 (1 + \phi \kappa c)} \quad (4.12)$$

If $\phi = 0$, a simple expression exists for $N_{>}$

$$N_{>} \approx \frac{1-q}{q \kappa \eta} \quad (4.13a)$$

And $N_q = N_{<} + N_{>}$ with a series expansion of Equation 4.9b

$$N_q \approx \frac{1}{\kappa \eta} \left(\frac{1-\eta}{\eta} + \frac{1-q}{q} \right) \quad (4.13b)$$

For the more relevant $\phi \neq 0$ case

$$N_{>} \approx \frac{1-q}{\bar{\phi} q \kappa \eta} - \frac{\phi}{\bar{\phi}} \ln \frac{1 + \phi \kappa \eta}{1/q + \phi \kappa \eta} \quad (4.14a)$$

$$N_q \approx \frac{1}{\bar{\phi} \kappa \eta} \left(\frac{1-\eta}{\eta} + \frac{1-q}{q} \right) - \frac{\phi}{\bar{\phi}} (\ln q + \phi \kappa \eta (1-q)) \quad (4.14b)$$

This derivation made the assumption that $\kappa \eta \ll 1$, which corresponds to a relatively small decay rate and low theoretical capacity loss per cycle. For the NaRFB space, fast decay and high capacity loss per cycle is uninteresting, as those active materials will not have the necessary stability or cyclability.

The model relates experimentally measured N_q to ϕ , which is a kinetic performance metric. ϕ is not dependent on active material concentration or cycle rate, although any significant electrolyte interactions affecting N_q will still be transferred to ϕ . Equation 4.14b requires an additional experimental value, in this case κ , the dimensionless rate constant. Finding

κ can be even more time consuming than N_q , as these measurements require resonance spectroscopy techniques and κ s have been reported in the hundreds of hours.^{48,74,83} To be most useful for cyclability characterization, an equation for ϕ would only require data from BE cycling.

From the original kinetic model, $1 - \kappa\eta^2$ is the theoretical maximum coulombic efficiency (CE). While BE experiments don't measure theoretical CE , we can still substitute experimental CE for κ in Equation 4.14b

$$N_q \approx \frac{1}{\bar{\phi} \frac{(1-CE)}{\eta}} \left(\frac{1-\eta}{\eta} + \frac{1-q}{q} \right) - \frac{\phi}{\bar{\phi}} \left(\ln q + \phi \frac{(1-CE)}{\eta} (1-q) \right) \quad (4.15)$$

Equation 4.15 can be used to calculate ϕ for any BE experiment, even if the active material does not have published stability data.

4.1.1.1 Model Variation for TEMPO

Of the active materials investigated in this thesis, (2,2,6,6-Tetramethylpiperidin-1-yl)oxyl (TEMPO) is unique due to an additional decay mechanism from the neutral state.⁸⁰ Assuming first order decay, an additional term is added to the initial kinetic model in Equation 4.1

$$dC/dt = \mp \frac{I}{VF} + \phi kC^* - k_{TEMPO}C \quad (4.16)$$

$$dC^*/dt = \pm \frac{I}{VF} - kC^* \quad (4.17)$$

The expressions for τ_c and τ_d are now

$$\tau_c \approx c_n \left(1 + \frac{\phi \kappa c_n}{2} - \frac{\kappa_{TEMPO} c_n}{2} \right) \quad (4.18)$$

$$\tau_d = \frac{\ln(1 + \kappa c^*)}{\kappa} \quad (4.19)$$

τ_d remains the same as the original derivation, as Equation 4.16 and 4.2 are identical. The expression for c_{n+1} is now

$$c_{n+1} \approx c_n - \bar{\phi} \kappa \tau_c^2 - \kappa_{TEMPO} \tau_c^2 - \kappa_{TEMPO} \tau_c^2 (1 + \kappa \tau_c^2 - 2\kappa \tau_c) \quad (4.20)$$

The expression for $N_{<}$ proceeds from the same conditions, $\tau_c = c_n = \eta$, with constant capacity fade for each cycle

$$N_{<} \approx \frac{(1 - \eta)}{\left(\bar{\phi} \kappa \eta^2 + \kappa_{TEMPO} \left(1 - \frac{\eta^2}{2} \right) + \kappa_{TEMPO} \left(1 - \frac{\eta^2(1 - \kappa \eta)^2}{2} \right) \right)} \quad (4.21)$$

With Equation 4.20, the integrand to find $N_{>}$ is no longer integrable. For sufficiently long N_q , small η (0.5, which is used in this thesis, is sufficient), and high q , $N_{>} \ll N_{<}$ and the expression for $N_{>}$ in Equation 4.13b is a reasonable approximation. The majority of active material decay should occur in the cycling regime described by $N_{<}$. The final form of the recovery equation is

$$N_q = (1 - \eta) \left(\frac{1}{\bar{\phi} \kappa \eta^2 + \kappa_{TEMPO} \left(1 - \frac{\eta^2}{2} \right) + \kappa_{TEMPO} \left(1 - \frac{\eta^2(1 - \kappa \eta)^2}{2} \right)} + \frac{1}{\bar{\phi} \kappa \eta^2} \right) + \frac{1 - q}{\bar{\phi} q \kappa \eta} + \frac{\phi}{\bar{\phi}} (\ln q + \phi \kappa \eta (1 - q)) \quad (4.22)$$

The $CE = 1 - \kappa \eta^2$ substitution can be made to reduce the dependence on kinetic data, giving the final form of the equation for TEMPO

$$N_q = \frac{(1 - \eta)}{\bar{\phi}(1 - CE) + \kappa_{TEMPO} \left(1 - \frac{\eta^2}{2} \right) + \kappa_{TEMPO} \left(1 - \frac{\eta^2 \left(1 - \frac{(1 - CE)}{\eta} \right)^2}{2} \right)} + \frac{(1 - \eta)}{\bar{\phi}(1 - CE)} + \frac{1 - q}{\bar{\phi} q \frac{(1 - CE)}{\eta}} + \frac{\phi}{\bar{\phi}} \left(\ln q + \phi \frac{(1 - CE)}{\eta} (1 - q) \right) \quad (4.23)$$

Unfortunately, Equation 4.23 does require κ_{TEMPO} to be measured experimentally, a condition which applies to all active materials with decay of the uncharged species.

4.2 Experimental

4.2.1 TEMPO Stability Measurements

Solutions of TEMPO and 4-acetomido TEMPO (> 99%, Sigma Aldrich) were prepared for spectroscopy in fritted glass H-cells. 20 mM of the active material was solvated with 500 mM lithium bis(trifluoromethanesulfonyl)amide (LiTFSi) (Sigma Aldrich) in 10mL acetonitrile (MeCN) (Acros Organics). The H-cell contained working and counter electrodes composed of reticulated

vitreous carbon (Duocell). The reference electrode was a fritted chamber containing 10 mM of a silver bis(trifluoromethanesulfonyl)amide (AgTFSi) and a silver wire. A BioLogic VSP potentiostat recorded all data.

The electrolyte was charged at a rate of 5 C to 100% SOC. A 20 μL sample of the charged electrolyte was placed in a glass capillary and sealed. The neutral radical was observed using electron paramagnetic resonance (EPR) spectroscopy in the X-band using 100 kHz field modulation. The first-derivative EPR spectra were collected at room temperature using a Bruker EMX X-band spectrometer operating at 9.69 GHz. For kinetic analysis, the EPR spectra was recorded at the constant time intervals, centered, background corrected, and doubly integrated. The decay kinetics were fit by a biexponential function, one for the decay of the cation and one for the decay of the TEMPO radical.

4.3 Results and Discussion

4.3.1 ϕ

A plot of ϕ vs N_{80} for different CE is shown in Figure 4.2. From Figure 4.2, ϕ becomes more descriptive as CE increases, providing more information for low N_{80} cells. ϕ as a metric fails at for active materials with low N_{80} and low CE , although these poorly performing active materials are not the target for development and can be safely neglected.

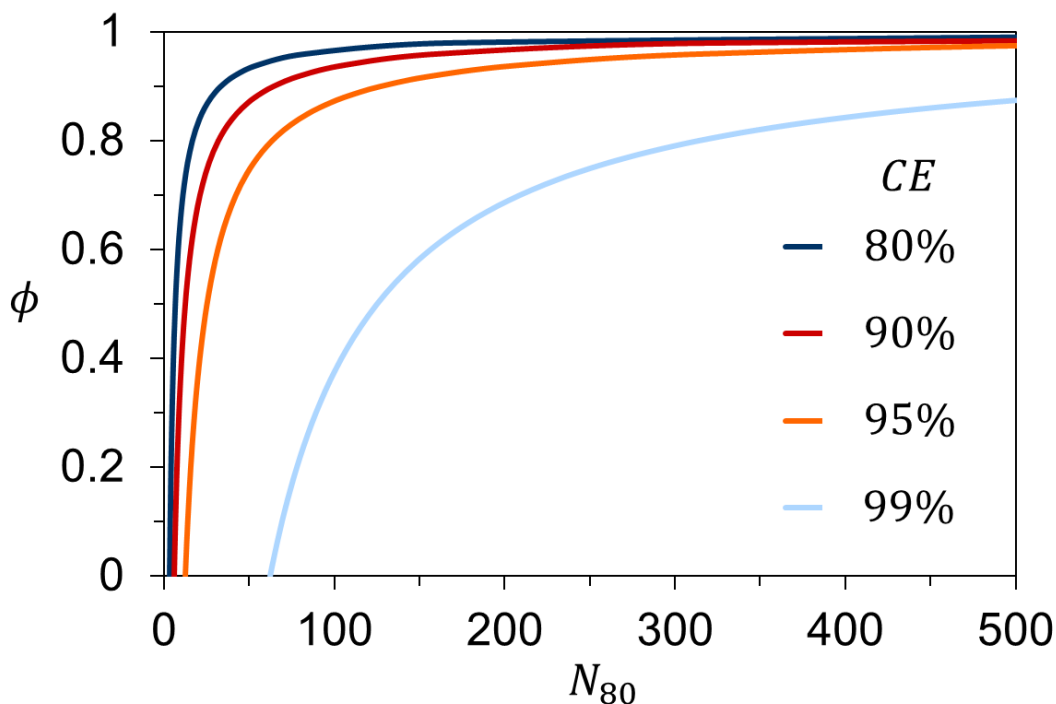


Figure 4.2 ϕ vs N_{80} in Equation 15 for different CE at $\eta = 0.5, q = 0.8$. As CE increases, ϕ shows greater variation at low N_{80} . Materials with sufficiently high CE have a theoretical minimum N_{80} .

4.3.2 Maximum CE

As a byproduct of model development, an expression was developed for maximum theoretical CE , $1 - \kappa\eta^2$. If stability data exists for an active material, exceeding the theoretical maximum CE indicates that there is a structural change of the active material in the cell, such as Li^+ coordination. Cation stabilities, reported as half-lives ($t_{\frac{1}{2}}$), for 1,4-Di-*tert*-butyl-2,5-dimethoxybenzene (DDB) and 1,4-Di-*tert*-butyl-2,5-bis (2-methoxyethoxy)benzene (DBBB) have been recorded ($t_{\frac{1}{2}} = 26.5$ h and 26.1 h respectively), TEMPO⁺ stability was found from EPR, $t_{\frac{1}{2}} = 106.5$ h. Table 4.1 contains the theoretical maximum CE for DDB, DBBB, and TEMPO at 1 C and 3 C cycle rates.

Table 4.1 Theoretical maximum CE for DDB, DBBB, and TEMPO. CE greater than the theoretical maximum in a BE experiment requires a change in the active material structure.

Molecule	DDB	DBBB	TEMPO
$CE_{max,1C}$	99.3%	99.3%	99.8%
$CE_{max,3C}$	99.8%	99.8%	99.9%

4.3.3 Recovery Summary

Chapter 3 illustrated the difficulty in comparing active materials at different experimental conditions due to the significance of supporting salt effects overshadowing active material concentration and cycle rate. Calculating ϕ for each of these experiments provides a renewed opportunity to understand the variations in N_{80} , although electrolyte effects may still dominate. Similarly, the cycling experiments from Chapter 2 provides an opportunity for greater comparison of recovery with structural similarity. Table 2.2 has been updated with ϕ in Table 4.2, which reports N_{80} , CE , and ϕ arranged by active material. A plot of ϕ vs N_{80} is shown in Figure 4.3.

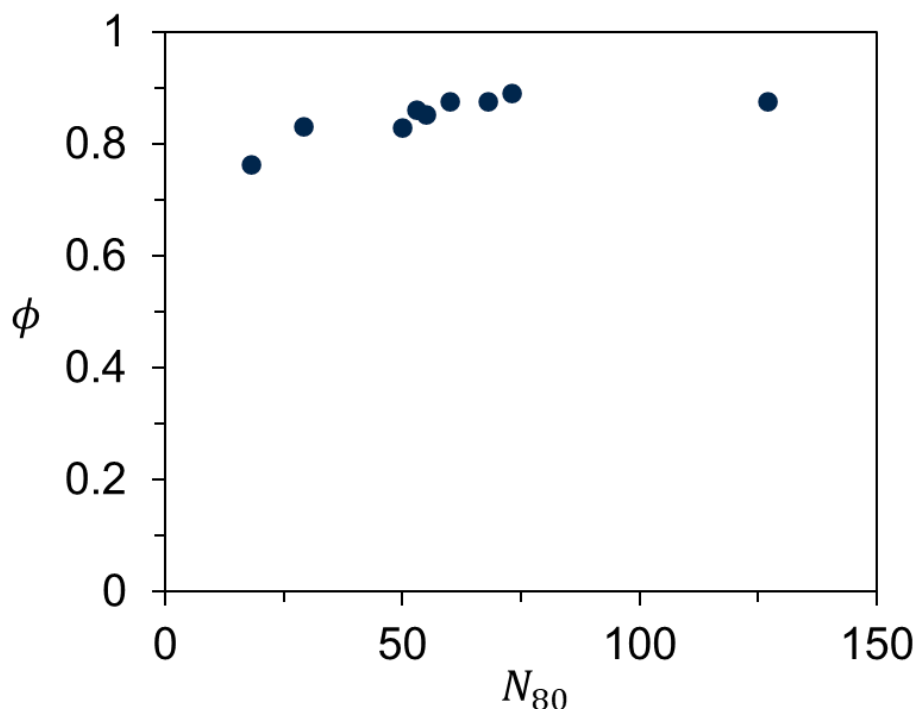


Figure 4.3 ϕ vs N_{80} for the dialkoxyarene catholytes in Table 4.2.

Table 4.2 Names, structures, cycle lives, coulombic efficiencies, and recoveries from BE experiments of the dialkoxyarene catholytes. All values are averages when multiple experiments were performed.

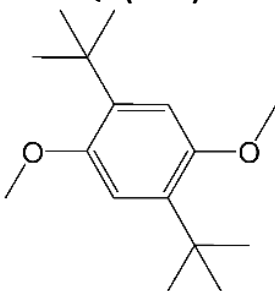
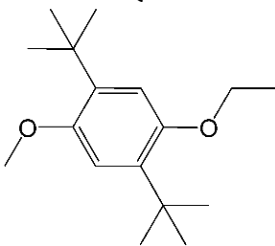
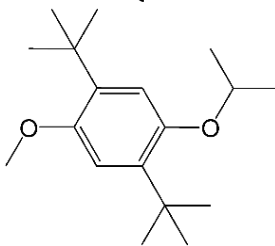
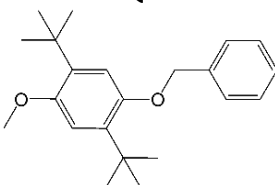
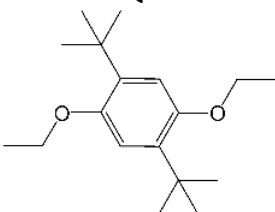
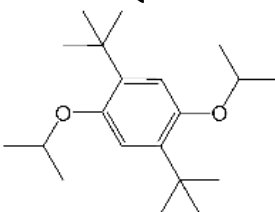
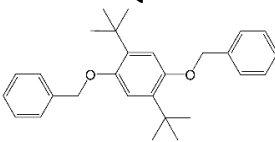
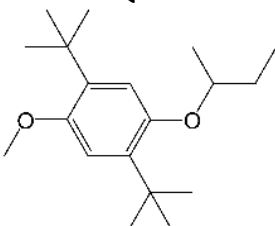
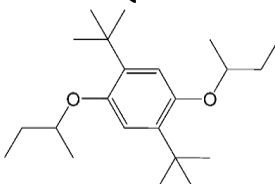
Molecule Structure	Q1 (DDB) 	Q2 	Q3 
\bar{N}_{80}	68	60	50
\overline{CE}	92.4%	89.7%	92.5%
ϕ	0.877	0.877	0.830
Molecule Structure	Q5 	Q6 	Q7 
\bar{N}_{80}	29	53	73
\overline{CE}	86.7%	91.2%	91.9%
ϕ	0.832	0.862	0.832
Molecule Structure	Q9 	Q10 	Q11 
\bar{N}_{80}	18	55	127
\overline{CE}	84.9%	92.0%	96.3%
ϕ	0.763	0.853	0.876

Figure 4.3 shows a slight positive correlation between ϕ and N_{80} , although ϕ for all the dialkoxyarenes with the exception of Q9 were between 0.83 and 0.88. These results suggest, with the exception of Q9, that this series of dialkoxyarenes has the same kinetic cycling performance and N_{80} is only related to the rate of cation decay.

Tables and 3.2 – 3.4 have been updated with ϕ in Tables 4.3 – 4.5, which report N_{80} , CE , and ϕ arranged by active material, concentration, cycle rate, and supporting salt in sequence. $k_{TEMPO} = 0.0129 \text{ h}^{-1}$ was found from the TEMPO stability EPR experiment and used for all ϕ values in Table 4.5. Plots of ϕ vs N_{80} for DDB, DBBB, and TEMPO are shown in Figure 4.4 – 4.6 respectively.

Table 4.3 Name, structure, active material concentration, cycle rate, supporting salt, cycle life, coulombic efficiency, and recovery for DDB. The alkylammonium supporting salts were not cycled at 20 mM active material concentration due to solubility limitations of DDB. Cells that terminated prematurely are marked with an asterisk.

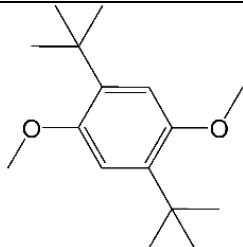
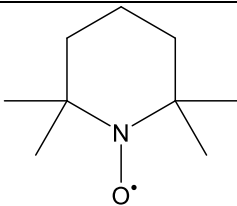
Molecule	Structure	Active Material Concentration	Cycle Rate	Supporting Salt	N_{80}	CE	ϕ	
DDB		5 mM	1 C	TBABF ₄	16	76.0%	0.828	
				TBAPF ₆	68	92.4%	0.876	
			TEABF ₄	21	78.1%	0.856		
			LiBF ₄	48	91.8%	0.838		
			LiPF ₆	498*	98.6%	0.910		
			LiTFSi	623*	95.3%	0.978		
			3 C	TBABF ₄	19	86.3%	0.752	
				TBAPF ₆	168	98.1%	0.804	
				TEABF ₄	35	91.9%	0.775	
			20 mM	1 C	LiBF ₄	620*	93.5%	0.984
		LiPF ₆			1073	98.9%	0.947	
		LiTFSi			447	98.9%	0.873	
		3 C			LiBF ₄	86	94.8%	0.859
					LiPF ₆	210	98.4%	0.818
		LiTFSi	172	96.9%	0.883			

Table 4.4 Name, structure, active material concentration, cycle rate, supporting salt, cycle life, coulombic efficiency, and recovery for DBBB. Cells that terminated prematurely are marked with an asterisk.

Molecule	Structure	Active Material Concentration	Cycle Rate	Supporting Salt	N_{80}	CE	ϕ
DBBB		5 mM	1 C	TBABF ₄	21	82.5%	0.823
				TBAPF ₆	63	89.6%	0.902
				TEABF ₄	26	84.5%	0.839
				LiBF ₄	70	93.1%	0.868
				LiPF ₆	941*	98.1%	0.966
				LiTFSi	883*	93.1%	0.990
			3 C	TBABF ₄	48	91.9%	0.835
				TBAPF ₆	165	96.8%	0.880
				TEABF ₄	32	88.5%	0.825
				LiBF ₄	756*	98.2%	0.954
				LiPF ₆	2696*	99.6%	0.970
				LiTFSi	582	96.4%	0.954
		20 mM	1 C	TBABF ₄	26	71.7%	0.909
				TBAPF ₆	33	87.2%	0.847
				TEABF ₄	176	96.7%	0.891
				LiBF ₄	648*	95.9%	0.976
				LiPF ₆	548	99.3%	0.832
				LiTFSi	439	96.0%	0.964
3 C	TBABF ₄		137	97.8%	0.790		
	TBAPF ₆		131	98.2%	0.729		
	TEABF ₄		163	97.4%	0.851		
	LiBF ₄		72	95.7%	0.795		
	LiPF ₆		461	95.7%	0.968		
	LiTFSi		242	98.4%	0.838		

Table 4.5 Name, structure, active material concentration, cycle rate, supporting salt, cycle life, coulombic efficiency, and recovery for TEMPO. No TEMPO cells terminated prematurely. $k_{TEMPO} = 0.0129 h^{-1}$ was used for all calculations of ϕ .

Molecule	Structure	Active Material Concentration	Cycle Rate	Supporting Salt	N_{80}	CE	ϕ
TEMPO		5 mM	1 C	TBABF ₄	129	98.0%	0.942
				TBAPF ₆	132	98.0%	0.944
				TEABF ₄	131	98.8%	0.909
				LiBF ₄	182	99.9%	0.229
				LiPF ₆	68	99.5%	0.451
				LiTFSi	323	98.5%	0.972
			3 C	TBABF ₄	89	97.8%	0.864
				TBAPF ₆	132	99.0%	0.837
				TEABF ₄	254	99.1%	0.925
				LiBF ₄	155	100.0%	0.0
				LiPF ₆	141	99.7%	0.507
				LiTFSi	366	99.2%	0.950
		20 mM	1 C	TBABF ₄	118	98.1%	0.932
				TBAPF ₆	149	98.9%	0.908
				TEABF ₄	102	97.3%	0.941
				LiBF ₄	142	99.9%	0.317
				LiPF ₆	67	98.8%	0.787
				LiTFSi	328	98.9%	0.963
			3 C	TBABF ₄	93	98.4%	0.826
				TBAPF ₆	118	98.7%	0.853
				TEABF ₄	156	99.0%	0.873
LiBF ₄	105			99.5%	0.500		
LiPF ₆	178			100.0%	0.0		
LiTFSi	193			99.5%	0.818		

With the exception of five TEMPO cells discussed later, ϕ values above 0.5 indicate that the decay of undischarged cations for these molecules favors a return to the parent compound. Like N_{80} , ϕ in Tables 4.3 – 4.5 is a lower bound due to the premature termination of some cells and derivation from N_{80} . For all three active materials, N_{80} and ϕ show the same weak positive correlation as the dialkoxyarenes catholytes in Figure 4.3.

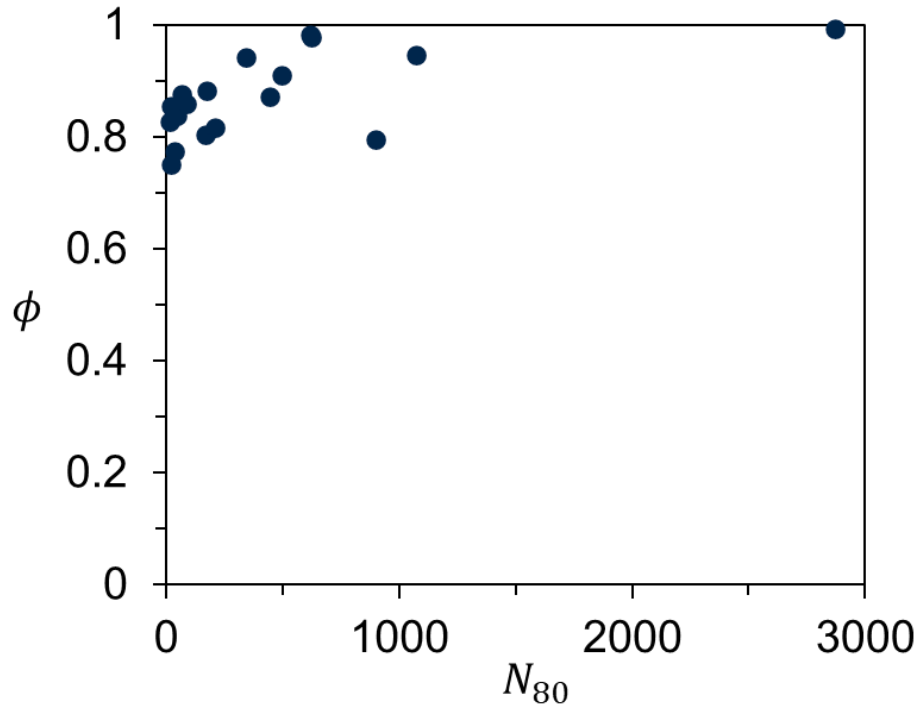


Figure 4.4 ϕ vs N_{80} for the DDB experiments in Table 4.3.

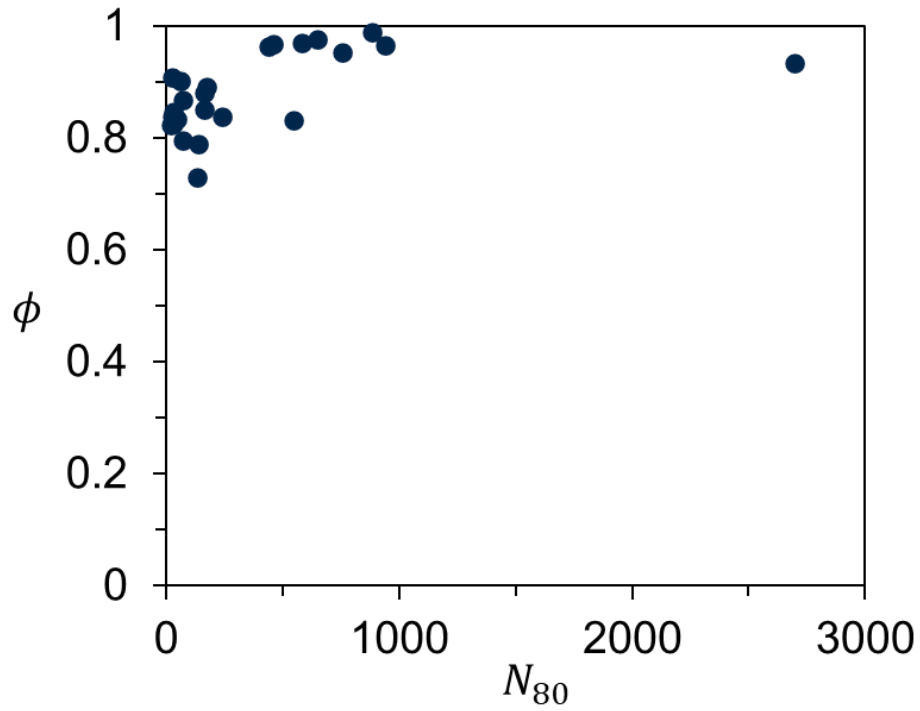


Figure 4.5 ϕ vs N_{80} for the DBBB experiments in Table 4.4.

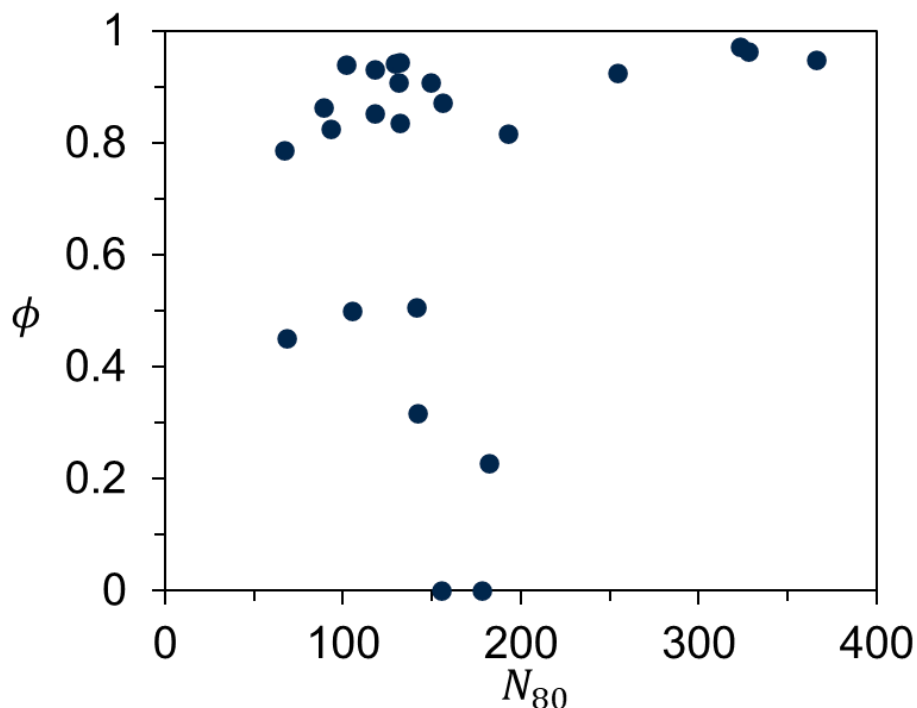


Figure 4.6 ϕ vs N_{80} for the TEMPO experiments in Table 4.5.

Figure 4.6 highlights the poor kinetic performance of TEMPO with LiPF_6 and LiBF_4 , which are separated from the remainder of the experiments with low ϕ .

4.3.4 Cells above Maximum CE

None of the Chapter 2 dialkoxyarenes, which were all cycled in tetrabutylammonium hexafluorophosphate (TBAPF_6), reported greater than maximum CE . This is expected, as there is no evidence of alkylammonium coordination to active materials.

Of the DDB, DBBB, and TEMPO cycling variation experiments in Chapter 3, five cells reported CE at or above the theoretical maximum. All of these cells used Li^+ supporting salts. One of these was DBBB 20/1/ LiPF_6 . This further confirms the suspected Li^+ stabilization of the dialkoxyarenes, as structural changes to the active material must occur to reach this CE .

Four TEMPO cells reported CE above the theoretical limit, three lithium tetrafluoroborate (LiBF_4) cells (5/1/ LiBF_4 , 5/3/ LiBF_4 , 20/1/ LiBF_4) and 20/3/ LiPF_6 . Three LiBF_4 cells on this list are surprising, as LiBF_4 showed no coordination to TEMPO by a molecular dynamics investigation in

Chapter 3. The 20/3/LiPF₆ cell's appearance is likely due to its strong Li⁺-coordination, all four TEMPO lithium hexafluorophosphate (LiPF₆) cells had high *CE*.

4.3.5 New Insights from ϕ

For the Chapter 2 dialkoxyarene characterization, ϕ confirms the increased decay of Q5 and Q9, which were among the lowest ϕ values of the series. Besides Q9 ($\phi = 0.763$), there was no significant difference in ϕ for the other dialkoxyarenes.

Unfortunately, ϕ cannot suppress the supporting salt interactions affecting N_{80} . For this reason, there is no significant understanding of the active materials gained by investigating ϕ for the cycling experiments in Chapter 3. ϕ for DDB and DBBB confirms the significant impact BF₄⁻ supporting salts have on performance. In addition to accelerating the decay of the dialkoxyarene cations, the impurity appears to increase the yield of the O-dealkylation side reaction through an unknown mechanism. LiPF₆ and lithium bis(trifluoromethanesulfonyl)amide (LiTFSi) experiments had ϕ ranging from 0.8 to 0.99, too wide a range for there to be a consistent effect from Li⁺ coordination. The coordination may have multiple effects on dialkoxyarenes, both decreasing the overall decay rate of the cation and inhibiting the O-dealkylation reaction. The balance of these effects is either due to variations within the individual experimental set ups or is dependent on specific active material-salt interactions and requires further investigation.

The four TEMPO LiBF₄ cells, three with unphysical *CE*, had several of the lowest ϕ in the BE experiments. With no TEMPO-LiBF₄ coordination, two hypotheses for this abnormal interaction are the cycling of the active impurity in LiBF₄ or TEMPO interactions with the impurity that were unobvious from N_{80} . Cycling of this active impurity, if more stable in the charged state than TEMPO, would account for the unphysical *CE* and the low ϕ . Additionally, the TEMPO LiBF₄ system is the most likely active material-supporting salt combination for TEMPO-impurity interactions. LiBF₄ dissociates poorly in and coordinates well to MeCN, which would bring the impurity in closer proximity to TEMPO compared to other supporting salts. These mechanisms may occur in combination and LiBF₄ should be avoided for further TEMPO characterization due to the active impurity interactions.

4.4 Conclusions

This chapter discussed the development of a kinetic model and parameter, ϕ , with applications for improved cycling comparisons. Unlike N_{80} , ϕ normalizes for material concentration and cycle rate, but still cannot suppress active material-supporting salt interactions. Due to electrolyte effects still appearing in ϕ , few additional insights were made from the results presented in Chapter 3. The most significant is a newly identified interaction between TEMPO and the active impurity in LiBF_4 . In the process of developing this model, the maximum theoretical CE was identified and can be calculated for active materials with reported decay rates. This CE can be used to identify cycling experiments which contain structural changes to the active material during cycling such as Li^+ coordination. Overall, this work introduces a second metric for active material cycling comparison, which can be used to compare experiments independent of active material concentration and cycle rate.

4.5 Acknowledgements

I would like to thank Dr. Ilya Shkrob from ANL for his collaborative efforts developing the cycling model. I would also like to thank James Windak at UM for his assistance with EPR experiments.

Chapter 5

Stability Predictions for Redox Active Organic Molecules

Portions of this chapter are adapted with permission from B. Silcox, J. Zhang, S. Tung, I. Shkrob, L. Zhang, L. Thompson; manuscript submitted to ACS Materials Letters. Copyright unassigned

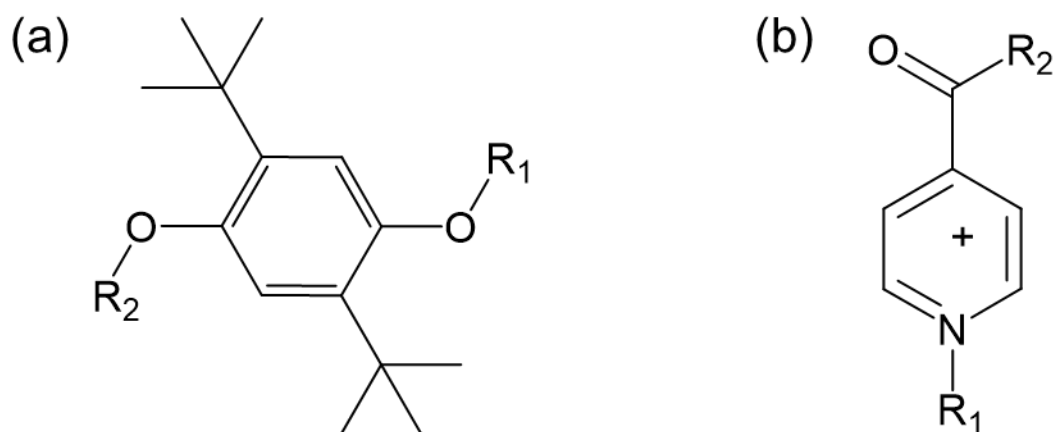
5.1 Background and Approach

Redox active organic molecules (ROMs) are a focus for active material development due to their low cost, high solubility, and high redox potentials in non-aqueous electrolytes.^{12,43,45,49} ROMs are conventionally divided into anolytes (negative charge carriers) and catholytes (positive charge carriers), with significant structural differences between the molecular families of each. Neutral molecules, stable radicals, and organic ions of either charge can serve as the parent molecules that become electrochemically charged. However, currently available ROMs lack the required long-term stability and cyclability to be used in practical devices.^{42,49,59,73,74,76,84}

Laboratory screening of active materials requires time consuming syntheses and exhaustive electrochemical characterization, limiting materials throughput. *In silico* screening of key active material properties such as redox potential, stability, and cyclability would streamline this process, but has proved difficult.^{48,53} The only generalized pre-synthetic prediction can be made for redox potential, which is linearly correlated to highest occupied/lowest unoccupied molecular orbital (HOMO/LUMO) energy calculated by density functional theory (DFT).⁵⁷ However, redox potential is one of the simplest properties to characterize, and greater benefit would be gained with correlations for stability and cyclability.

Two quantitative structure-property models were developed from active materials studies, one for pyridinium anolyte stability⁴⁸ and one for metal acetylacetonate cyclability.⁵³ While these models are useful within their individual molecular families, they are not generalizable to other ROM or metal coordination complex families. Given the labor of synthesis and characterization, all existing data sets within each active material family are relatively small (10-30 molecules). The small dataset size makes it challenging to learn robust, generalizable, models, where instead overfitting is favored, and high uncertainty arises.

Stability is the first property of interest for computational model building. While stability is not particularly relevant to cycling experiments, it governs the charge-storage retention of a redox flow battery (RFB). Of ROM families, only two have published stability data, the dialkoxyarenes discussed in this thesis and the pyridinium anolyte family.⁴⁸ Molecules from these two families form the data set used for model building in this chapter. The generalized structures for the dialkoxyarene catholytes and pyridinium anolytes used in this work are shown in Scheme 5.1.



Scheme 5.1 Structures for (a) dialkoxyarene catholytes and (b) pyridinium anolytes.

There are two types of models of particular use in ROM development, materials screening and property prediction. Materials screening focuses on identifying unviable materials and excluding them from further development, in this case electrochemically unstable active materials. These active materials are the first target for exclusion in the development pipeline to avoid wasted effort with their synthesis and characterization. Property prediction focuses on

accurately predicting properties of interest, in this chapter stability, and applying those models to candidate active materials for further validation.

In this chapter, I introduce 3 models to assist in ROM development for improved stability. A generalized model for screening electrochemically unstable active materials based on the dialkoxyarene and pyridinium families was developed with Sure Independence Screening and Sparsifying Operator (SISSO).⁸⁵ Two additional models for predicting dialkoxyarene stability were also developed with SISSO. In addition to establishing these models, this work is the first to use SISSO for prediction of experimental data on redox active molecules.

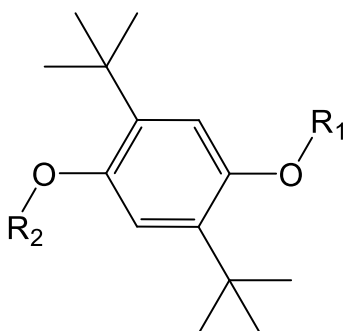
5.2 Experimental

5.2.1 ROMs

The dialkoxyarene catholyte and pyridinium anolyte families used in this chapter are the only ROM families with comprehensive published stability data. In total, 52 active materials were used in this chapter, although model development occurred with subsets of this data set when necessary. Of these 52 molecules, 33 were dialkoxyarene catholytes (23 stable molecules and 10 unstable molecules, 21 from ref. 76, nine from ref. 60, one from ref. 86,⁸⁶ and two introduced here). These molecules were split into Scheme 5.2 and Scheme 5.3 based on structure, and their names, functional groups, and stability (if measured) are presented in Tables 5.1 and 5.2 respectively. Stability data for the twenty-three stable DMBs is presented in refs. 8 and 10. 19 pyridinium anolytes (P1 to P18 from ref. 48 and unstable P19) are shown in Scheme 5.4 and their names, functional groups, and stability are presented in Table 5.3. The stability data for dialkoxyarenes was measured at room temperature in acetonitrile electrolytes, while the pyridinium stability data was measured at 70 °C in acetonitrile electrolytes. Unstable molecules were identified by electrochemical reversibility in cyclic voltammetry. The unstable species have a half-life in the charged state shorter than 1-10 s, which is the typical time for the potential sweep during the measurement of the redox current.

5.2.2 Density Functional Theory

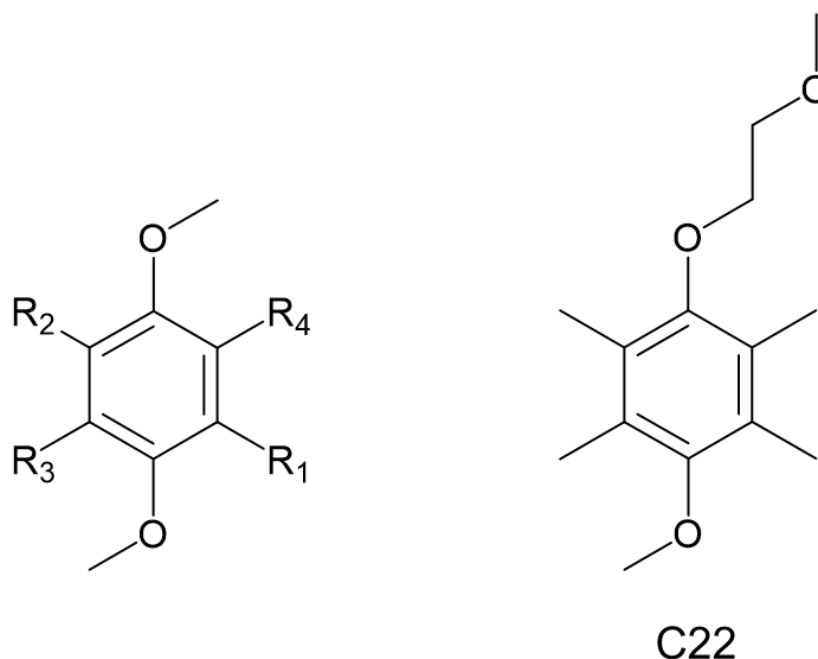
Density functional theory (DFT) was used to calculate descriptors for the investigated active materials. Calculations were performed using Gaussian 09 suite for the parent molecules and their charged states, both in the gas phase and in a solvation model based on density (SMD) model.⁸⁷ Molecular descriptors included orbital energies, dipole moments, ionization energies, and steric parameters. Sterimol parameters were calculated from optimized geometries in Sterimol.⁸⁸ Computing resources were provided by UM Advanced Research Computing.



Scheme 5.2 Structure for the dialkoxyarene catholytes in Table 5.1.

Table 5.1 Name, substituting groups, and experimentally measured half-lives of the Scheme 5.2 dialkoxyarenes.

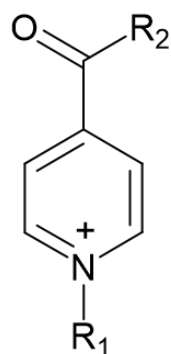
Molecule	Alternate Names	R ₁	R ₂	$t_{\frac{1}{2}}$
Q1	DDB, DiMe	Me	Me	26.5
Q2	MeEt	Me	Et	365.2
Q3	MeiPr	Me	<i>iso</i> -Pr	213.5
Q5	MeBn	Me	Bn	5.6
Q6	DiEt	Et	Et	208
Q7	DiiPr	<i>iso</i> -Pr	<i>iso</i> -Pr	312.9
Q9	DiBn	Bn	Bn	10.4
Q10	MesBu	Me	<i>sec</i> -Bu	19.2
Q11	DisBu	<i>sec</i> -Bu	<i>sec</i> -Bu	23.7
Q12	MePr	Me	<i>n</i> -Pr	86.3
Q13	DiPr	<i>n</i> -Pr	<i>n</i> -Pr	248.6
C1	DBBB, DiEO	C ₂ H ₄ OMe	C ₂ H ₄ OMe	26.1
C2	MeEO	Me	C ₂ H ₄ OMe	162.5
C3	Me(EO) ₂	Me	(C ₂ H ₄ O) ₂ Me	189.8
C4	Di(EO) ₂	(C ₂ H ₄ O) ₂ Me	(C ₂ H ₄ O) ₂ Me	13.6
F1	FMe	Me	CH ₂ CF ₃	13.3
F2	FEt	Me	CH ₂ C ₂ F ₅	197.4
F3	FBn	Me	CH ₂ C ₆ F ₅	71
F4	DiFMe	CH ₂ CF ₃	CH ₂ CF ₃	275.8
F5	DiFEt	CH ₂ C ₂ F ₅	CH ₂ C ₂ F ₅	106.6
F6	DiFBn	CH ₂ C ₆ F ₅	CH ₂ C ₆ F ₅	9.1
C23		OSO ₂ CF ₃	OSO ₂ CF ₃	Unstable



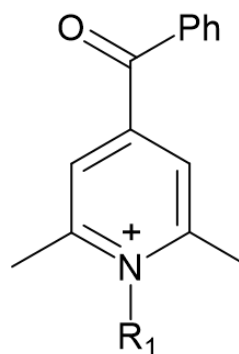
Scheme 5.3 Structures for the dialkoxyarenes catholytes in Table 5.2.

Table 5.2 Name, substituting groups, and experimentally measured half-lives of the Scheme 5.3 dialkoxyarenes.

Molecule	R ₁	R ₂	R ₃	R ₄	$t_{\frac{1}{2}}$
C7	Me	H	H	Me	15.3
C8	Me	Me	H	H	42.5
DMB	H	H	H	H	Unstable
JH0	Me	H	H	H	Unstable
JH3	Me	Me	Me	H	Unstable
JH4	Me	Me	Me	Me	Unstable
JH6	Me	H	Me	H	Unstable
JH7	NO ₂	H	H	H	Unstable
JH8	OAc	H	H	H	Unstable
C21	(iPr ₂)PO	F	(iPr ₂)PO	F	Unstable
C22	Me	Me	Me	Me	Unstable



P1-16, P19



P17, P18

Scheme 5.4 Structures for the pyridinium analytes in Table 5.3.

Table 5.3 Name, substituting groups, and experimentally measured half-lives of the Scheme 5.4 pyridiniums.

Molecule	R ₁	R ₂	$t_{\frac{1}{2}}$
P1	Me	Ph	1.47
P2	Me	<i>p</i> -C ₆ H ₅ OMe	1.06
P3	Me	<i>p</i> -C ₆ H ₅ Me	0.91
P4	Me	<i>p</i> -C ₆ H ₅ Cl	10.2
P5	Me	<i>o</i> -C ₆ H ₅ Me	3.38
P6	Me	Ph	41.98
P7	<i>p</i> -C ₆ H ₅ CF ₃	Ph	132.09
P8	Et	Ph	2.68
P9	<i>iso</i> -Pr	Ph	15.97
P10	<i>tert</i> -Bu	Ph	106.24
P11	Me	Me	1.47
P12	<i>tert</i> -Bu	Me	25.16
P13	Me	Mes	26.92
P14	<i>p</i> -C ₆ H ₅ OMe	Ph	31.73
P15	<i>o</i> -C ₆ H ₅ Me	Ph	392.92
P16	<i>o,o'</i> -C ₆ H ₄ Me ₂	Ph	1311.19
P17	Et	-	163.73
P18	Me	-	12.72
P19	Me	OMe	Unstable

5.2.3 Sure Independence Screening and Sparsifying Operator

SISSO is an algorithm that identifies low-dimensional a mathematical model for a property of interest, with a focus on being able to handle large, correlated feature spaces and sparse data sets. The limited number and size of ROM data sets and the complexity of stability and cyclability prediction make SISSO ideal for model building in this thesis. A full description of the SISSO algorithm and feature space construction can be found at ref. 85. SISSO constructs its feature space by applying mathematical operators recursively on the selected set of provided features while maintaining the dimensionality of the original descriptors. Basic arithmetic operations, the modulus, and the square root were used for all models in this chapter. A graphical representation of SISSO's construction of the feature space is shown in Figure 5.1.

$$\begin{aligned}\Phi_0 &\in \{x_1, x_2, y_1, \dots\} \\ \Phi_1 &\in \left\{ \begin{array}{l} x_1 + x_2, x_1 x_2 \\ x_1 y_1, x_1^2, \frac{x_1}{y_1} \\ \dots \end{array} \right\} \\ \Phi_2 &\in \left\{ \begin{array}{l} x_1(x_1 + x_2), x_1 y_1^2 \\ x_1 x_2 y_1, \frac{x_1 y_1}{x_2}, x_1^3 \\ \dots \end{array} \right\} \\ &\vdots\end{aligned}$$

Figure 5.1 SISSO construction of its feature space. Mathematical operators are recursively applied to the initial feature space, rapidly increasing the total number of descriptor combinations while maintaining dimensionality. For this example, x and y are variables with different dimensionality, limiting possible combinations.

With the feature space constructed, sure independence screening (SIS) is then performed to return the subset of the feature space that best correlates with the target property. With the new feature space subset, Sparsifying Operator (SO) finds the best n -dimensional model for the subset, if no model is found SIS and SO are run recursively to find subsequently higher dimension solutions.

SISSO can be used for classification or regression model development. For supervised classification, SISSO separates materials into one of two groups, uses the binary sort overlap to determine the optimal model. For supervised regression, SISSO uses goodness of fit for model selection. One of the models presented in this chapter used SISSO for classification, the other two were regression models. SISSO also has the flexibility to operate as single-task or multi-task learning, where materials are grouped and a model developed in parallel.⁸⁹ A full description of multi-task SISSO can be found at ref 85. Computing resources were provided by UM Advanced Research Computing.

5.3 Results and Discussion

5.3.1 A Binary Classifier for Generalized ROM Stability

In the development pipeline, many ROMs are designed, synthesized, and finally characterized by CV before they are identified as unstable. Targeting these unstable active materials presents the largest potential benefit in increasing the rate of viable ROM synthesis. While a screening model for a single ROM family would still be beneficial, a generalized model is ideal. A generalized model would have to be validated with stability data from a variety of ROM families, which is currently unavailable. However, a common model for even two active material families has not been developed.

All 52 ROM active materials in Tables 5.1 – 5.3 were used for this model, divided into “stable” and “unstable” categories by their measured stability. Single-task SISSO returned the model parameter ξ defined as

$$\xi = \frac{L\epsilon}{SE(SE + IE)^3}$$

Where L is the Sterimol length (across the ether oxygens for dialkoxyarenes and across the nitrogen and carbonyl carbon for the pyridiniums, in nm),⁸⁸ ϵ is the orbital energy for the highest

occupied (for a catholyte) or the lowest unoccupied (for an anolyte) Kohn-Sham molecular orbital (in Hartree), SE is the solvation energy, and IE is the ionization energy (both in Hartree, both of the uncharged molecule). ξ classified the 52 active materials with perfect accuracy and is shown in Figure 5.2.

The formula for ξ suggests a balance of several factors affecting stability. The numerator provides a positive correlation between higher redox potentials, greater steric effects, and chemical stability, in agreement with the pyridinium stability correlation.⁴⁸ For the dialkoxyarenes, this hinderance prevents the initial O-dealkylation reaction, while the pyridiniums are likely to experience π -merization with two pyridiniums face to face. The denominator suggests that lower solvation and ionization energies improve stability, and indicates the involvement of solvolysis, which is one of subsequent dialkoxyarene reactions after O-dealkylation.^{83,90} The presence of ionization energy on stability is unclear, as there are no established relationships between ionization energy and stability. Within the ROM families themselves, there is no correlation between ionization energy and stability. The presence of ionization energy may be a divider between the two ROM families, as the pyridinium anolytes have lower ionization energies than the dialkoxyarenes, which is reflected in ξ also dividing the stable ROMs.

5.3.1.2 Cross Validation

With any statistical model, validation is necessary to prove the robustness of the model as a predictive tool and to remove the possibility of SISO overfitting to the data set. Because ξ is a two-family model, validation is necessary to determine if ξ is describing a common molecular descriptor of stability or is just a statistical anomaly. To do so, the 52 molecules were partitioned into training and validation data sets, and SISO was then trained on the training set and its performance was validated on the validation set. This method, holdout validation, can be repeated with multiple random partitions of the initial data set in Monte Carlo cross validation (MC-CV). With SISO, this can result in a new term selected for each partition. If the MC-CV, on average, classifies the validation set with high accuracy and the new model, ξ' , is statistically

similar to ξ , then SISSO is identifying molecular factors affecting stability and has use as a predictive tool.

To determine the statistical similarity of ξ and ξ' , the Pearson correlation coefficient (PCC, ρ) between the two data sets was used

$$\rho_{\xi, \xi'} = \frac{n \sum \xi_i \xi'_i - \sum \xi_i \sum \xi'_i}{\sqrt{n \sum \xi_i^2 - (\sum \xi_i)^2} \sqrt{n \sum \xi'^2_i - (\sum \xi'^2_i)^2}} \quad (5.1)$$

where n is the sample size and ξ_i and ξ'_i are the individual sample points. If ξ and ξ' are identical, $\rho = 1$, if there is no correlation, $\rho = 0$, and if there is a perfect negative correlation $\rho = -1$.

The initial MC-CV for the model was performed with a 42/10 training/validation set split, maintaining the ratio of stable and unstable ROMs in each set (9/2 training/validation set split of unstable molecules). A histogram for 100 partitions is shown in Figure 5.3.

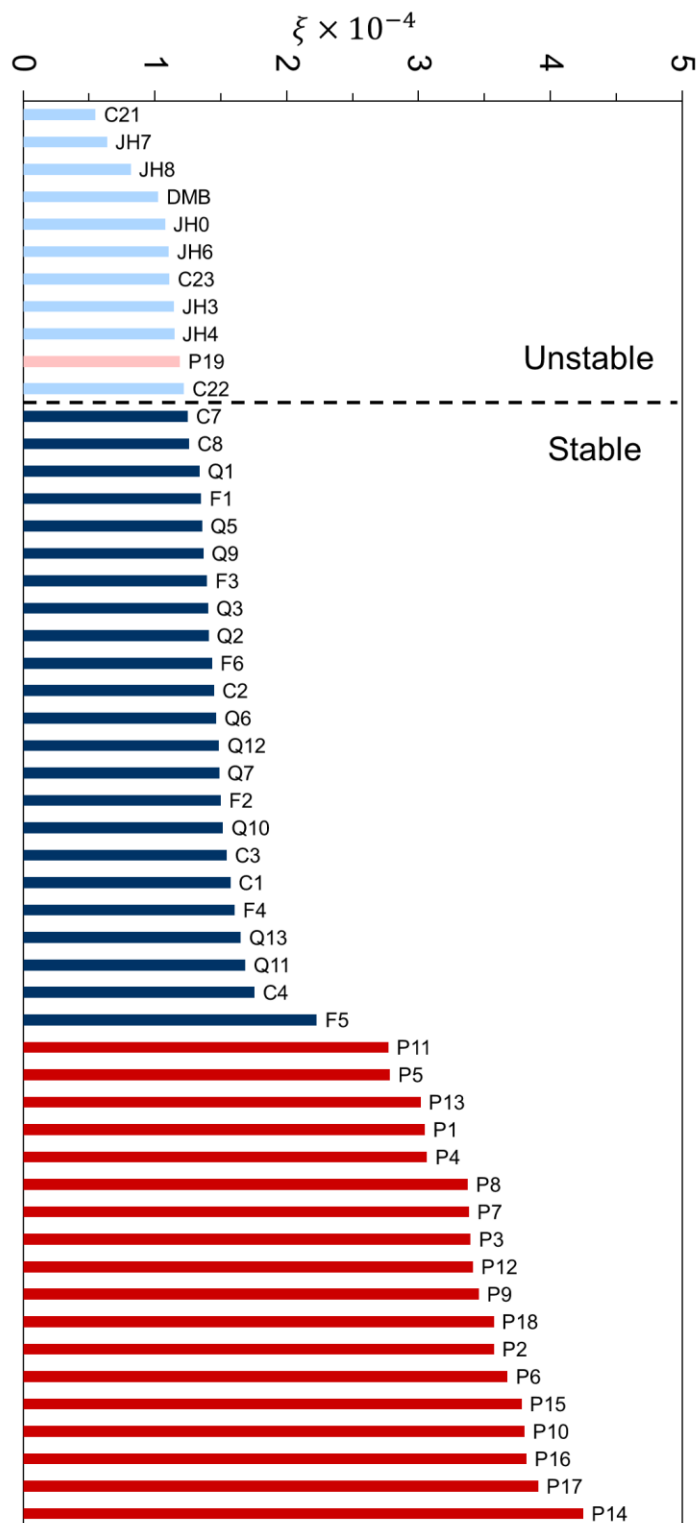


Figure 5.2 ξ classification of the 52 dialkoxyarene catholytes (blue) and pyridinium analytes (red) as unstable or stable above or below the dashed line respectively. Experimentally unstable molecules are given faded colors.

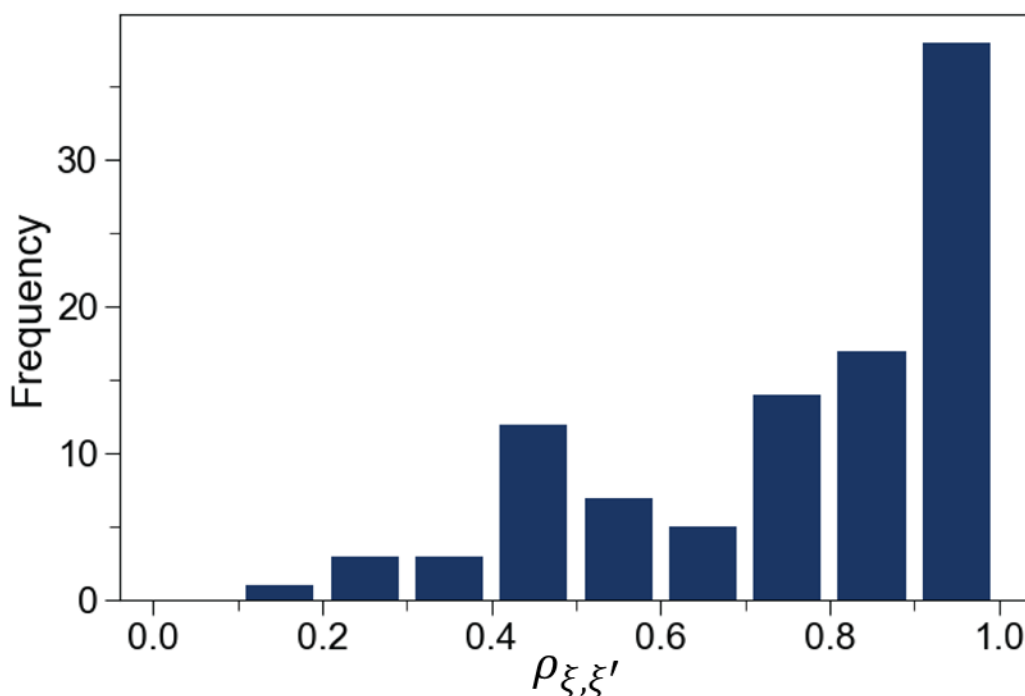
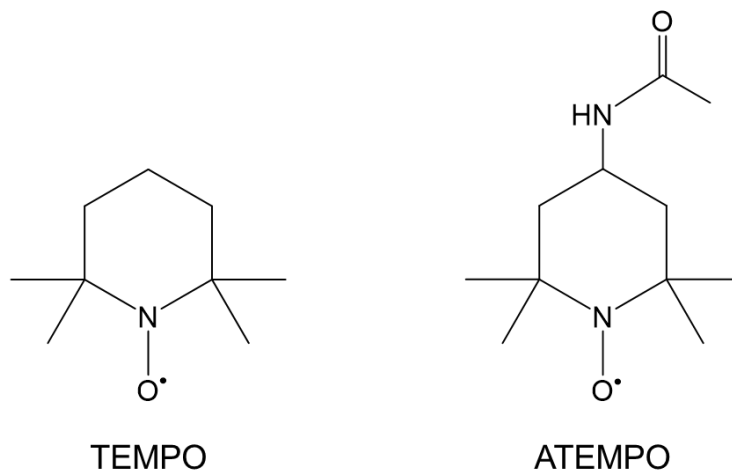


Figure 5.3 A histogram of 100 absolute PCCs of ξ and ξ' for the 42/10 MC-CV partitions. Clustering of the values near one indicates that the models identified by SISO do have chemical meaning for ROM stability.

Figure 5.3 shows most validation cases have ξ' close to ξ , with a sharp decrease in the number of models towards zero. This suggests that SISO is identifying an unobvious common feature of the two ROM families describing stability. The prediction accuracy for the validation sets in these 42/10 partitions averaged to 93%, confirming the use of ξ as a predictor. A second, larger, validation partition of 27/25 was made to further validate the accuracy of the model. Even with $\sim 50\%$ of the data in the validation set, the models identified in MC-CV had a 90% prediction accuracy. This further confirms the validity of ξ as a predictive and generalizable model for ROM stability screening.

5.3.1.3 TEMPO Family Prediction

While there are no other complete ROM families to validate ξ with, (2,2,6,6-tetramethylpiperidin-1-yl)oxyl (TEMPO) and 4-acetamido TEMPO (ATEMPO) shown in Scheme 5.5, are both stable radicals and stable by CV.



Scheme 5.5 Structures of TEMPO and ATEMPO. Both molecules are stable, electrochemically active radicals.

ξ can be further validated with TEMPO and ATEMPO, shown in Figure 5.4.

Both TEMPO and ATEMPO are classified by ξ as unstable despite their excellent experimental stability. While this result is disappointing, it is unsurprising as ξ was not trained on any TEMPO family catholytes. With TEMPO and ATEMPO added to the data set for a total of 54 molecules, SISSO ran to find an updated form of the model, returning ξ_{TEMPO}

$$\xi_{TEMPO} = \left(\frac{IE}{L} - \frac{SE}{B_1} \right) \frac{1}{IE + \epsilon}$$

Where B_1 is the Sterimol height out of the ring for all active materials. $\rho_{\xi, \xi_{TEMPO}} = -0.958$, and while ξ did not correctly classify TEMPO and ATEMPO, there is almost perfect negative correlation between ξ and ξ_{TEMPO} . This further supports the conclusion that SISSO is identifying an unobvious descriptor for electrochemical stability and that ξ is identifying a generalizable stability parameter.

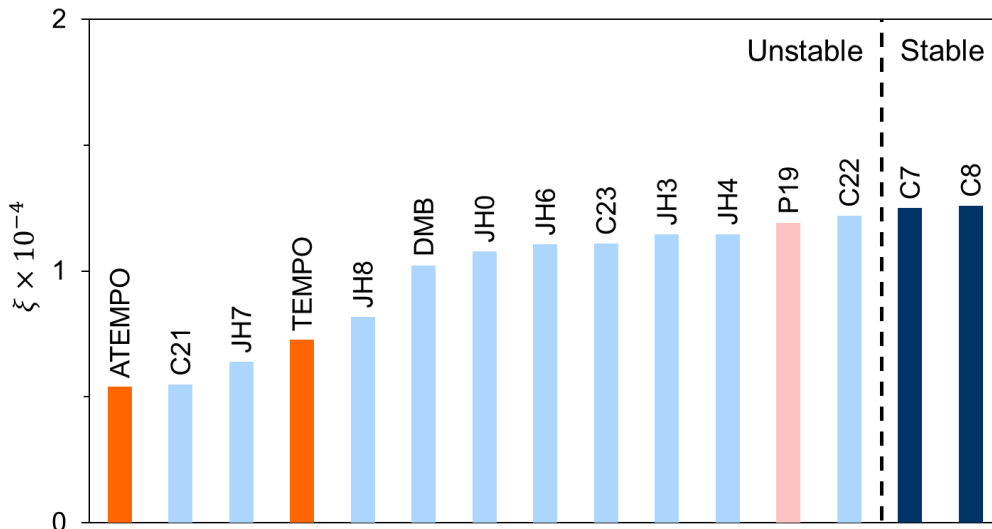


Figure 5.4 ξ classification of a selected group of dialkoxyarene catholytes (blue), pyridinium anolytes (red), and TEMPO family catholytes (orange) as unstable or stable above or below the dashed line respectively. Experimentally unstable molecules are given faded colors. Both TEMPO and ATEMPO are stable but are not classified properly by ξ .

5.3.2 Dialkoxyarene Stability Predictions

While screening for electrochemically unstable molecules led to the development of a fairly simple model, stability prediction is more difficult. The success and simplicity of the stability prediction for pyridinium anolytes seems to be an exception rather than the trend. This is surprising given the nature of dialkoxyarene cycling in alkylammonium salts, which had a strong correlation between steric hinderance and cycle life (N_{80}). In contrast, the dialkoxyarene half-lives show no correlation with any steric parameters. Q2, which is the most stable cation, is the second least sterically hindered dialkoxyarene in any of the three dimensions, while Q11, the longest cycling molecule from Chapter 2, has a cation half-life of less than 24 hours. As the stabilities of the dialkoxyarenes seem random, descriptive models are more difficult to find and more complex, with a greater possibility of overfitting.

Initial attempts to develop a stability model from the 23 stable dialkoxyarenes in Tables 5.1 and 5.2 were unsuccessful. Of the models that were developed with a reasonable R^2 value, none passed the simplest cross-validation case, leave-one-out cross-validation (LOOCV), implying that all the models were overfitted. LOOCV is a subset of leave-p-out cross validation, where a

subset p is removed from the original data set to be used as the validation set. LOOCV uses $p = 1$, which for 23 total samples is equivalent to removing $\sim 4\%$ of the training set.

Despite the lack of a robust model, the SISSO terms which correlate best to the target property, in this case $t_{\frac{1}{2}}$, can still provide insight into the most important descriptors. The best 1, 2, and 3-dimensional properties selected by SISSO (c_{1D} , c_{2D} , c_{3D}) were

$$c_{1D} = \frac{1}{SE_+}$$
$$c_{2D} = \frac{B_5}{SE_+^3}$$
$$c_{3D} = \frac{SE_+(SE_0 + SE_+)}{B_5}$$

Where SE is the solvation energy of the active species for the specified molecular charge (in Hartree) and B_5 is the Sterimol width (measured from the ether oxygen axis, in nm). The presence of these three terms suggest that width out of the benzene ring and solvation energy are the most important factors for dialkoxyarene stability. The presence of solvation in these terms and the classification model in Section 5.3.1 suggests that the solvation environment has a significant effect on the stability of dialkoxyarenes. This also has implications for cycling experiments, which have so far been almost exclusively performed in acetonitrile. Further investigation of the dialkoxyarenes in other non-aqueous solvents may be needed to optimize their electrolytes for stability. B_5 confirms the established hypothesis that steric hinderance is significant for maintaining ROM stability, but typically height of the ROM is more significant than width.⁴⁸

5.3.2.1 Stability Prediction of Hydrocarbon-Substituted Dialkoxyarenes

Overfitting of the dialkoxyarene predictions may be due to insufficient structural similarities in the 23-molecule training set. Removing even one structurally unique active material would then change the entire model. Selecting a narrower subset of the dialkoxyarenes does further reduce the size of the training set, but may prevent overfitting. The first subset selected were the molecules Q1 – Q13 in Table 5.1, the hydrocarbon-substituted structures. SISSO returned a fairly simple model for these structures

$$t_{\frac{1}{2}} = A \times \frac{1}{B_1 \times LUMO} + B \times \frac{\mu_0}{\mu_0 - \mu_+} + C \times \frac{\mu_+}{|LUMO - LUMO_S|} + D$$

Where B_1 is the Sterimol height (measured from the plane of the benzene ring, in nm), $LUMO$ is the lowest unoccupied Kohn-Sham molecular orbital (in Hartree), and μ is the absolute dipole moment for subscript molecular charge (in Debye). $A = -3.54$, $B = -218$, $C = -0.0223$, and $D = -101$. This formula for $t_{\frac{1}{2}}$ suggests that solvation energy does not play a significant role in the stability of these dialkoxyarenes, instead $LUMO$ and dipole moments are most important. While the significance of the LUMO is unknown, dipole moments are an indirect measure of both symmetry and size. From the presence of B_1 and the dipole moment, steric hinderance is a significant factor on the stability of the hydrocarbon-substituted dialkoxyarenes, matching observations from the general ROM screening model and pyridinium stability.⁴⁸ A parity plot for this model is shown in Figure 5.5.

Due to the limited size of the data set, LOOCV was used to assess the robustness of the model. Of the 11 cross validation cases, nine returned the same model, including the exclusion of Q2, the most stable molecule. The two LOOCV cases which did not cross-validate were exclusion of Q1 and Q5. Q5 is the least stable molecule and the inability to cross validate with the lowest 9% of the data removed is not surprising. Q1's inability to cross validate is not dependent on the exclusion of extreme data and must have structural significance. This inability to cross validate is likely due the lack of an asymmetric pair for Q1, as the base molecule for the dialkoxyarene family. Every other hydrocarbon-substituted dialkoxyarene is part of an asymmetric/symmetric pair, even if one is excluded in cross-validation, the other still provides necessary descriptors for SISSO to find the original model.

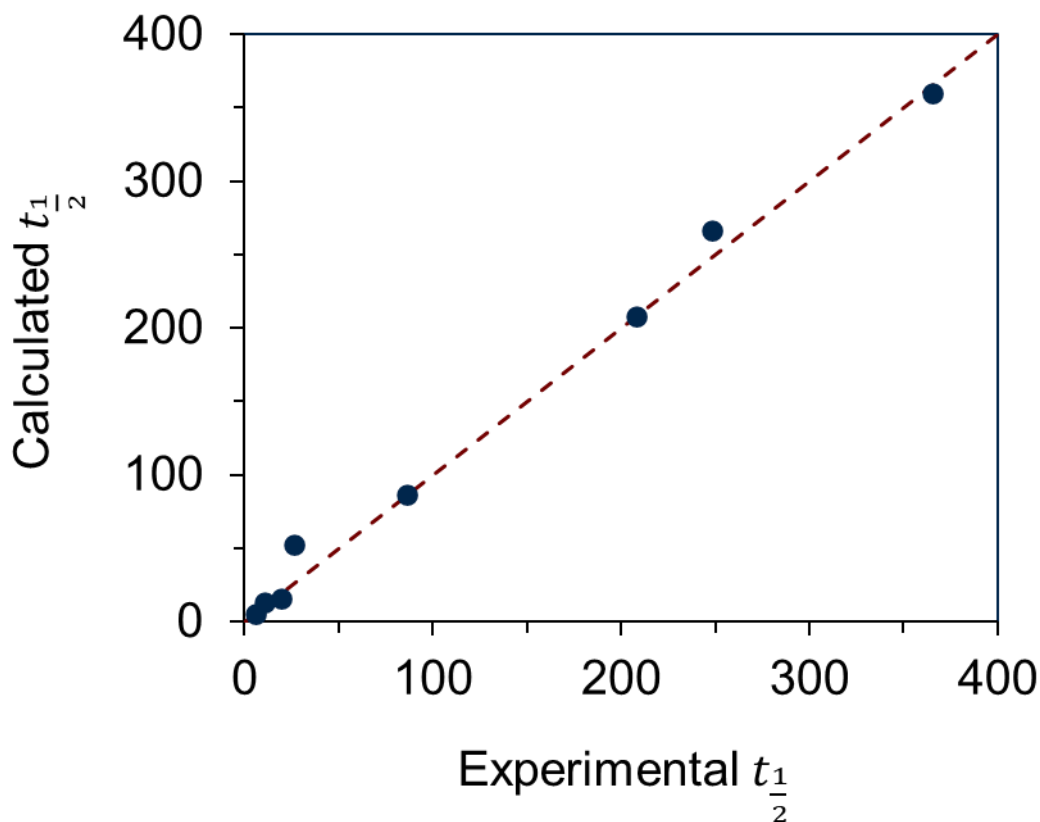


Figure 5.5 Parity plot of experimental and predicted $t_{1/2}$ of hydrocarbon substituted dialkoxyarene catholytes.

5.3.2.2 Multi-Task Stability Prediction of Dialkoxyarenes

The lack of similarity between the descriptors for dialkoxyarene stability and the hydrocarbon substituted dialkoxyarene stability suggests that a common stability model cannot be developed with the current data set. However, with the success of the hydrocarbon substituted dialkoxyarene model, multi-task SISSO modeling may be suitable. To enable multi-task learning, the 21 dialkoxyarenes in Table 5.1 were divided into three sub-families by substituting groups, hydrocarbons, poly-ethylene oxides (PEO), and fluorinated hydrocarbons. SISSO was tasked with finding shared stability descriptors for the three sub-families in parallel, the descriptors are given unique coefficients for each sub-family to complete the model. The general form of the model returned by SISSO is

$$t_{1/2} = A \times \frac{B_{1,short} + B_{1,long}}{2B_{1,short}B_{1,long}LUMO_S} + B \times \frac{LUMO}{L - 2B_5} + C \times \frac{\mu_+^3}{\langle R^2 \rangle^9} + D$$

Where $\langle R^2 \rangle$ is the electronic spatial extent of the neutral molecule (in 10^4 a.u.). Table 5.4 contains the active materials and coefficients for each sub-family of dialkoxyarenes.

Table 5.4 Molecules and coefficients for the three dialkoxyarene sub-families.

Sub-Family	Active Materials	<i>A</i>	<i>B</i>	<i>C</i>	<i>D</i>
Hydrocarbons	Q1 – Q13	-2.22	-1.66×10^4	-0.635	-139
PEO	C1 – C4	-35.2	1.64×10^5	0.307	-3770
Fluorinated	F1 – F6	-4.89	-170	-0.0121	-8.30

Molecular geometry plays a significant role in the model through Sterimol parameters and a term for the electronic spatial extent. Similar to the hydrocarbon-only model, LUMO energy and the dipole moment as a proxy for symmetry seem to be significant, although the physical meaning of the LUMO is still unknown. A parity plot for all three sub-families is shown in Figure 5.6.

Due to the limited size of the data set and the constraints of multi-task SISSO, which minimizes goodness of fit for each sub-task weighted equally, cross-validation was unsurprisingly unsuccessful. Even with LOOCV only excluding one active material, the size of each sub-family prevented SISSO from prediction. Because of this, the multi-task model reported cannot be claimed to be robust, but more active materials are needed for a well-supported conclusion.

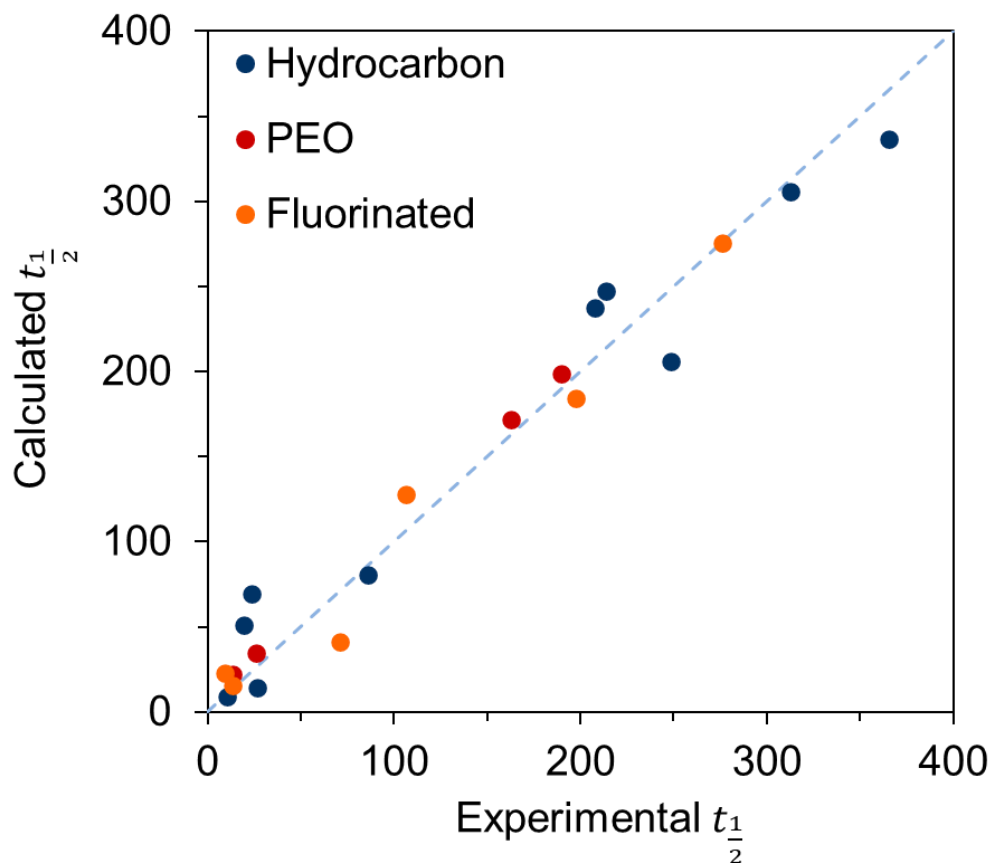


Figure 5.6 Parity plot of experimental and predicted $t_{1/2}$ of hydrocarbon substituted dialkoxyarene catholytes.

5.4 Conclusions

In this Chapter, SISO was used to find molecular descriptors for ROM stability. Three separate physics-based models were developed, a generalized ROM screening model, a predictive model for hydrocarbon-substituted dialkoxyarenes, and a predictive, multi-task model for dialkoxyarenes. The screening model allows researchers to screen unstable ROMs in the dialkoxyarene catholyte and pyridinium anolyte family. The two dialkoxyarene models are the first stability models developed for the dialkoxyarene family. All of the models developed showed the importance of steric properties on stability, although these varied by ROM family. For the dialkoxyarenes in particular, *LUMO* energy, sterimol height out of the benzene ring, and symmetry were the best individual descriptors for stability. Most importantly, this work

shows that there is commonality between stable and unstable molecules in the three ROM families investigated, as well as demonstrates how physics-based models can be constructed for ROMs with SISSO. Overall, this work introduces three models for design of stable active materials and identifies the molecular descriptors impacting ROM stability.

5.5 Acknowledgments

I would like to thank Prof. Shelley Minter for communicating the structure of P19.

Chapter 6

Cyclability predictions for Catholyte Redox Active Organic Molecules

6.1 Background and Approach

The most important characteristic for redox active organic molecules (ROMs) is their cyclability, or their ability to cycle reversibly over extended time frames. However, no ROM has been developed with the required cyclability to be used in beyond the laboratory scale.^{42,49,59,73,74,76,84} Developing new ROMs to meet cyclability targets requires time consuming syntheses and exhaustive electrochemical characterization, limiting materials throughput. Ideally, researchers would be able to use *in silico* screening of cyclability before synthesizing and characterizing ROMs.

Computational calculation of redox potentials and the estimation of redox potentials from highest occupied/lower unoccupied molecular orbital (HOMO/LUMO) energies is well established. Reasonable stability predictions exist for the pyridinium anolyte family and a generalized ROM prediction in Chapter 5 of this thesis.⁴⁸ For cyclability, only one model exists, which encompasses a subset of metal acetylacetonates.⁵³ This model related the cycle life (N_{80}) of metal acetylacetonates to the HOMO orbital density on the metal center, shown in Figure 6.1.

The same limitations for developing stability predictions, such as difficulties taking experimental data, small data sets, and a small number of data sets, are amplified for cyclability. Only one complete set of ROM N_{80} data has been published,⁷⁶ with most papers only reporting their best results. In addition, many of the reported results intentionally avoid showing material decay, providing only an artificial lower bound on N_{80} . These limitations are compounded by the complexities and limitations of bulk electrolysis (BE) experiments discussed in Chapter 3. While stability is a relatively controlled measurement, cyclability introduces interactions between the

active material and the electrodes, electrolyte, and separators, among others. Differences in experimental conditions and supporting salt choices can make comparing literature experiments pointless with no understanding of these effects on their N_{80} . These limitations further decrease the amount of data available, making cyclability modeling more challenging.

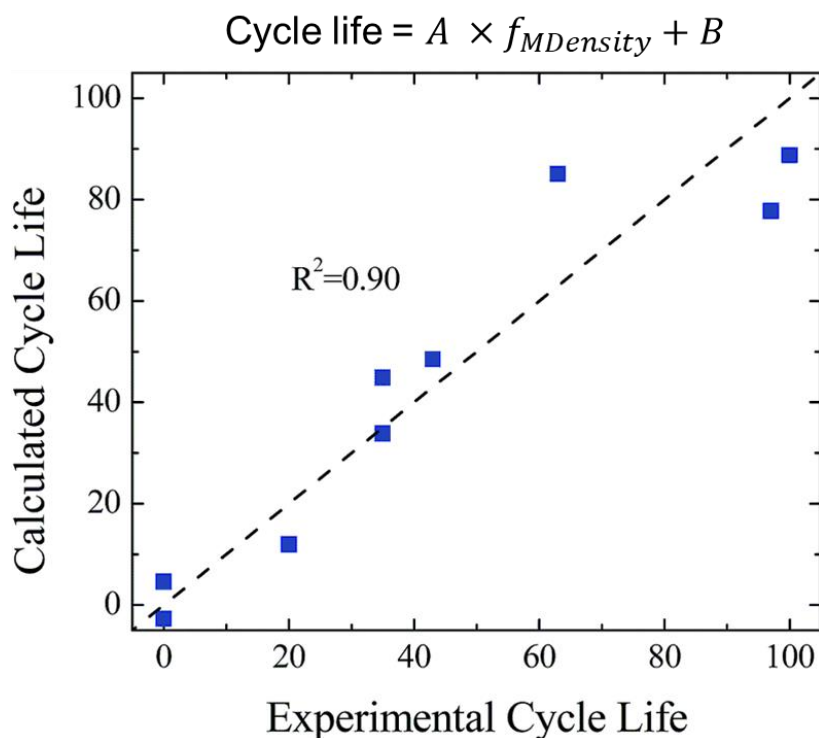


Figure 6.1 Parity plot of experimental and predicted cycle life of metal acetylacetonates with more than 50% of their HOMO orbital density on the metal.⁵³

The N_{80} data used in this chapter are the BE cells which have been previously discussed in Chapters 2-4, the suite of dialkoxyarene active materials and (2,2,6,6-Tetramethylpiperidin-1-yl)oxyl (TEMPO). Cyclability modeling is less concerned with screening and more concerned with prediction, as most electrochemically reversible molecules cycle to some degree and the range of N_{80} for ROMs is not large enough to dismiss molecules under a specific cutoff.

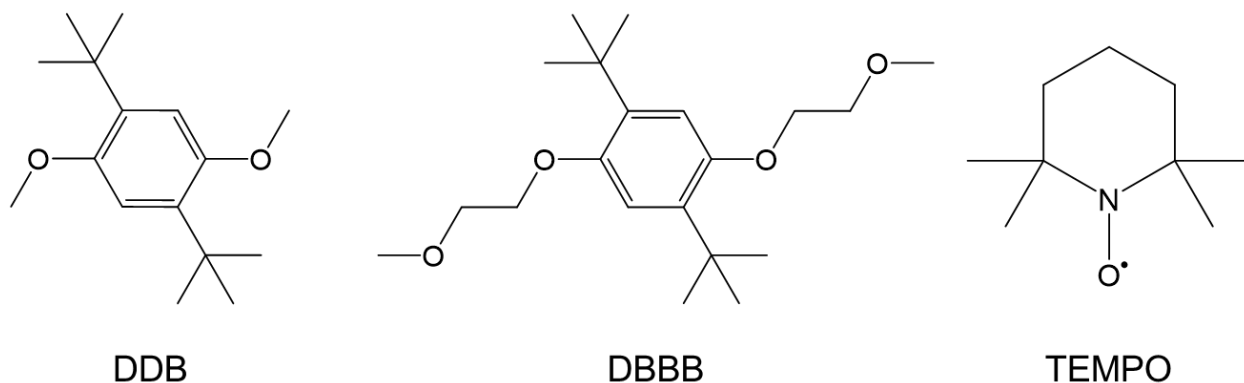
In this chapter, I introduce nine models for dialkoxyarene N_{80} developed with Sure Independence Screening and Sparsifying Operator (SISSO). The first two are simple models for

dialkoxyarene cycling in TBAPF₆ and LiTFSi based on the insights gained in Chapter 2 for improving N_{80} . The remainder were developed from the cycling matrix data in Chapter 3.

6.2 Experimental

6.2.1 ROMs

Due to the limitations of cyclability data from literature sources, all N_{80} data used in this chapter was taken from the BE experiments in Chapters 2 and 3. Chapter 2 data consisted of nine dialkoxyarene catholytes cycled at 5 mM active material, 1 C rate, with 500 mM TBAPF₆ in acetonitrile (MeCN). The names, structures, and N_{80} of these dialkoxyarenes, reproduced from Table 2.2 are shown in Table 6.1. Chapter 3 data consisted of the BE cycling matrix for 1,4-Di-tert-Butyl-2,5-dimethoxybenzene (Q1, DDB), 2,5-Di-tert-butyl-1,4-bis(2-methoxyethoxy)benzene (DBBB), and TEMPO at a variety of active material concentrations, cycle rates, and with 6 different supporting salts. Structures for DDB, DBBB, and TEMPO are shown in Scheme 6.1, reproduced from Scheme 3.1



Scheme 6.1 Structures of DDB, DBBB, and TEMPO.

N_{80} data for the cycling matrix can be found in Tables 3.2 – 3.4. Additional N_{80} data for DBBB and the three liquid dialkoxyarenes, shown in Table 6.2 with their names, structures, and N_{80} , were used as a validation set for the simple dialkoxyarene model.

Table 6.1 Names, structures, and cycle lives from BE experiments of the dialkoxyarene catholytes originally presented in Chapter 2. Cells were cycled at 5 mM active material, 1 C cycle rate, in TBAPF6/MeCN.

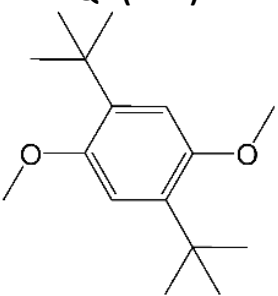
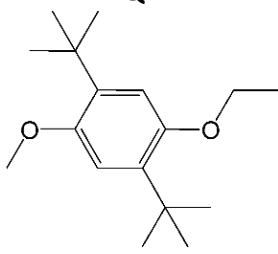
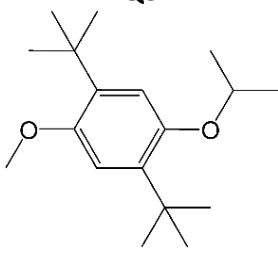
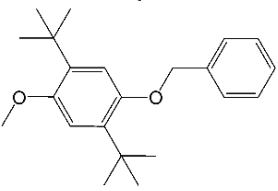
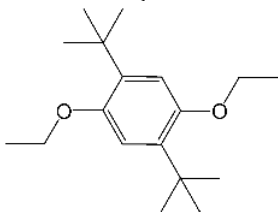
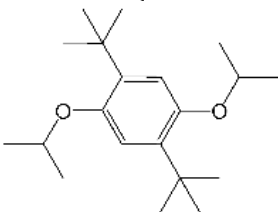
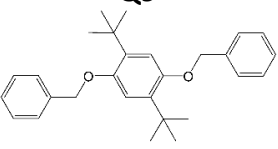
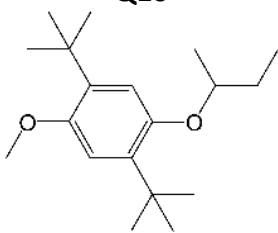
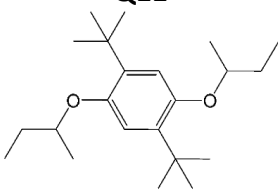
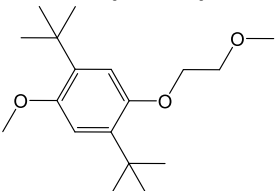
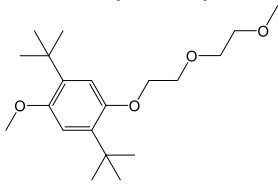
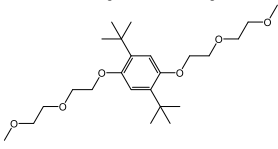
Molecule Structure	Q1 (DDB) 	Q2 	Q3 
\bar{N}_{80}	68	60	50
Molecule Structure	Q5 	Q6 	Q7 
\bar{N}_{80}	29	53	73
Molecule Structure	Q9 	Q10 	Q11 
\bar{N}_{80}	18	55	127

Table 6.2 Names, structures, and cycle lives from BE experiments of the liquid dialkoxyarene catholytes.

Molecule Structure	C2 (ANL-8) 	C3 (ANL-9) 	C4 (ANL-10) 
N_{80}	51	51	59

6.2.2 Density Functional Theory

Density functional theory (DFT) was used to calculate descriptors for the investigated active materials. Calculations were performed using Gaussian 09 suite for the parent molecules and their charged states (using B3LYP/6-31g(d), both in the gas phase and in a solvation model based on density (SMD) model.⁸⁷ Molecular descriptors for SISSO included orbital energies, dipole moments, ionization energies, and steric parameters. Sterimol parameters were calculated from optimized geometries in Sterimol.⁸⁸ Computing resources were provided by UM Advanced Research Computing.

6.2.3 Sure Independence Screening and Sparsifying Operator

SISSO quantitative single and multi-task were used to construct the 9 models presented in this chapter. The SISSO feature space was constructed with basic arithmetic operations, the modulus, and the square root. SISSO selected models from the identified feature space with the least squared error. Computing resources were provided by UM Advanced Research Computing.

6.3 Results and Discussion

6.3.1 A Simple Model for Dialkoxyarene N_{80} with a TBAPF₆/MeCN Electrolyte

Chapter 2 introduced a new set of dialkoxyarene catholytes, characterized them with BE, and identified the descriptors which correlated to N_{80} . As a model for dialkoxyarene cyclability has yet to be developed, this data set provides an opportunity to do so. Ideally, this model would not be limited to a single supporting salt and include more than 9 data points, but reliable, transferable N_{80} data does not exist.

The nine dialkoxyarene molecules in Table 6.1 were used for this model. Single-task SISSO returned the model

$$N_{80} = A \times \frac{B_{1,short}}{SE} + B \times \frac{B_{1,long}}{\mu_0} + C$$

where B_1 is the sterimol height out of the benzene ring for the long and short functional groups (in Å). If the dialkoxyarene was symmetric, these values are identical. SE is the solvation energy of the neutral molecule (in Hartree) and μ is the absolute dipole moment at the specified charge

(in Debye) in the SMD solvent model (MeCN). $A = -0.788$, $B = -0.00199$, and $C = -30.1$. A parity plot of predicted N_{80} vs experimental N_{80} is shown in Figure 6.2 with the maximum absolute error (MAE) inset.

The formula for N_{80} suggests steric factors are the most significant component, confirming the hypothesis from Chapter 2. The separation of the steric parameters of the two functional groups and the presence of the dipole moment both suggest that symmetry is also significant. The data from Table 6.1 shows that Q7 and Q11, the more cyclable molecules, are both symmetric and out-cycle their asymmetric counterparts. Revisiting the reaction in Scheme 2.3, O-dealkylation can occur on either methoxy group, which necessitates a sterically hindered functional group on each. Similar to the model for general ROM screening, SE is significant, possibly due to the solvolysis reaction that occurs after O-dealkylation.

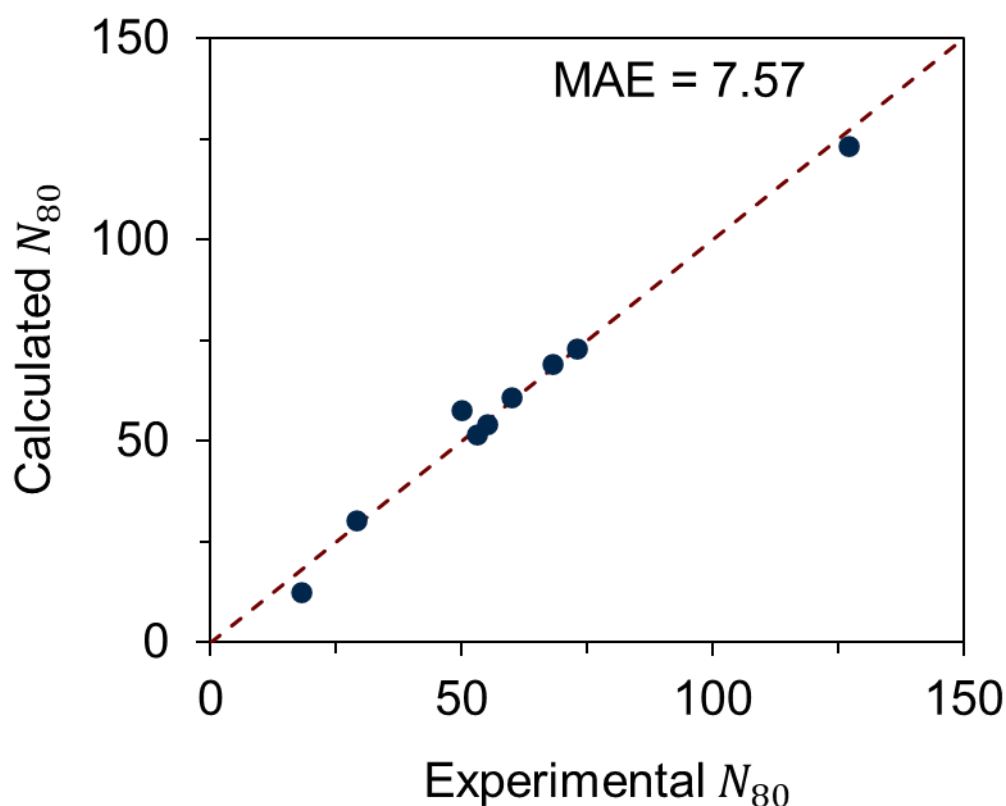


Figure 6.2 Parity plot of experimental and SISSO predicted cycle life of dialkoxyarene catholytes cycled in a TBAPF₆/MeCN electrolyte at 5 mM active material concentration and 1 C rate.

6.3.1.1 Cross Validation

Due to the very limited size of the data set, the only reasonable cross-validation strategy is leave-one-out (LOOCV), partitions the data set into a validation set of size one and a training set with the remainder of the data. Due to the nature of the data set used for this model development, cross-validation is not expected to be perfect. Q11 is almost an outlier in the data, and most of the data is clumped around $N_{80} = 60$. Of the nine LOOCV cases, six returned the same model and seven correctly predicted the validation set. The two cases where predictions failed were with Q7 and Q11 excluded. These two molecules are symmetric and the most sterically hindered of the dialkoxyarenes and correspondingly have the second highest and highest N_{80} respectively. However, the models returned by SISO in these cross-validation cases were highly similar to the original, maintaining the presence of B_1 and SE . The LOOCV case which did not return the exact same model but still was predictive had Q1 removed from the training set. Similar to the model for hydrocarbon stability, Q1 will not cross-validate, most likely due to the lack of an asymmetric pair molecule.

6.3.1.2 Liquid Dialkoxyarene Validation

With a seemingly robust model for the dialkoxyarenes in Table 6.1, an attempt was made to validate it with four additional experiments for poly-ethylene oxide (PEO) substituted dialkoxyarenes, DBBB, C2, C3, and C4. Unfortunately, the model underpredicts N_{80} by an average of 24, or 45% for these four molecules due to their increased solubilities (and consequently greater solvation energies). Adding these molecules to the training set introduced much greater complexity into the SISO selected model, indicative of a separate descriptor for their N_{80} that SISO could not reconcile.

6.3.1.3 The Simple Model for a LiTFSi/MeCN Electrolyte

With the success of the simple model for the TBAPF₆/MeCN electrolyte, an attempt was made to identify a model for the same active materials in a LiTFSi/MeCN electrolyte using the

data taken at Argonne National Laboratory (ANL) in Figure 2.8. Single-task SISO identified a similarly complex model

$$N_{80} = A \times \frac{SE_+}{SE} + B \times \frac{\mu_+}{LUMO_s} + C$$

Where SE_+ is the solvation energy of the cation active material (in Hartree) and $LUMO_s$ is the lowest unoccupied Kohn-Sahm molecular orbital energy in the SMD solvent environment (in Hartree). $A = 131$, $B = 0.428$, and $C = -362$. A parity plot for this model is shown in Figure 6.3. In addition to a greater root-mean-square error than the TBAPF₆/MeCN model, this LiTFSi/MeCN model did not cross-validate with LOOCV, likely due to the inability of the descriptors to adequately capture Li⁺ coordination effects. While this model is of no particular robustness, it confirms the most significant descriptors for predicting dialkoxyarene cyclability. Even without a predictive model, these descriptors can be used as guidelines for developing more cyclable dialkoxyarenes.

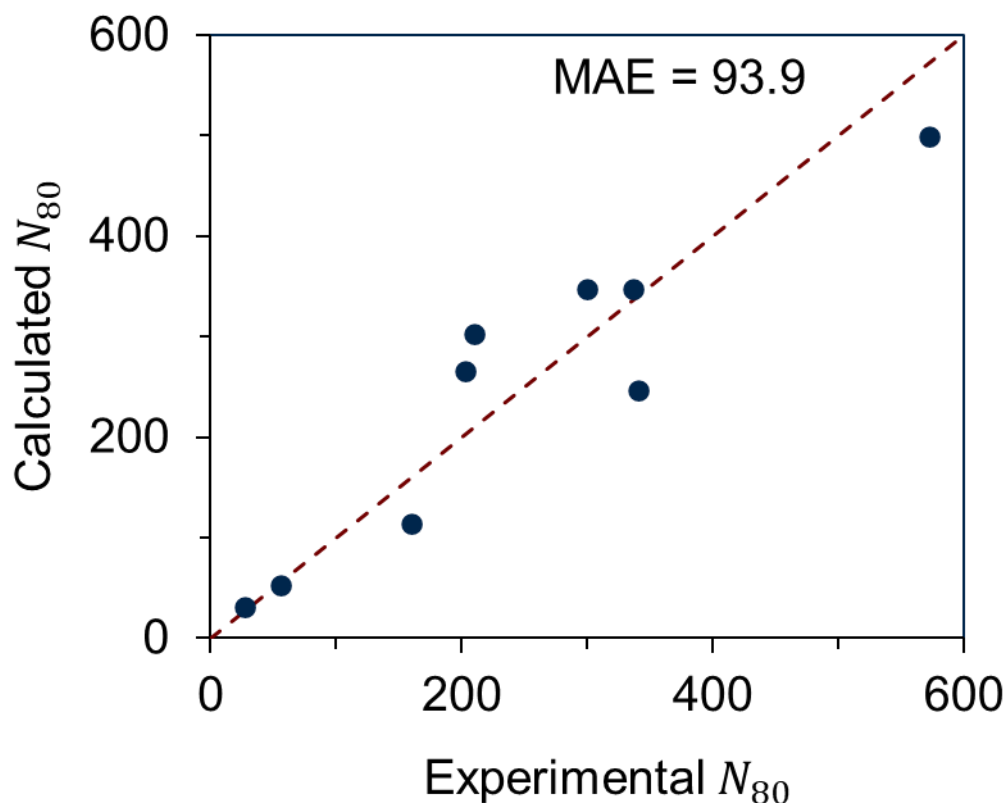


Figure 6.3 Parity plot of experimental and predicted cycle life of dialkoxyarene catholytes cycled in a LiTFSi/MeCN electrolyte at 20 mM active material concentration and 3 C rate.

6.3.2 Cyclability Models for Varied Experimental Conditions and Supporting Salts

Chapter 3 performed a thorough investigation of active material concentration, cycle rate, and supporting salt choice in BE experiments. As trends for N_{80} could not be observed, developing models with SISSO provides a second opportunity to identify trends in this data. Alternatively, this attempt may prove futile, as supporting salt effects dominated the BE experiments. Due to the multi-variate nature of the data set, the 66-element data set from Tables 3.2 – 3.4 was partitioned along active materials, supporting salts, and experimental conditions to form training sets. Due to the supporting salt interactions, six additional supporting salt descriptors were added to the descriptor set from a literature review of refs. 15-17.^{32,33,91} Only descriptors which were measured for all six of the investigated supporting salts could be used, of which only six were found. The limited number of descriptors means that differences between supporting salts signaled by these descriptors may be the result of unknown factors that are not in the descriptor set. Therefore, the presence of these descriptors in the models presented in this chapter may not have physical meaning. These descriptors were ionic radii, limiting molar conductivities, the transfer activity coefficient of the positive supporting salt ion from water to MeCN, and the standard Gibbs energy of transfer of the positive supporting ion from water to MeCN.

6.3.2.1 General Models for Catholyte ROM Cyclability

Similar to the screening model for stability developed in Chapter 5, a general model for cyclability would be the ideal tool for assisting molecular design efforts. With the data from Chapter 3, this model would hypothetically be able to predict cyclability for a given active material at specific experimental conditions. However, due to its complexity, it is difficult to even develop trends for the data presented in Chapter 3. The numerous active material-supporting salt interactions and dialkoxyarene cells which terminated early are likely introducing enough variance into the data to obscure any trend that may exist. SISSO was unable to identify a general model form for N_{80} . However, the best correlating terms to N_{80} still provide some insight into the most important descriptors. The best 1, 2, and 3-dimensional properties selected by single-task SISSO (c_{1D} , c_{2D} , c_{3D}) were

$$c_{1D} = \frac{L}{r_+}$$

$$c_{2D} = \frac{L}{r_+ C}$$

$$c_{3D} = \frac{C \text{ Rate}}{r_+ C \times LUMO}$$

Where L is the sterimol length across either the ether oxygen axis for dialkoxyarenes or through the oxygen and 4-position for TEMPO (in Å), r_+ is the ionic radius of the supporting salt cation (in nm), C is the active material concentration, $C \text{ rate}$ is the experimental cycle rate, and $LUMO$ is the lowest unoccupied Kohn-Sahm molecular orbital energy (in Hartree). From these three terms, it is apparent that supporting salt choice is as impactful as active material selection, while active material concentration and cycle rate are also significant. This confirms that supporting salt choice is the most impactful variation of those tested in Chapter 3, although all are significant. The benefit of Li^+ coordination is also reflected in these terms through the ionic radius of the supporting salt cation, which is an order of magnitude lower for Li^+ than for the alkylammoniums.

For multi-task learning, the data was partitioned three separate ways, by active material, by salt, and by experimental condition. SISSO was once again unable to identify a common model for any partition of the data. SISSO's selected best descriptors for each partition were also dominated by terms containing L , r_+ , $LUMO$, C , and $C \text{ rate}$, confirming the significance of these terms on N_{80} , but no overall relationship.

6.3.2.2 Models at Individual Experimental Conditions

With the difficulty developing a general model for N_{80} , further partitioning of the data set by individual experimental conditions was needed. These partitions would both reduce the number of terms in the data set and eliminate the presence of concentration and cycle rate from the model. With these partitions, models for the 20 mM active material, 1 C and 3 C rate models was identified. It is likely that the reduced impact of active material-supporting salt interactions at the higher active material concentration benefited model development. The SISSO identified model for the 20 mM active material, 1 C rate experiments is

$$N_{80} = A \times \frac{\gamma_{+,MeCN}}{r_+ r_- (LUMO + LUMO_S)} + B \times \frac{\gamma_{+,MeCN}}{\frac{B_1}{r_+} - \frac{L}{r_-}} + C \times \frac{\gamma_{+,MeCN}}{\Lambda_{\circ-} (HOMO_S - LUMO_S) - \Lambda_{\circ+} IE_S} + D$$

Where $\gamma_{+,MeCN}$ is the log of the transfer activity coefficient of the positive supporting salt ion from water to MeCN, r_- is the ionic radius of the supporting salt cation (in nm), B_1 is the Sterimol height out of the benzene ring for the dialkoxyarenes and through the oxygen and 4-position for TEMPO (in Å), Λ_{\circ} is the limiting ionic molar conductivity for the specified supporting salt ion (in S m² mol⁻¹), $HOMO_S$ is the highest occupied Kohn-Sahm molecular orbital energy in the SMD solvent environment (in Hartree), and IE_S is the ionization energy of the neutral active material in the SMD solvent environment (in Hartree). $A = -0.0227$, $B = -37.5$, $C = -28.7$, $D = 143$. Due to the increased complexity of this model, less can be gleaned from the descriptors than from the simple models.

The presence of a significant number of supporting salt terms are likely due to the impact of Li⁺ coordination, which SISSO is modeling by the differences in supporting salt cation descriptors, with supporting salt anion descriptors to further differentiate the experimental data. Of the active material descriptors used in the model, the LUMO energy once again appears to be the most significant factor along with Sterimol properties. Due to the limitations of the data, this model represents a prediction for the lowest bound of N_{80} , which can introduce some error for cross validation. A parity plot for this model is shown in Figure 6.4.

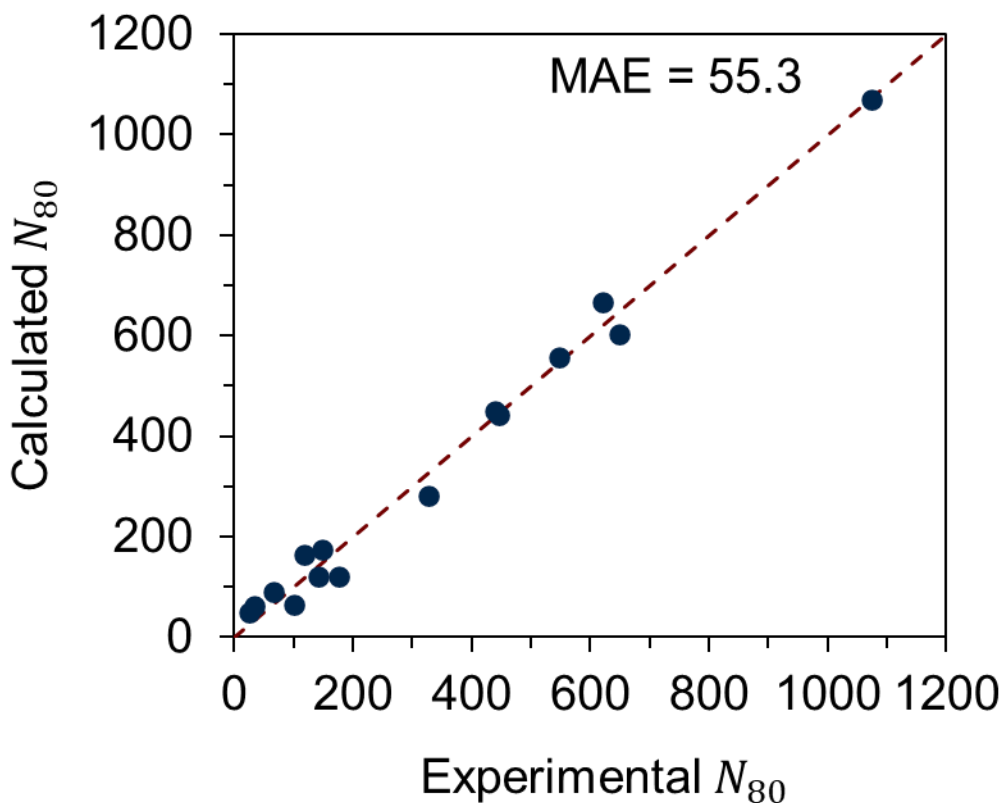


Figure 6.4 Parity plot of experimental and predicted cycle life of DDB, DBBB, and TEMPO cycled at 20 mM active material concentration and 1 C rate.

LOOCV of this model returned mixed results, with 8 out of the 15 possible validation cases succeeding. This is unsurprising with experiments that measure lower bounds and the unique active material-supporting salt interactions. Even with non-ideal cross-validation, this model still has use as the first predictor for cyclability at experimental conditions of 20 mM and 1 C.

The SISO identified model for the 20 mM active material, 3 C rate experiments was more complex than those previously reported in this chapter

$$N_{80} = A \times \frac{r_-^4}{\frac{r_-}{SE} - \frac{r_+}{LUMO_S}} + B \times \left| \frac{\Lambda_{o+}}{SE + LUMO_S} - \frac{\Lambda_{o-} - \Lambda_{o+}}{SE - LUMO} \right| + C \times (r_- \Lambda_{o-}^2 + \Lambda_{o+} |r_- - r_+|) + D$$

Where $A = -34800$, $B = -0.0643$, $C = 0.326$, $D = -872$. With the increasing complexity of the individual terms identified by SISO, the individual descriptors in the model become less meaningful and overfitting becomes more likely. However, it appears that SISO identifies

supporting salt ionic radii and limiting molar conductivity as the best descriptors to differentiate the six supporting salts. Similarly, the LUMO energy appears for the fourth time in the models, the most important active material descriptor for N_{80} , although the reason behind its significance is still unclear. A parity plot for the 20 mM 3 C model is shown in Figure 6.5.

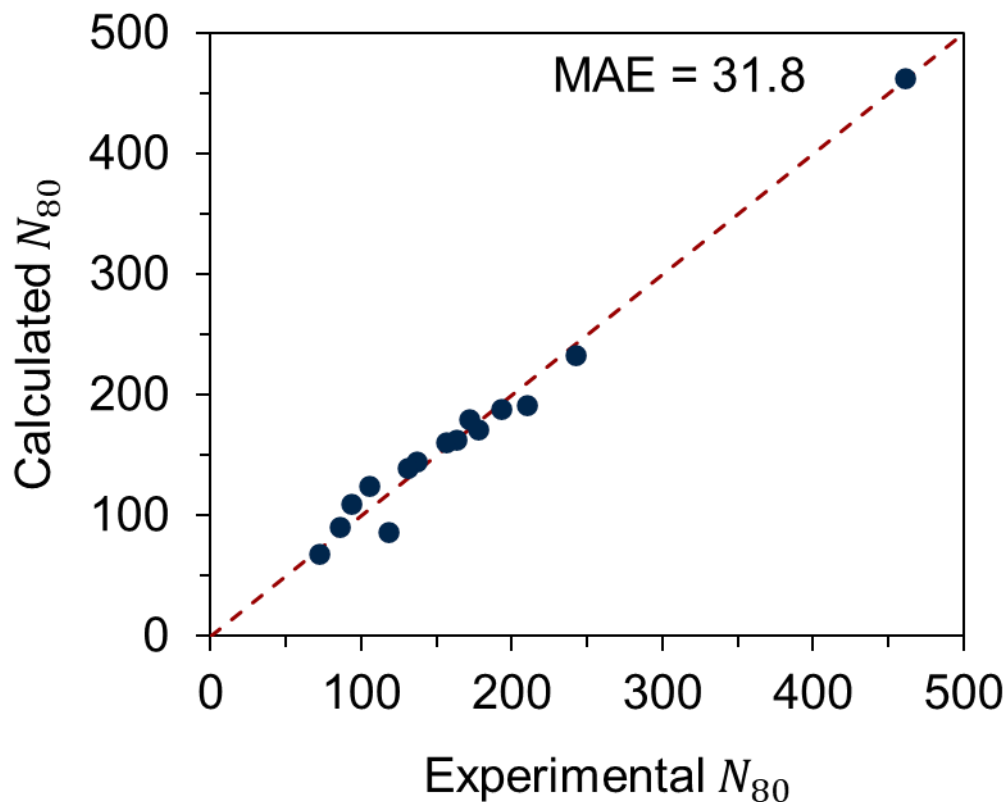


Figure 6.5 Parity plot of experimental and predicted cycle life of DDB, DBBB, and TEMPO cycled at 20 mM active material concentration and 3 C rate.

LOOCV of the 20 mM 3 C model returned a similar result to the 20 mM 1 C model, with 8 out of 15 possible validation cases succeeding. Notably, LOOCV failed for all DBBB data points and succeeded for all TEMPO data points, suggesting that further partitioning of the data set by active material would lead to simpler and more robust models. With this restriction, developed models are no longer general models for ROM cyclability and more data is needed to assist the development of a general ROM model.

6.3.3 Models for Individual Active Materials and Experimental Conditions

Partitioning the training set for an individual active material and experimental condition combination reduces the number of data points in each training set to six. With these limited training sets, the complexity of models is greatly reduced but the potential for overfitting is greatly increased. The presence of Li⁺ coordination to the dialkoxyarenes also reduces some training sets to two clusters of three points each, which is trivial to fit. Additionally, the limited number of descriptors for supporting salts means SISO is restricted to identifying relationships from a sparse data set. Insights from the SISO selected descriptor are therefore selected for necessity not physical meaning. The models reported in this section are models which passed LOOCV, and to remain properly fitted models, all have only one SISO identified descriptor. No properly fitted models were identified for DDB due to the reduced number of experiments performed at 20 mM active material concentration and the BF₄⁻ impurity effect.

6.3.3.1 DBBB

Only one robust model was identified for DBBB, at the 20 mM active material 1 C rate experimental condition.

$$N_{80} = A(r_+ + r_-) + B$$

Where $A = -1660$ and $B = 1120$. All six LOOCV cases succeeded, reporting the same model as the training set. Once again, this model is only predictive for the lower bound of these experiments due to premature cell termination. However, it does suggest that supporting salts with lower ionic radii are ideal for maximizing the N_{80} of DBBB at these experimental conditions. A parity plot for this model is shown in Figure 6.6.

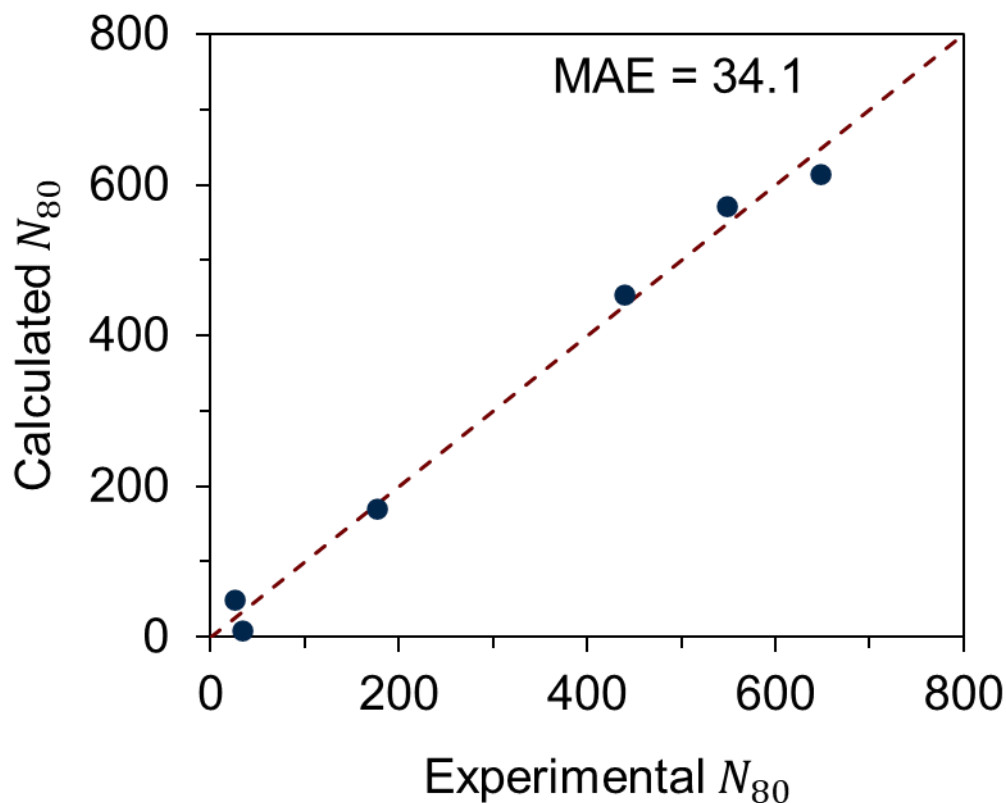


Figure 6.6 Parity plot of experimental and predicted cycle life of DBBB cycled at 20 mM active material concentration and 1 C rate.

6.3.3.2 TEMPO

TEMPO was the easiest of the three active materials to model, with a robust model developed for each of the four experimental conditions. This is likely due to the reduced impact of the BF_4^- impurity on TEMPO cycling experiments. Notably, TEMPO LOOCV was most likely to fail when LiPF_6 was removed from the training set, as the descriptor set with SISSO cannot account for active material-supporting salt interactions, which are strongest in the TEMPO- LiPF_6 experiments. The SISSO identified model for the 5 mM active material 1 C rate experiments is

$$N_{80} = A \frac{L}{\Lambda_{\sigma^-}} + B$$

Where $A = 10300$ and $B = -505$. As TEMPO is the only active material in the training set, L is a constant and SISSO identifies the supporting salt anion as the only significant factor for N_{80} . A parity plot with the LiPF_6 and LiBF_4 data points highlighted is shown in Figure 6.7.

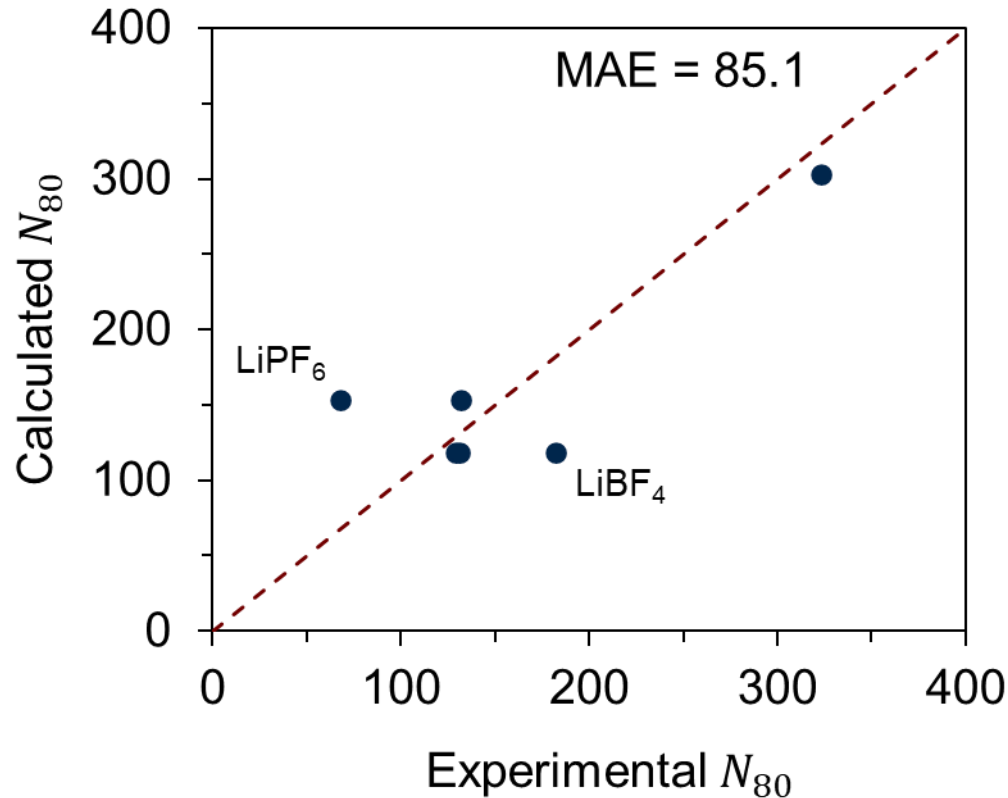


Figure 6.7 Parity plot of experimental and predicted cycle life of TEMPO cycled at 5 mM active material concentration and 1 C rate. The LiPF₆ and LiBF₄ data points are labeled.

The TEMPO 5 mM/1C data set is poorly predicted by the model, with LiPF₆ and LiBF₄ significantly over and underpredicted, respectively. LOOCV returned the same model for all six cases, suggesting that there is no descriptor for this data set that can account for the active material-supporting salt interactions.

The SISSO identified model for the 5 mM active material 3 C rate experiments is

$$N_{80} = A(\Lambda_{\circ-} - \Lambda_{\circ+}) + B$$

Where $A = -8.05$ and $B = 453$. SISSO identifies both supporting salt ions as necessary to predict N_{80} ; favoring supporting salts with similar cationic and anionic limiting molar conductivities. The parity plot is shown in Figure 6.8.

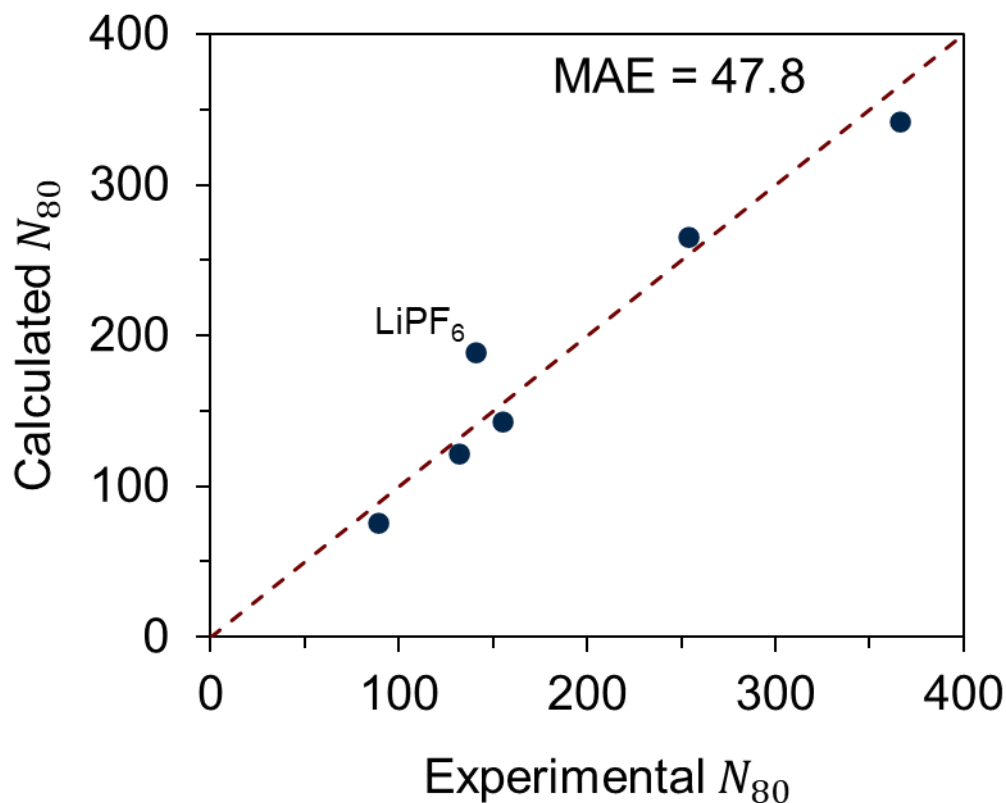


Figure 6.8 Parity plot of experimental and predicted cycle life of TEMPO cycled at 5 mM active material concentration and 3 C rate. The LiPF₆ data point is labeled.

Once again, the LiPF₆ is the worst predicted experiment due to TEMPO-LiPF₆ coordination that is unaccounted for in the descriptor set. LOOCV succeeded in five out of six cases, failing with LiTFSi, the experiment with the largest N_{80} .

The SISO identified model for the 20 mM active material 1 C rate experiments is

$$N_{80} = A \frac{L}{\Lambda_{\circ-}} + B$$

Where $A = 11900$ and $B = -617$. This model is identical to the 5 mM active material 1 C rate model, which confirms the Chapter 3 hypothesis that active material concentration has a scaling, negative effect on TEMPO N_{80} . A parity plot with LiPF₆ labeled is shown in Figure 6.9.

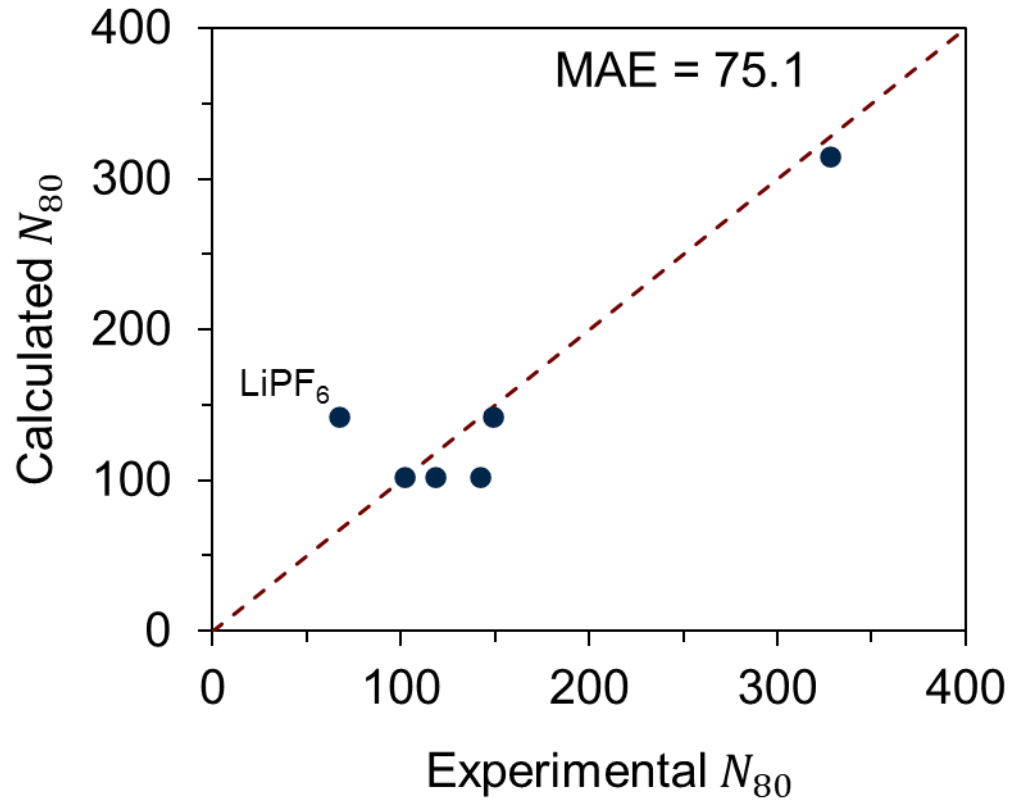


Figure 6.9 Parity plot of experimental and predicted cycle life of TEMPO cycled at 20 mM active material concentration and 1 C rate. The LiPF₆ data point is labeled.

Once again, the LiPF₆ N_{80} is overpredicted by the model. LOOCV for this model also succeeded for five out of six cases, failing for LiTFSi.

The SISSO identified model for the 5 mM active material 3 C rate experiments is

$$N_{80} = Ar_{\Lambda^+} + B$$

Where $A = 11.8$ and $B = -67.2$. This model does not match the 5 mM 3 C rate model, but the 20 mM 3 C condition did not fit any trends in Chapter 3. A parity plot with the LiPF₆ callout is shown in Figure 6.10.

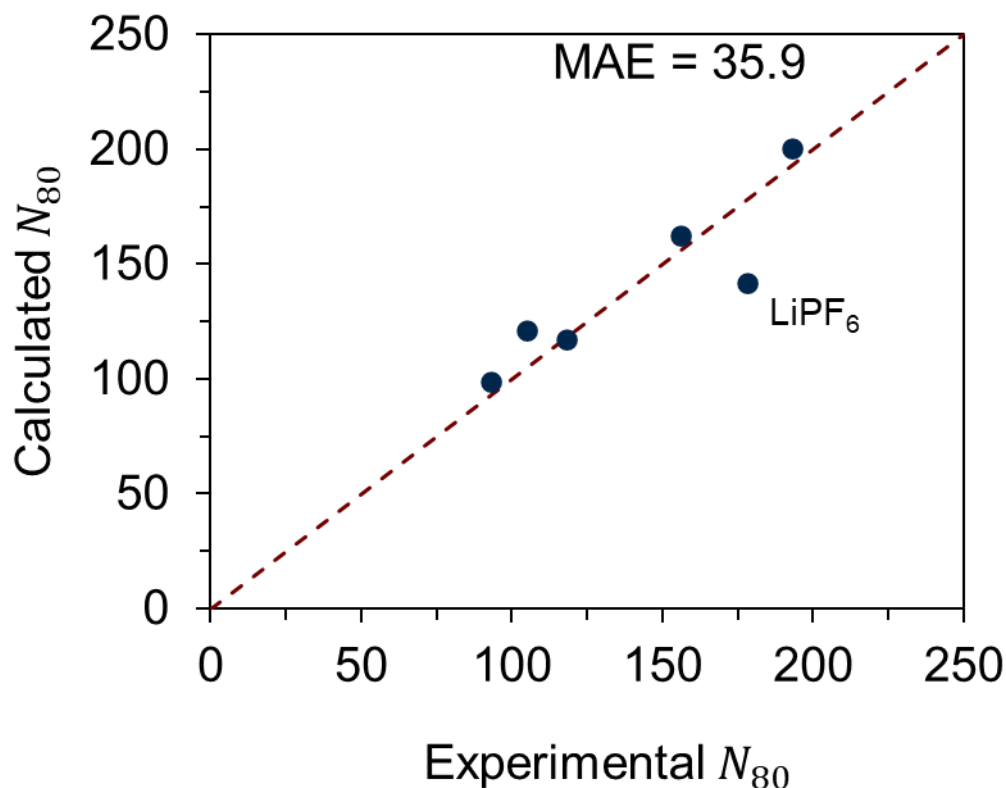


Figure 6.10 Parity plot of experimental and predicted cycle life of TEMPO cycled at 20 mM active material concentration and 3 C rate. The LiPF₆ data point is labeled.

Of the four TEMPO models, the 20 mM 3 C model is the only one to underpredict LiPF₆, although it is still the outlier. LOOCV succeeded in five out of six cases, failing with the exclusion of LiBF₄.

The five models developed for supporting salt variation show that prediction of N_{80} for new supporting salts is possible. For TEMPO and DBBB at 20 mM 1 C experimental conditions, new supporting salts can be screened before characterization, identifying supporting salts that can further improve N_{80} .

6.4 Conclusions

In this Chapter, SISO was used to develop descriptors and models for ROM cyclability. These models are the first for ROMs, although only two are applicable to multiple active materials. For the dialkoxyarene catholytes, two models were developed for N_{80} . The first

encompassed the experiments in Chapter 2 at 5 mM active material, 1 C rate, with a TBAPF₆/MeCN electrolyte, the second was developed for the same active materials cycled at 20 mM concentration, 3 C rate, in a LiTFSi/MeCN electrolyte. Two models were developed for the experimental condition experiments in Chapter 3, predicting N_{80} for cells with 20 mM active material. Models for this specific concentration were successfully identified due to the lower significance of the BF₄⁻ impurity affecting dialkoxyarene cycling. Lastly, five models predicting the impact of supporting salts on specific active materials and experimental conditions were developed. From the SISO descriptors, dialkoxyarene cyclability is governed by steric factors, LUMO energy, and the solvation energy, although the effect of the LUMO is unknown. Ultimately, this work introduces design tools for hydrocarbon-substituted dialkoxyarenes and began predicting N_{80} for ROMs.

6.5 Acknowledgments

I would like to thank Dr. Siwon Tung for characterizing C3 and C4.

Chapter 7

Conclusions and Future Directions

7.1 Conclusions

Non-aqueous redox flow batteries (NaRFBs) are promising candidates for the future of grid scale energy storage. Due to their high energy densities, they have potential for low-cost electricity storage. However, the candidate active materials employed in these batteries cannot provide the necessary stability and cyclability for scale-up. This thesis presents a novel combination of experimental and computational work focused on improving redox active organic molecules (ROMs) for NaRFBs. By combining computational and experimental work, key descriptors of stable and cyclable molecules were identified, enabling new strategies for active material development.

7.1.1. Cyclability Characterization

The first section of this thesis focused on cyclability characterization of ROM catholytes. The dialkoxyarene family is the most studied ROM family for NaRFB applications and their development from lithium-ion overcharge protection molecules to NaRFB active materials was introduced. Chapter 2 discussed nine new hydrocarbon substituted-dialkoxyarenes with new functional group variations. Electrochemical characterization of these active materials revealed trends between oxidation potential, cycle life (N_{80}), and coulombic efficiency (CE). All three of these electrochemical properties correlated well to steric hindrance, which was identified as the most significant descriptor for performance. Additional gas and liquid chromatography revealed dialkoxyarenes decay through O-dealkylation, which is disrupted when more sterically hindered

ligands are present. However, these results were inconsistent with cyclability trends in Li^+ supporting salts, which implied the existence of a second stabilization mechanism.

An alternative stabilization mechanism only present in Li^+ supporting salts required an investigation of the effects of experimental conditions on N_{80} . Chapter 3 identified three variable factors in cycling experiments, active material concentration, cycle rate, and supporting salt choice. A systematic variation of these three factors in cycling experiments of three different ROM catholytes revealed significant effects of supporting salt choice on N_{80} . Li^+ support salts engaged in varying degrees of coordination to active materials, a largely beneficial effect. Additionally, BF_4^- supporting salts were shown to have an electrochemically active impurity, drastically impacting the N_{80} of dialkoxyarenes. However, this study did not develop relationships to normalize N_{80} for these three experimental factors.

With the difficulty comparing N_{80} between different experimental conditions, Chapter 4 introduced a new metric for cyclability, recovery (ϕ). ϕ was derived from a kinetic model for bulk electrolysis cycling, the first of its kind. ϕ normalizes experimental results for active material concentration and cycle rate, which allows experiments to be compared independent of these conditions. However, ϕ is still dependent on active material-supporting salt interactions present in experiments, which limits its use as a universal cyclability comparison. Additionally, the kinetic model for cycling identifies the theoretical maximum CE, which is used to identify experiments with unphysical charge retention, indicative of Li^+ coordination to active materials.

Collectively, these results can be used to improve future characterization of ROMs and other active materials for all classes of RFBs. The identification of structural contributors to cyclability is critical for future ROM development and the two stabilizing mechanisms identified provides different pathways towards more cyclable active materials. Combining these active material design strategies with proper electrolyte selection can improve ROM cyclability to reach RFB targets for commercial deployment within a decade.

7.1.2 Computational Screening and Prediction

The second section of this thesis discussed computational screening and prediction of two key active material properties, stability and cyclability. As NaRFB development is currently limited

by synthesis and characterization of candidate active materials, it is desirable to have in silico methods for characterization. Chapter 5 introduces computational models for screening and predicting stability of ROMs. The screening model is generalizable to all ROM families and identifies unstable active materials, allowing them to be removed from the workflow before synthesis. Two additional predictive models for dialkoxyarene ROMs were developed to identify descriptors for dialkoxyarene stability and provide computational design tools for new materials.

Lifetime of NaRFBs is currently the greatest limiting factor to scale up, which places an even greater importance on cyclability prediction compared to stability prediction. In Chapter 6, N_{80} data from Chapters 2 and 3 was used to develop predictive models. A model for hydrocarbon substituted-dialkoxyarenes identified steric effects and the solvation energy as the two most important factors for predicting dialkoxyarene N_{80} . Attempts to predict N_{80} with variations to active material, active material concentration, cycle rate, and supporting salt failed, but predictions were successfully made for active material and supporting salt variations. These predictions act as a starting point for design of new active materials for cyclability and to optimize electrolyte choice. However, cyclability is significantly more complex than stability and these models are not as robust or impactful as those for stability. Combined, the modeling work in this thesis offers many computational design tools for ROMs, with a focus on the dialkoxyarene family.

7.2 Future Directions

The greatest challenge for NaRFB development is still the development of stable and cyclable active materials. New ROM development has successfully demonstrated design concepts for improving solubility, redox potential, and stability.^{45,48,59} Cyclability is still a black box for design, with varied structural effects that are molecular family dependent. Unfortunately, the only way to identify the factors affecting cyclability are with synthesis and characterization of new ROMs to validate current models and provide the necessary data needed for robust model development.

From the results presented in this thesis, Li^+ -coordination to active materials is the best strategy for improving ROM cyclability, although the effect is dependent on the choice of

electrolyte. Development for active materials must consider the desired supporting salt and electrolyte environment, with different design targets for different electrolytes. For the dialkoxyarene family, development for cyclability in alkylammonium supporting salts should be focused on increasing the steric hinderance of the substituting ligands, although care must be taken with regards to solubility in non-aqueous electrolytes. Designing for cyclability in Li⁺ supporting salts should focus on maintaining Li⁺ coordination while substituting functional groups with improved solubility. Li⁺ coordination to improve cyclability is the most promising design strategy for reaching the NaRFB scale-up targets, although the dependence on Li⁺ introduces the mineral resource disadvantages from metal coordination complexes to ROMs. Designing for Li⁺ coordination may also benefit from improvements in Li-ion electrolytes and development of beyond Li-ion batteries.

While this thesis did investigate and identify the effects of supporting salt choice on cyclability, there are still numerous unknown factors affecting measured N_{80} . Additional characterization on existing ROMs would help identify these factors. Two principal areas of additional characterization are the investigation of additional supporting salts and the investigation of new solvents. Both supporting salts and non-aqueous solvents can have significant stabilizing or destabilizing effects on ROM stability and cyclability,⁷³ but most active materials are only characterized in one electrolyte.^{60,72,92} The addition of other supporting salts, such as TEATFSi, to the existing data set would provide additional data to isolate key active material-supporting salt interactions of dialkoxyarenes and TEMPO. Investigation of new electrolytes has the potential to identify previously developed and discarded active materials which show significant stability and cyclability improvements in specific electrolytes.

Lastly, the significant performance enhancement seen for dialkoxyarenes in this thesis merits further investigation in full flow cell systems. DDB and DBBB show remarkable cyclability in bulk electrolysis with Li⁺ supporting salts, but this may not transfer to other cycling experiments. Flow cell cyclability introduces additional membrane and anolyte interactions, which are likely to decrease overall cyclability. However, the remarkable performance of DDB and DBBB demonstrated in this thesis should be used as a starting point for further ROM development and characterization.

References

- (1) Form EIA-860 detailed data with previous form data (EIA-860A/860B) <https://www.eia.gov/electricity/data/eia860/> (accessed Oct 28, 2020).
- (2) Annual Energy Outlook 2020 <https://www.eia.gov/outlooks/aeo/> (accessed Oct 28, 2020).
- (3) Soloveichik, G. L. Flow Batteries: Current Status and Trends. *Chem. Rev.* **2015**, *115* (20), 11533–11558.
- (4) Chen, H.; Cong, T. N.; Yang, W.; Tan, C.; Li, Y.; Ding, Y. Progress in Electrical Energy Storage System: A Critical Review. *Prog. Nat. Sci.* **2009**, *19* (3), 291–312.
- (5) U.S. Grid Energy Storage Factsheet | Center for Sustainable Systems <http://css.umich.edu/factsheets/us-grid-energy-storage-factsheet> (accessed Oct 28, 2020).
- (6) Sabihuddin, S.; Kiprakis, A.; Mueller, M. A Numerical and Graphical Review of Energy Storage Technologies. *Energies* **2014**, *8* (1), 172–216.
- (7) Ter-Gazarian, A. G. *Energy Storage for Power Systems*, 2nd Editio.; IET: Stevenage, 2011.
- (8) *Large Energy Storage Systems Handbook*, First Edit.; Barnes, F. S., Levine, J. G., Eds.; CRC Press: Boca Raton, 2011.
- (9) Chen, H.; Cong, G.; Lu, Y. C. Recent Progress in Organic Redox Flow Batteries: Active Materials, Electrolytes and Membranes. *Journal of Energy Chemistry*. Elsevier B.V. September 1, 2018, pp 1304–1325.
- (10) Doris, S. E.; Ward, A. L.; Baskin, A.; Frischmann, P. D.; Gavvalapalli, N.; Chénard, E.; Sevov, C. S.; Prendergast, D.; Moore, J. S.; Helms, B. A. Macromolecular Design Strategies for Preventing Active-Material Crossover in Non-Aqueous All-Organic Redox-Flow Batteries. *Angew. Chemie Int. Ed.* **2017**, *56* (6), 1595–1599.
- (11) Li, Y.; Nulens, I.; Verbeke, R.; Mariën, H.; Koschine, T.; Dickmann, M.; Egger, W.;

- Vankelecom, I. F. J. Tuning the Porosity of Asymmetric Membranes via Simple Post-Synthesis Solvent-Treatment for Non-Aqueous Applications. *Sep. Purif. Technol.* **2019**, *217*, 147–153.
- (12) Darling, R. M.; Gallagher, K. G.; Kowalski, J. A.; Ha, S.; Brushett, F. R. Pathways to Low-Cost Electrochemical Energy Storage: A Comparison of Aqueous and Nonaqueous Flow Batteries. *Energy Environ. Sci.* **2014**, *7* (11), 3459–3477.
- (13) Wang, W.; Luo, Q.; Li, B.; Wei, X.; Li, L.; Yang, Z. Recent Progress in Redox Flow Battery Research and Development. *Adv. Funct. Mater.* **2013**.
- (14) Pissort, P. A. No Title. 754065, 1933.
- (15) 'NASA TM-79067 i REDOX FLOW CELL DEVELOPMENT AND DEMONSTRATION PROJECT.
- (16) Skyllas-Kazacos, M.; Rychcik, M.; Robins, R. G.; Fane, A. G.; Green, M. A. New All-Vanadium Redox Flow Cell. *J. Electrochem. Soc.* **1986**, *133* (5), 1057–1058.
- (17) Li, L.; Kim, S.; Wang, W.; Vijayakumar, M.; Nie, Z.; Chen, B.; Zhang, J.; Xia, G.; Hu, J.; Graff, G.; et al. A Stable Vanadium Redox-Flow Battery with High Energy Density for Large-Scale Energy Storage. *Adv. Energy Mater.* **2011**, *1* (3), 394–400.
- (18) Wu, X.; Xu, H.; Shen, Y.; Xu, P.; Lu, L.; Fu, J.; Zhao, H. Treatment of Graphite Felt by Modified Hummers Method for the Positive Electrode of Vanadium Redox Flow Battery. *Electrochim. Acta* **2014**, *138*, 264–269.
- (19) Wang, W. H.; Wang, X. D. Investigation of Ir-Modified Carbon Felt as the Positive Electrode of an All-Vanadium Redox Flow Battery. *Electrochim. Acta* **2007**, *52* (24), 6755–6762.
- (20) Li, Y.; Parrondo, J.; Sankarasubramanian, S.; Ramani, V. Impact of Surface Carbonyl- and Hydroxyl-Group Concentrations on Electrode Kinetics in an All-Vanadium Redox Flow Battery. *J. Phys. Chem. C* **2019**, *123* (11), 6370–6378.
- (21) Greco, K. V.; Forner-Cuenca, A.; Mularczyk, A.; Eller, J.; Brushett, F. R. Elucidating the Nuanced Effects of Thermal Pretreatment on Carbon Paper Electrodes for Vanadium Redox Flow Batteries. *ACS Appl. Mater. Interfaces* **2018**, *10* (51), 44430–44442.
- (22) Choi, C.; Kim, S.; Kim, R.; Choi, Y.; Kim, S.; Jung, H. young; Yang, J. H.; Kim, H. T. A Review of Vanadium Electrolytes for Vanadium Redox Flow Batteries. *Renewable and Sustainable Energy Reviews*. Elsevier Ltd March 1, 2017, pp 263–274.

- (23) Cao, L.; Skyllas-Kazacos, M.; Menictas, C.; Noack, J. A Review of Electrolyte Additives and Impurities in Vanadium Redox Flow Batteries. *Journal of Energy Chemistry*. Elsevier B.V. September 1, 2018, pp 1269–1291.
- (24) The Zito Company. No Title. 3806368, 1972.
- (25) Rajarathnam, G. P.; Vassallo, A. M. Strategies for Studying and Improving the Zn/Br RFB; Springer, Singapore, 2016; pp 81–97.
- (26) Leung, P. K.; Ponce-De-León, C.; Low, C. T. J.; Shah, A. A.; Walsh, F. C. Characterization of a Zinc-Cerium Flow Battery. *J. Power Sources* **2011**, *196* (11), 5174–5185.
- (27) Xie, Z.; Liu, Q.; Chang, Z.; Zhang, X. The Developments and Challenges of Cerium Half-Cell in Zinc-Cerium Redox Flow Battery for Energy Storage. *Electrochimica Acta*. Pergamon February 15, 2013, pp 695–704.
- (28) Liu, T.; Wei, X.; Nie, Z.; Sprenkle, V.; Wang, W. A Total Organic Aqueous Redox Flow Battery Employing a Low Cost and Sustainable Methyl Viologen Anolyte and 4-HO-TEMPO Catholyte. *Adv. Energy Mater.* **2016**, *6* (3), 1501449.
- (29) Hagemann, T.; Winsberg, J.; Grube, M.; Nischang, I.; Janoschka, T.; Martin, N.; Hager, M. D.; Schubert, U. S. An Aqueous All-Organic Redox-Flow Battery Employing a (2,2,6,6-Tetramethylpiperidin-1-yl)Oxyl-Containing Polymer as Catholyte and Dimethyl Viologen Dichloride as Anolyte. *J. Power Sources* **2018**, *378*, 546–554.
- (30) Cole, W.; Frazier, A. W. *Cost Projections for Utility-Scale Battery Storage: 2020 Update; 2030*.
- (31) Mongird, K.; Fotedar, V.; Viswanathan, V.; Koritarov, V.; Balducci, P.; Hadjerioua, B.; Alam, J. *Energy Storage Technology and Cost Characterization Report; 2019*.
- (32) Ue, M.; Ida, K.; Mori, S. Electrochemical Properties of Organic Liquid Electrolytes Based on Quaternary Onium Salts for Electrical Double-Layer Capacitors. *J. Electrochem. Soc.* **1994**, *141* (11), 2989.
- (33) Izutsu, K. *Electrochemistry in Nonaqueous Solutions*; Wiley-VCH Verlag GmbH & Co. KGaA: Weinheim, Germany, 2009.
- (34) Gong, K.; Fang, Q.; Gu, S.; Li, S. F. Y.; Yan, Y. Nonaqueous Redox-Flow Batteries: Organic Solvents, Supporting Electrolytes, and Redox Pairs. *Energy Environ. Sci.* **2015**, *8* (12), 3515–

3530.

- (35) Yuan, K.; Bian, H.; Shen, Y.; Jiang, B.; Li, J.; Zhang, Y.; Chen, H.; Zheng, J. Coordination Number of Li⁺ in Nonaqueous Electrolyte Solutions Determined by Molecular Rotational Measurements. **2014**.
- (36) Barthel, J. M. G.; Gores, H. J.; Neueder, R.; Schmid, A. Electrolyte Solutions for Technology - New Aspects and Approaches. *Pure Appl. Chem.* **1999**, *71* (9), 1705–1715.
- (37) Williams, D. B. G.; Lawton, M. Drying of Organic Solvents: Quantitative Evaluation of the Efficiency of Several Desiccants. *J. Org. Chem.* **2010**, *75* (24), 8351–8354.
- (38) Seo, D. M.; Borodin, O.; Han, S.-D.; Ly, Q.; Boyle, P. D.; Henderson, W. A. Electrolyte Solvation and Ionic Association I. Acetonitrile-Lithium Salt Mixtures: Intermediate and Highly Associated Salts. *J. Electrochem. Soc.* **2012**, *159* (5), 553–565.
- (39) Ue, M. Mobility and Ionic Association of Lithium and Quaternary Ammonium Salts in Propylene Carbonate and γ -Butyrolactone. *J. Electrochem. Soc.* **1994**, *141* (12), 3336.
- (40) Seo, D. M.; Boyle, P. D.; Borodin, O.; Henderson, W. A. Li⁺ Cation Coordination by Acetonitrile—Insights from Crystallography. *RSC Adv.* **2012**, *2* (21), 8014.
- (41) Carino, E. V.; Staszak-Jirkovsky, J.; Assary, R. S.; Curtiss, L. A.; Markovic, N. M.; Brushett, F. R. Tuning the Stability of Organic Active Materials for Nonaqueous Redox Flow Batteries via Reversible, Electrochemically Mediated Li⁺ Coordination. *Chem. Mater.* **2016**, *28* (8), 2529–2539.
- (42) Kowalski, J. A.; Su, L.; Milshtein, J. D.; Brushett, F. R. Recent Advances in Molecular Engineering of Redox Active Organic Molecules for Nonaqueous Flow Batteries. *Curr. Opin. Chem. Eng.* **2016**, *13*, 45–52.
- (43) Buhrmester, C.; Chen, J.; Moshurchak, L.; Jiang, J.; Wang, R. L.; Dahn, J. R. Studies of Aromatic Redox Shuttle Additives for LiFePO₄-Based Li-Ion Cells. *J. Electrochem. Soc.* **2005**, *152* (12), A2390.
- (44) Buhrmester, C.; Moshurchak, L. M.; Wang, R. L.; Dahn, J. R. The Use of 2,2,6,6-Tetramethylpiperinyl-Oxides and Derivatives for Redox Shuttle Additives in Li-Ion Cells. *J. Electrochem. Soc.* **2006**, *153* (10), A1800.
- (45) Huang, J.; Cheng, L.; Assary, R. S.; Wang, P.; Xue, Z.; Burrell, A. K.; Curtiss, L. A.; Zhang, L.

- Liquid Catholyte Molecules for Nonaqueous Redox Flow Batteries. *Adv. Energy Mater.* **2015**, 5 (6), 1401782.
- (46) Zhang, L.; Zhang, Z.; Redfern, P. C.; Curtiss, L. A.; Amine, K. Molecular Engineering towards Safer Lithium-Ion Batteries: A Highly Stable and Compatible Redox Shuttle for Overcharge Protection. *Energy Environ. Sci.* **2012**, 5 (8), 8204.
- (47) Wei, X.; Xu, W.; Vijayakumar, M.; Cosimbescu, L.; Liu, T.; Sprenkle, V.; Wang, W. TEMPO-Based Catholyte for High-Energy Density Nonaqueous Redox Flow Batteries. *Adv. Mater.* **2014**, 26 (45), 7649–7653.
- (48) Sevov, C. S.; Hickey, D. P.; Cook, M. E.; Robinson, S. G.; Barnett, S.; Minter, S. D.; Sigman, M. S.; Sanford, M. S. Physical Organic Approach to Persistent, Cyclable, Low-Potential Electrolytes for Flow Battery Applications. *J. Am. Chem. Soc.* **2017**, 139, 2924–2927.
- (49) Duan, W.; Huang, J.; Kowalski, J. A.; Shkrob, I. A.; Vijayakumar, M.; Walter, E.; Pan, B.; Yang, Z.; Milshtein, J. D.; Li, B.; et al. “Wine-Dark Sea” in an Organic Flow Battery: Storing Negative Charge in 2,1,3- Benzothiadiazole Radicals Leads to Improved Cyclability.
- (50) Matsuda, Y.; Tanaka, K.; Okada, M.; Takasu, Y.; Morita, M.; Matsumura-Inoue, T. A Rechargeable Redox Battery Utilizing Ruthenium Complexes with Non-Aqueous Organic Electrolyte. *J. Appl. Electrochem.* **1988**, 18 (6), 909–914.
- (51) Herr, T.; Fischer, P.; Tübke, J.; Pinkwart, K.; Elsner, P. Increasing the Energy Density of the Non-Aqueous Vanadium Redox Flow Battery with the Acetonitrile-1,3-Dioxolane-Dimethyl Sulfoxide Solvent Mixture. *J. Power Sources* **2014**, 265, 317–324.
- (52) Liu, Q.; Sleightholme, A. E. S.; Shinkle, A. A.; Li, Y.; Thompson, L. T. Non-Aqueous Vanadium Acetylacetonate Electrolyte for Redox Flow Batteries. *Electrochem. commun.* **2009**, 11 (12), 2312–2315.
- (53) Kucharyson, J. F.; Cheng, L.; Tung, S. O.; Curtiss, L. A.; Thompson, L. T. Predicting the Potentials, Solubilities and Stabilities of Metal-Acetylacetonates for Non-Aqueous Redox Flow Batteries Using Density Functional Theory Calculations. *J. Mater. Chem. A* **2017**, 5 (26), 13700–13709.
- (54) Fisher, S. L. Non-Aqueous Redox Flow Batteries : Active Species Stability and Cost Saving Design Concepts, University of Michigan, 2017.

- (55) Burgess, M.; Moore, J. S.; Rodríguez-López, J. Redox Active Polymers as Soluble Nanomaterials for Energy Storage. *Acc. Chem. Res.* **2016**, *49* (11), 2649–2657.
- (56) Montoto, E. C.; Nagarjuna, G.; Hui, J.; Burgess, M.; Sekerak, N. M.; Hernández-Burgos, K.; Wei, T.-S.; Kneer, M.; Grolman, J.; Cheng, K. J.; et al. Redox Active Colloids as Discrete Energy Storage Carriers. *J. Am. Chem. Soc.* **2016**, *138* (40), 13230–13237.
- (57) Cheng, L.; Assary, R. S.; Qu, X.; Jain, A.; Ong, S. P.; Rajput, N. N.; Persson, K.; Curtiss, L. A. Accelerating Electrolyte Discovery for Energy Storage with High-Throughput Screening. *J. Phys. Chem. Lett.* **2015**, *6* (2), 283–291.
- (58) Zhang, C.; Zhang, L.; Ding, Y.; Peng, S.; Guo, X.; Zhao, Y.; He, G.; Yu, G. Progress and Prospects of Next-Generation Redox Flow Batteries. *Energy Storage Materials*. Elsevier B.V. November 1, 2018, pp 324–350.
- (59) Huang, J.; Pan, B.; Duan, W.; Wei, X.; Assary, R. S.; Su, L.; Brushett, F. R.; Cheng, L.; Liao, C.; Ferrandon, M. S.; et al. The Lightest Organic Radical Cation for Charge Storage in Redox Flow Batteries. *Sci. Rep.* **2016**, *6* (1), 32102.
- (60) Huang, J.; Su, L.; Kowalski, J. A.; Barton, J. L.; Ferrandon, M.; Burrell, A. K.; Brushett, F. R.; Zhang, L. A Subtractive Approach to Molecular Engineering of Dimethoxybenzene-Based Redox Materials for Non-Aqueous Flow Batteries. *J. Mater. Chem. A* **2015**, *3* (29), 14971–14976.
- (61) Suttill, J. A.; Kucharyson, J. F.; Escalante-Garcia, I. L.; Cabrera, P. J.; James, B. R.; Savinell, R. F.; Sanford, M. S.; Thompson, L. T. Metal Acetylacetonate Complexes for High Energy Density Non-Aqueous Redox Flow Batteries. *J. Mater. Chem. A* **2015**, *3* (15), 7929–7938.
- (62) Kucharyson, J. Structure-Function Relationships of Metal Coordination Complexes for Non-Aqueous Redox Flow Batteries. PhD Dissertation, University of Michigan, 2017.
- (63) Jensen, F. *Introduction to Computational Chemistry*, 3rd ed.; John Wiley & Sons, Inc., 2017.
- (64) Hohenberg, P.; Kohn, W. Inhomogeneous Electron Gas. *Phys. Rev.* **1964**, *136* (3B), B864.
- (65) Kohn, W.; Sham, L. J. Self-Consistent Equations Including Exchange and Correlation Effects. *Phys. Rev.* **1965**, *140* (4A), A1133.
- (66) Rassolov, V. A.; Ratner, M. A.; Pople, J. A.; Redfern, P. C.; Curtiss, L. A. 6-31G* Basis Set for Third-Row Atoms. *J. Comput. Chem.* **2001**, *22* (9), 976–984.

- (67) Becke, A. D. Density-Functional Thermochemistry. III. The Role of Exact Exchange. *J. Chem. Phys.* **1993**, *98* (7), 5648–5652.
- (68) Pelzer, K. M.; Cheng, L.; Curtiss, L. A. Effects of Functional Groups in Redox-Active Organic Molecules: A High-Throughput Screening Approach. *J. Phys. Chem. C* **2017**, *121*, 237–245.
- (69) Gaussian 09 Rev E.01; Frisch, M. J.; Trucks, G. W.; Schlegel, H. B.; Scuseria, G. E.; Robb, M. A.; Cheeseman, J. R.; Scalmani, G.; Barone, V.; Mennucci, B.; et al. Gaussian 09 Rev E.01. Gaussian Inc.: Wallingford CT 2009.
- (70) Kucharyson, J. F.; Gaudet, J. R.; Wyvrat, B. M.; Thompson, L. T. Characterization of Structural and Electronic Transitions During Reduction and Oxidation of Ru(Acac)₃ Flow Battery Electrolytes by Using X-Ray Absorption Spectroscopy. *ChemElectroChem* **2016**, *3* (11), 1875–1883.
- (71) Seo, D. M.; Borodin, O.; Han, S.-D.; Boyle, P. D.; Henderson, W. A. Electrolyte Solvation and Ionic Association II. Acetonitrile-Lithium Salt Mixtures: Highly Dissociated Salts. *J. Electrochem. Soc.* **2012**, *159* (9), A1489–A1500.
- (72) Sevov, C. S.; Fisher, S. L.; Thompson, L. T.; Sanford, M. S. Mechanism-Based Development of a Low-Potential, Soluble, and Cyclable Multielectron Anolyte for Nonaqueous Redox Flow Batteries. *J. Am. Chem. Soc.* **2016**, *138* (47), 15378–15384.
- (73) Wei, X.; Xu, W.; Huang, J.; Zhang, L.; Walter, E.; Lawrence, C.; Vijayakumar, M.; Henderson, W. A.; Liu, T.; Cosimbescu, L.; et al. Radical Compatibility with Nonaqueous Electrolytes and Its Impact on an All-Organic Redox Flow Battery. *Angew. Chemie Int. Ed.* **2015**, *54* (30), 8684–8687.
- (74) Zhang, J.; Yang, Z.; Shkrob, I. A.; Assary, R. S.; Tung, S. on; Silcox, B.; Duan, W.; Zhang, J.; Su, C. C.; Hu, B.; et al. Annulated Dialkoxybenzenes as Catholyte Materials for Non-Aqueous Redox Flow Batteries: Achieving High Chemical Stability through Bicyclic Substitution. *Adv. Energy Mater.* **2017**, *7* (21), 1701272.
- (75) Kowalski, J. A.; Carney, T. J.; Huang, J.; Zhang, L.; Brushett, F. R. An Investigation on the Impact of Halidization on Substituted Dimethoxybenzenes. *Electrochim. Acta* **2020**, *335*.
- (76) Silcox, B.; Zhang, J.; Shkrob, I. A.; Thompson, L.; Zhang, L. On Transferability of Performance Metrics for Redox-Active Molecules. *J. Phys. Chem. C* **2019**, *123* (27), 16516–16524.

- (77) Electric Power Research Institute (EPRI). Market Driven Distributed Energy Storage Requirements for Load Management Applications. *Manager* **2007**, 3 (3), 1–60.
- (78) Yamada, Y.; Furukawa, K.; Sodeyama, K.; Kikuchi, K.; Yaegashi, M.; Tateyama, Y.; Yamada, A. Unusual Stability of Acetonitrile-Based Superconcentrated Electrolytes for Fast-Charging Lithium-Ion Batteries. *J. Am. Chem. Soc.* **2014**, 136 (13), 5039–5046.
- (79) Xin, N.; Sun, Y.; He, M.; Radke, C. J.; Prausnitz, J. M. *Solubilities of Six Lithium Salts in Five Non-Aqueous Solvents and in a Few of Their Binary Mixtures*.
- (80) Ma, Y.; Loyns, C.; Price, P.; Chechik, V. Organic & Biomolecular Chemistry Thermal Decay of TEMPO in Acidic Media via an N-Oxoammonium Salt Intermediate †. **2011**.
- (81) Ding, Y.; Zhang, C.; Zhang, L.; Zhou, Y.; Yu, G. Molecular Engineering of Organic Electroactive Materials for Redox Flow Batteries. *Chem. Soc. Rev.* **2018**, 47 (1), 69–103.
- (82) Assary, R. S.; Curtiss, L. A.; Redfern, P. C.; Zhang, Z.; Amine, K. Computational Studies of Polysiloxanes: Oxidation Potentials and Decomposition Reactions. *J. Phys. Chem. C* **2011**, 115, 12216–12223.
- (83) Zhang, J.; Shkrob, I. A.; Assary, R. S.; Tung, S. O.; Silcox, B.; Curtiss, L. A.; Thompson, L.; Zhang, L. Toward Improved Catholyte Materials for Redox Flow Batteries: What Controls Chemical Stability of Persistent Radical Cations? *J. Phys. Chem. C* **2017**, 121 (42), 23347–23358.
- (84) Brushett, F. R.; Vaughey, J. T.; Jansen, A. N. An All-Organic Non-Aqueous Lithium-Ion Redox Flow Battery. *Adv. Energy Mater.* **2012**, 2 (11), 1390–1396.
- (85) Ouyang, R.; Curtarolo, S.; Ahmetcik, E.; Scheffler, M.; Ghiringhelli, L. M. SISSO: A Compressed-Sensing Method for Identifying the Best Low-Dimensional Descriptor in an Immensity of Offered Candidates. *Phys. Rev. Mater.* **2018**, 2, 83802.
- (86) Huang, J.; Azimi, N.; Cheng, L.; Shkrob, I. A.; Xue, Z.; Zhang, J.; Dietz Rago, N. L.; Curtiss, L. A.; Amine, K.; Zhang, Z.; et al. An Organophosphine Oxide Redox Shuttle Additive That Delivers Long-Term Overcharge Protection for 4 v Lithium-Ion Batteries. *J. Mater. Chem. A* **2015**, 3 (20), 10710–10714.
- (87) Marenich, A. V.; Cramer, C. J.; Truhlar, D. G. Universal Solvation Model Based on Solute Electron Density and on a Continuum Model of the Solvent Defined by the Bulk Dielectric

- Constant and Atomic Surface Tensions. *J. Phys. Chem. B* **2009**, *113* (18), 6378–6396.
- (88) Brethomé, A. V.; Fletcher, S. P.; Paton, R. S. Conformational Effects on Physical-Organic Descriptors: The Case of Sterimol Steric Parameters. *ACS Catal.* **2019**, *9* (3), 2313–2323.
- (89) Ouyang, R.; Ahmetcik, E.; Carbogno, C.; Scheffler, M.; Ghiringhelli, L. M. Simultaneous Learning of Several Materials Properties from Incomplete Databases with Multi-Task SISSO. *J. Phys. Mater.* **2019**, *2* (2), 024002.
- (90) Weng, W.; Huang, J.; Shkrob, I. A.; Zhang, L.; Zhang, Z. Redox Shuttles with Axisymmetric Scaffold for Overcharge Protection of Lithium-Ion Batteries. *Adv. Energy Mater.* **2016**, *6* (19).
- (91) Ue, M. Mobility and Ionic Association of Lithium and Quaternary Ammonium Salts in Propylene Carbonate and γ -Butyrolactone. *J. Electrochem. Soc.* **1994**, *141* (12), 3336.
- (92) Huang, J.; Duan, W.; Zhang, J.; Shkrob, I. A.; Assary, R. S.; Pan, B.; Liao, C.; Zhang, Z.; Wei, X.; Zhang, L. Substituted Thiadiazoles as Energy-Rich Anolytes for Nonaqueous Redox Flow Cells. *J. Mater. Chem. A* **2018**, *6* (15), 6251–6254.